

Direct-Write Digital Holography

Development and research of a hologram printer

John Peter Tapsell

Submitted for the degree of Doctor of Philosophy

University of Sussex

April 2008

To my wife, Saki.

Declaration

I hereby declare that this thesis, either in the same or different form, has not been previously submitted to this or any other University for a degree.

Signature:

John Peter Tapsell

UNIVERSITY OF SUSSEX

JOHN PETER TAPSELL, DOCTOR OF PHILOSOPHY

DIRECT-WRITE DIGITAL HOLOGRAPHY

DEVELOPMENT AND RESEARCH OF A HOLOGRAM PRINTER

SUMMARY

Chapter 1 gives a brief history of the field of holography along with an overview of this thesis. A more detailed description of holography is provided in Chapter 2 along with a discussion of digital holography. Chapter 3 examines the design of a one-step monochromatic hologram printer capable producing white-light viewable transmission holograms created with the aid of an LCOS display system and printed in a dot-matrix sequence. The lens system employed includes a microlens array and an afocal relay telescope which are both quantitatively examined in order to maximise the contrast, diffraction efficiency and depth of view of the final hologram image. A brief overview of speckle reduction techniques and their applicability to pulsed digital holography is presented along with experimental results of the use of a microlens array to reduce speckle effects. Chapter 4 presents an analysis of the unwanted side effects of the angular intensity distribution of a hologram pixel, using a case study for analysis. Chapter 5 examines methods for increasing both the printing speed and resolution of the hologram printer. Chapter 6 describes the analysis and design of a temperature-energy feedback system to correct for pulsed laser instabilities arising from mode beating due to temperature variations. Chapter 7 provides a conclusion to the work and discusses possible future developments.

Acknowledgements

I would first like to thank the people who made this project possible: My university supervisors Professor Chris Chatwin and Dr. Rupert Young for their help and encouragement; and my work supervisor Dr. David Brotherton-Ratcliffe and the staff at Geola Technologies for allowing me to break much of their valuable equipment over the three years of employment. I would also like to make a special mention to Doug Ollivier for his permission for the use of his 3D futuristic-tank model.

A special thanks goes out to my brother, Ian Kevin Tapsell, who spent many days and nights working with me in the dark room handling the chemicals and processing the holograms with expert ease.

I would also like to acknowledge the support of a EPSRC fellowship. This work was funded by the UK's leading funding agency - the Engineering and Physical Sciences Research Council. Without this opportunity, I never would have delved into the world of physics and engineering.

Finally, my warmest appreciation goes to my darling wife Saki Tapsell, who looked after me at every step of the way. Without her, none of this would have been possible.

Contents

Contents	ix
1 Introduction	1
1.1 Holography	1
1.2 Overview of thesis	3
2 Background	4
2.1 Definition	4
2.2 A brief introduction to photography	5
2.3 History of holography	6
2.4 Digital versus analogue	17
3 Design of a digital hologram printer	19
3.1 Overview	19
3.2 Detail of system components	23
3.2.1 Laser system	24
3.2.2 Optics for transport of beams	25
3.2.3 Digital display system	26
3.3 Analysis of lens system	30
3.3.1 Lenses L1 and L2	38
3.3.2 Lenses L3 and L4	38

3.3.3	Lenses L2 and L3	39
3.3.4	Focal length approximations	40
3.3.5	Optical system for microlens array	40
3.3.6	Summary	47
3.3.7	Example microlens array	48
3.4	Experimental evaluation of lens array system	51
3.4.1	Previous work	52
3.4.2	Experimental setup	54
3.4.3	Image quality	55
3.4.4	Speckle repeating structure size	59
3.4.5	Microlens array focal plane	61
3.4.6	Summary	63
3.5	Minimizing beam energy loss in lens system	65
3.6	Summary	67
4	White logo	69
4.1	Overview	69
4.2	Photograph analysis	73
4.3	Spectrometer	80
4.4	Future work	85
4.5	Summary	88
5	Printing speed and resolution improvements	89
5.1	Overview	89
5.2	Power supply	90
5.3	Stability	91
5.4	Software	96
5.5	Display system refresh rates	98
5.6	Stage movement	99
5.7	Increasing printed holopixel resolution	100

5.8	3D model	103
5.9	Analysis	109
5.10	Summary	112
6	Temperature-energy feedback	113
6.1	Problems with laser instability	113
6.2	Custom energy meter	116
6.2.1	Overview of custom energy meter	117
6.2.2	Methods for diverting beam	117
6.2.3	Calibrating custom energy meter	119
6.3	Digital temperature controller	124
6.4	Temperature feedback algorithm	125
6.5	Temperature feedback system on rear mirror	127
6.6	DTC-PC communication	129
6.7	Temperature-energy feedback	131
6.8	Summary	135
7	Conclusion and future work	136
7.1	Conclusion	136
7.2	Future work	140
A	Program listing for image cropping	150
B	DTC commands	151
C	Hologram printer diagrams	153
D	Program listing for image analysis	160
E	Optical fourier transform lens system	162
F	LCOS mechanical mount	166
G	Lens system	168

H Laser specifications	170
I Microlens array analysis	173
I.1 First microlens array	175
I.2 Second microlens array	178
I.3 Third microlens array	180
J Hologram printer photographs	182

List of Tables

3.1	Micro lens array properties	49
3.2	Size of repeating speckle structure	59
3.3	Distance between microlens array focal plane and aperture	62
4.1	Technical details of spectrometer	82
4.2	Spectrometer results	83
4.3	Photograph intensity for spectrometer results	83
5.1	Maximum reference and object beam separation distance	94
5.2	Maximum angle deviation for a photographic plate	102
B.1	Communication protocol for Digital Temperature Controller	152
G.1	Lens system optical components	169
H.1	Specifications of laser used	172
I.1	Raw data results for first lens array	177
I.2	Raw data results for second lens array	179
I.3	Raw data results for third lens array	181

List of Figures

2.1	First permanent photograph, by Niépce in 1826	5
2.2	Wire diffraction grating, similar to that made by Fraunhofer	8
2.3	Dennis Gabor	8
2.4	Yuri Denisyuk	10
2.5	Theodore H. Maiman	11
3.1	Hologram printer by Ratcliffe et al.	22
3.2	Hologram Printer with LCOS	23
3.3	Top-down orthographic projection of Hologram Printer with LCOS	24
3.4	Length adjustment system	25
3.5	Lens system	28
3.6	Photograph of LCOS being illuminated	29
3.7	Object lens system on printer	31
3.8	Ray-traced lens setup 1	33
3.9	Ray-traced lens setup 2	33
3.10	Logical diagram of optical beam path layout	37
3.11	Effective focal length of lens L4	41
3.12	Brilliant LCOS Display BR1080HC	49
3.13	Quality of the projected image due to speckle	56
3.14	Suitable positions for first microlens array	57
3.15	Suitable positions for second microlens array	58

LIST OF FIGURES

3.16 Suitable positions for third microlens array	58
3.17 Speckle structure against microlens array array position	60
3.18 Distance between microlens array focal plane and aperture images	63
3.19 Photograph of dragon hologram	68
4.1 Viewing-window comparison	71
4.2 White Logo photograph and rendered images	74
4.3 Photograph intensity against rendered image intensity	75
4.4 Photograph minus image intensity against total image intensity . .	77
4.5 Corrected image	77
4.6 Corrected image with each channel corrected separately	78
4.7 Photograph minus image against total (Individual channels)	79
4.8 Photograph of framework for spectrometer and halogen light . . .	80
4.9 Photograph of fine-control spectrometer mount	81
4.10 Photograph of spectrometer in use	82
4.11 Spectrometer readings against photograph readings	84
4.12 Photograph of hologram with decreasing viewing window	86
4.13 Photograph of hologram with decreasing viewing window and en- ergy	87
5.1 Diagram of intersection plane of hologram plate and beams	92
5.2 Object and reference beam misalignment	93
5.3 Behavior of Microsoft Windows <code>sleep()</code> function	97
5.4 Rendered model images	105
5.5 Large rendered model image	106
5.6 High resolution hologram of a futuristic tank	110
5.7 Zoomed in on a small section of the high resolution hologram . . .	111
6.1 Diffraction efficiency curve for VRP-M emulsion	115
6.2 Two possible layouts to deflect energy to the detector	118
6.3 Comparison of energy readings for mirror-leakage method	119

LIST OF FIGURES

6.4	Measured voltage on custom energy meter	120
6.5	Theoretical voltage on custom energy meter	122
6.6	Comparison of custom energy meter vs. Ophir's	123
6.7	Photograph of DTC	124
6.8	DTC response to target temperature changes	128
6.9	DTC response to noise in temperature readings	128
6.10	Breadboard temperature against time	129
6.11	Energy against time in rear mirror position scan over 20 hours	131
6.12	Energy temperature feedback algorithm	133
6.13	Pulse energy with active feedback	134
6.14	Pulse std. dev. with active feedback	134
7.1	Photograph of dragon hologram	139
7.2	High resolution hologram of a futuristic tank	139
A.1	Program for cropping images with a sliding window	150
C.1	Original hologram printer with LCD	154
C.2	Hologram printer with LCOS	155
C.3	Layout of Hologram Printer	156
C.4	Layout of Hologram Printer with dimensions	157
C.5	Length adjustment system	158
C.6	Object lens system on printer	159
D.1	Program for White Logo analysis	161
E.1	Lens system for imaging LCOS Fourier image	163
E.2	Compound Lens L2	163
E.3	Compound Lens L3	164
E.4	Compound Lens L4	164
E.5	Objective Lens system, ray traced	165

LIST OF FIGURES

F.1	Side-on orthogonal view of mechanical mount for LCOS and split beam polariser	167
H.1	Photograph of laser, powersupply and cooling unit	171
H.2	Photograph of laser case	171
J.1	Photograph of part of the hologram printer	183
J.2	Photograph of me working on the hologram printer	184
J.3	Photograph of LCOS section of the hologram printer	185
J.4	Photograph of short cavity laser	186

List of Algorithms

- 1 Printing algorithm suitable for printing at low speed 96
- 2 DTC feedback using PID algorithm 126

List of Acronyms

SLM Spatial Light Modulator. A device that spatially modulates a beam of light.

EASLM Electrically Addressed Spatial Light Modulator. A SLM display that is electrically (as opposed to optically) controlled, typically by a computer.

LCD Liquid Crystal Display. In this usage, a transmissive EASLM display that spatially modulates the beam intensity.

LCOS Liquid Crystal On Silicon. A reflective EASLM display that spatially modulates the beam phase. Used in conjunction with a polariser to modulate the intensity.

Nd:YAG Neodymium Doped Yttrium Aluminum Garnet. A lasing material used in near-infrared lasers.

VSYNC Vertical Synchronization. Matching a display (such as an SLM) refresh rate.

CW Continuous Wave. A laser beam that is continuous, rather than pulsed.

3D Three-Dimensional. A three dimensional object or image.

2D Two-Dimensional. A two dimensional image, without depth. Such as a photograph.

LIST OF ACRONYMS

- 2.5D** 2.5 Dimensional. An image with, typically, horizontal but not vertical parallax.
- CCD** Charge-coupled device. A device that enables electric charges to be transported through successive capacitors controlled by a clock signal. Used mainly for sensors that capture and record light.
- DTC** Digital Temperature Controller. The name we gave to the PCB that heats and measures the temperature of a component.
- PCB** Printed Circuit Board. A board for supporting, mounting and connecting electronic components.
- PID** Proportional Integral Derivative. A standard algorithm to change an output in response to an input.
- ID** identification number. Assigned unique number for identification.
- USB** Universal Serial Bus. A serial bus standard for communication between devices.
- PC** Personal Computer.
- A-D** Analogue-Digital.
- EIA** Electronics Industry Alliance. A trade organization for electronics manufacturers in the United States.
- DPI** Dots Per Inch. The number of dots (pixels) per linear inch.
- RGB** Red Green Blue. Three additive primary colors.
- I/O** Input/Output. Input and output data streams.
- OS** Operating System. The software that manages the computer's hardware resources.

LIST OF ACRONYMS

NDF Neutral Density Filter. A darkened piece of glass used to decrease the energy of a laser beam.

(Page numbers indicate the first use of the variable)

Hologram printer components

The components in the hologram printer are labelled uniquely throughout the thesis. See Appendix C for full page schematic labelled diagrams.

L1	Lens between microlens array and LCOS.
L2	First compound lens in relay telescope to image LCOS to plane I2
L3	Second compound lens in relay telescope to image LCOS to plane I2
L4	Objective compound lens, to image the Fourier plane of I2 onto I3
L5	First lens in afocal telescope in object beam to magnify the beam
L6	Second lens in afocal telescope in object beam to magnify the beam
L7	Acts with lens L8 to image I4 to I3
L8	Acts with lens L7 to image I4 to I3
L9	Acts with lens L10 to image aperture to image I4
L10	Acts with lens L9 to image aperture to image I4
LCOS	LCOS display system
I1	Real focal image plane inside relay telescope
I2	Real focal image plane inside relay telescope
I3	Real holopixel plane. Fourier transform of LCOS
I4	Real image plane of aperture
I5	Focal plane of L10 and L9 - aperture placed here to clean beam
A	Microlens array
a	Optical distance from microlens array to lens L1
b	Optical distance from lens L1 to LCOS, via mirror and cube polariser
c	Optical distance from LCOS to lens L2 via split beam polariser
d	Optical distance from lens L2 to image plane I1
e	Optical distance from image plane I1 to lens L3
f	Optical distance from lens L3 to image plane I2

g	Optical distance from image plane I2 to lens L4
h	Optical distance from lens L4 to image plane I3
j	Optical distance from image plane I3 to lens L7
k	Optical distance from between lenses L7 and L8
m	Optical distance from lens L8 to image plane I4
n	Optical distance from image plane I4 to lens L9
y	Width of aperture on microlens array A
z	Distance between aperture and microlens array
Laser	Laser mounted on breadboard

Equation reference

Sensitivity analysis

Provides a measure of the sensitivity of a function with respect to one of its input variables. A value of $\ll 1$ means the output of the function is very insensitive to changes in the variable. A value of $\gg 1$ means that the output of the function is very sensitive to changes in the variable.

$$\text{Relative sensitivity of } f \text{ w.r.t. } x = \frac{x}{f} \cdot \frac{\partial f}{\partial x} \quad (1)$$

Lens equations

The thin lens formula in air is:

$$\frac{1}{S_1} + \frac{1}{S_2} = \frac{1}{f} \quad (2)$$

Where S_1 is the distance between an object plane and a thin lens with focal length f and S_2 is the distance between the thin lens and the image plane.

For two thin lenses with focal lengths f_1 and f_2 respectively, separated by an optical distance of $f_1 + f_2$, the final convergence of the beam is not altered (making it afocal), but the width of the beam is magnified by a factor M of:

$$M = -\frac{f_1}{f_2} \quad (3)$$

Small angle approximation for paraxial rays:

$$\sin(\theta) \approx \theta \quad (4)$$

Matrix method for lens system analysis

The matrix method for lens system analysis works on the basis that a thin-lens system can be described with a matrix, M . The input vector, $\mathbf{v}_{\text{input}}$, is modified by the matrix to produce the output vector, $\mathbf{v}_{\text{final}}$ as so:

$$\mathbf{v}_{\text{final}} = M \cdot \mathbf{v}_{\text{input}} \quad (5)$$

Vector for light ray at height r and travelling at angle θ from the horizontal (From Chartier [1, pages 120-130]):

$$\mathbf{v} = (r, \theta)^T \quad (6)$$

Transfer matrix for ray travelling distance b in constant medium:

$$M = \begin{pmatrix} 1 & b \\ 0 & 1 \end{pmatrix} \quad (7)$$

Lens matrix for ray travelling through a thin-lens with focus f :

$$M = \begin{pmatrix} 1 & 0 \\ -\frac{1}{f} & 1 \end{pmatrix} \quad (8)$$

Matrix for surface with initial index of refraction n_1 , final index of refraction n_2 and curvature R :

$$M = \begin{pmatrix} 1 & 0 \\ \frac{n_1 - n_2}{R \cdot n_2} & \frac{n_1}{n_2} \end{pmatrix} \quad (9)$$

1

Introduction

1.1 Holography

To watch a person's first interaction with a hologram is a truly fascinating experience. They cannot help but try to reach out and touch the object that they can see projected out in front of them, but know is not really there. A large full colour hologram can be a beautiful, albeit expensive, piece of artwork, projecting a Three-Dimensional (3D) holographic image producing all of the visual impressions of depth and realism that is found in real scenes. Holography has traditionally required a real object from which to make the hologram, but recent advances in digital holography have allowed the production of realistic holographic images of scenes and objects that exist only in the mind of the artist. Digital holography is already being used in numerous applications - from artwork, to product advertising, to data visualization.

Holography is the technique of recording 3D images by recording and replay-

1.1. HOLOGRAPHY

ing optical wavefronts. Gabor et al. [2] developed the mathematical toolkit for holography just under 50 years ago. It took a further 20 years for technology to advance sufficiently to allow researchers to reliably produce 3D holograms using a laser[3]. Optical holographic imaging is the traditional technique of first illuminating a firm rigid object with a coherent laser source. The scattered light from the object falls upon a coated plate, interfering with a second mutually-coherent beam. The resultant microscopic interference pattern is recorded by the high resolution light sensitive emulsion on the plate[3, 4]. After chemical development, the plate can be viewed to reveal a 3D image of the original object, on a 1:1 scale.

With the goal of producing holograms that were not 1:1 scale images of real objects, researchers looked at using Liquid Crystal Display (LCD) displays as a replacement of the real object. Although these produce an inherently Two-Dimensional (2D) image, by printing millions of different 2D images in a dot-matrix style with a suitable image transformation, a 3D or 2.5 Dimensional (2.5D) hologram image can be composed.

This thesis investigates possible improvements to an existing digital monochrome holographic printer. The architecture of a digitally-based holographic printer is directed by three main goals: (1) To produce holograms of models created on a computer by an artist with no special knowledge of holography, (2) to have as high a resolution, contrast and fidelity as possible, and (3) to produce said holograms at a commercially viable rate and cost.

1.2 Overview of thesis

The following original research is documented in this thesis dissertation:

- A description of a digital hologram printer, intended to aid with the production of a practical hologram printer.
- An analytical examination of the two main components of the lens system, allowing for the final pixel size and shape to be predicted accurately, and thus predicting the energy density on the holographic film. The problem of speckle is also addressed and qualitatively assessed. This knowledge becomes crucial for increasing the resolution, and thus decreasing the pixel size.
- Mechanical and software improvements to a holographic printer design based upon a sensitivity analysis, qualitative experience, and quantitative research.
- The architecture and implementation of a temperature-energy feedback system designed to improve stability of the pulsed laser, a key component in the holographic printer.
- A case study analysis of the unwanted side effects of the angular intensity distribution of a hologram pixel on its apparent intensity.
- Demonstration of improvements to produce a high resolution hologram, recorded at 532 nm.
- Demonstration of the feasibility of using a high contrast reflective Liquid Crystal On Silicon (LCOS) display system over the older lower contrast transmissive LCD display system.

The following **Background** chapter provides a brief historical overview of holography, focussing on the path that led to digital holography, as well as a more detailed look at recent research in the field of digital holographic printers.

2

Background

2.1 Definition

What is a hologram? The term hologram has been used (often incorrectly) to mean many things – encompassing everything from a projected 3D image floating in the air, to lenticular posters, to sparkly Christmas wrapping paper.

The Merriam-Webster dictionary defines it as:

‘A three-dimensional image reproduced from a pattern of interference produced by a split coherent beam of radiation (as a laser);’

For the purposes of this thesis, a hologram is defined to mean that the viewer can see an apparently Three-Dimensional virtual image with at least horizontal parallax when looking at a hologram device with the image being produced from a pattern of interference.

For a better understanding of how a hologram works, a brief look at the his-

2.2. A BRIEF INTRODUCTION TO PHOTOGRAPHY

tory and theory of traditional photography is required.

2.2 A brief introduction to photography

A traditional photograph is created when ordinary white light is captured by a light sensitive emulsion attached to some substrate. A camera captures light that is emitted or reflected from the target objects and is focused by a series of lenses to create a real image on the emulsion. The emulsion is made of a light sensitive mixture (typically involving silver or chalk) that undergoes a chemical reaction whose reaction rate has some approximately linear correlation to the intensity of the light incident upon it. The film can then undergo wet chemical processing to make a permanent image.

In this way, the film captures the intensity of the light. Phase information about the light is discarded, requiring that a particular point in the scene is set permanently as the focus point.

1724. J.H. Schultz discovered that some silver salts, for example silver chloride and silver nitrate, darken when exposed to light.



Figure 2.1: First permanent photograph, by Niépce in 1826 (Public domain)

2.3. HISTORY OF HOLOGRAPHY

1826. It took over a hundred years before Joseph Nicéphore Niépce used the silver salts to make a permanent photograph based on these principles (See Figure 2.1 on the preceding page). It took 8 hours to expose this photograph.

1840. Talbot [5] developed a process to create a negative image first, creating the today-common nomenclature ‘photograph’, ‘negative’ and ‘positive’.

1851. Archer [6] discovered¹ by using a process he coined the Wet Plate Collodion process the exposure time could be drastically reduced.

1884. Eastman et al. [7] invented the photographic film, replacing the photographic plate.

1975. Analogue photography does not change fundamentally until modern digital photography is invented. Dillon et al. [8] uses solid-state Charge-coupled device (CCD) image sensor chips to capture an image.

1990. The first true commercial digital camera is released – the Dycam Model 1; using an improved CCD image sensor.

2.3 History of holography

This section looks at development of the field of holography. Holograms in many different forms have been developed in the second half of the 20th century. The basic idea idea has always been the same – to create a diffraction grating on some material in a way that ultimately ends up with a viewable picture.

Arguably a hologram is synonymous with a diffraction grating – at the technical level they are the same thing. But the distinction is analogous to the difference between a painting and a piece of paper with paint on it. The latter is technically the same as the painting, but may contain no picture or image that can be interpreted by a human eye.

¹For historical accuracy, I feel obliged to note that the Collodion process was first suggested by Mr. Le Gray[6] but published by Archer first.

2.3. HISTORY OF HOLOGRAPHY

Because of the technical similarity between a hologram and a diffraction grating, the advances of each tend to go hand-in-hand. So to give an explanation of holography, a brief description of a diffraction grating is in order.

A diffraction grating is a surface covered by a pattern of parallel lines, with the distance between the lines ideally of the order of the wavelength of visible light. Light incident on the diffraction grating is bent or reflected due to diffraction, or absorbed. The light acts as a wave, to produce a image or a pattern. Most literature considers diffraction gratings with a series of regularly space lines, producing just a change in angle of the light. However throughout this thesis the term diffraction grating will refer to a more general grating with an arbitrary-spaced series of lines.

A brief history of the diffraction grating:

Approx 1660. James Gregory noticed that bird feathers produced diffraction patterns, creating iridescent colors. Reflection diffraction gratings appear quite commonly in nature, from butterfly wings, to peacock feathers and even many beetles. Birds, for example, grow their feathers in such a way as to form a diffraction grating, creating a beautiful visual effect in order to attract mates.

1785. The first man-made diffraction grating was made around 1785 by David Rittenhouse, who used 50 hairs strung between two finely threaded screws.

1803. Thomas Young used two thin slits to demonstrate that light behaves as a wave, diffracting and constructively and destructively interfering – principles fundamental to the field of holography.

1821. Joseph von Fraunhofer produced a diffraction grating using a similar method to that which Rittenhouse used, but using wire (Figure 2.2 on the next page). Fraunhofer used his diffraction grating to discover the absorption 'Fraunhofer lines' in the solar spectrum [9].

With the wave-like nature of light starting to be understood, the stage is set

2.3. HISTORY OF HOLOGRAPHY

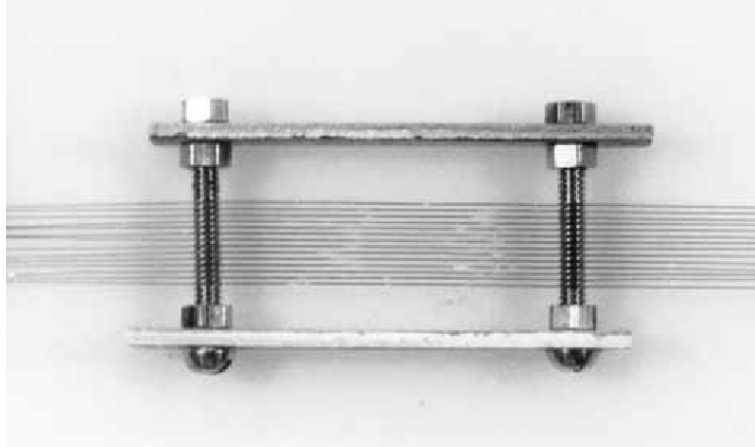


Figure 2.2: Wire diffraction grating, similar to that made by Fraunhofer for invention of holography. This starts with Dennis Gabor (Figure 2.3 on the following page) in 1947.

Dennis Gabor was a brilliant British/Hungarian scientist with an interest in the way that light behaves. Even as a child he was fascinated by Abbe's theory of the microscope and by Gabriel Lippmann's method of color photography.

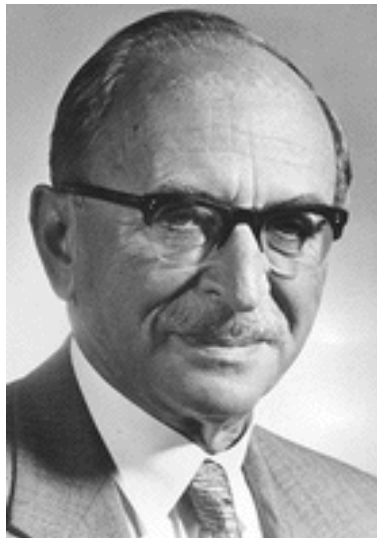


Figure 2.3: Dennis Gabor

Before he had entered university, he had already repeated many modern (at that time) experiments on wireless X-rays and radioactivity, with his brother George Gabor.

He moved to Germany for his education, and during his time at university, he

2.3. HISTORY OF HOLOGRAPHY

invented one of the first high speed cathode ray oscillographs, and made the first iron-shrouded magnetic electron lens. He worked for a while in this field, but left Germany when Hitler came into power. He ultimately ended up in England, and despite the depression managed to find work at a research company, British Thomson-Houston Co., where he would work for many years.

1946. During his time at the company, Gabor et al. [10] wrote the first papers on communication theory, as well as many other subjects. Although on the surface it seems that communication theory has nothing to do with creating pretty 3D images, it actually the underlying theory of how holography works. Gabor [11] went on to first develop stereoscopic cinematography, and then on to creating basic flat holograms – although at the time his was goal was to improve the resolution of the electron microscope [12, 13, 14].

The first hologram made by Gabor was an in-line plane transmission hologram [15]. In-line means that the reference beam and object beam come from the same direction. This was a requirement for Gabor because his light source was a mercury arc lamp. The light was filtered (he used the 546 nm mercury green line) and squeezed through a pinhole to make it quasi-coherent. The resulting light had a very small coherence length – just enough to make an in-line hologram.

A plane hologram, as opposed to a white-light hologram, means that the hologram has to be reconstructed (viewed) in the same monochromatic light.

A transmission hologram is one which is viewed with a light being transmitted through the hologram. The replay light (the light to view it again) has to illuminate the hologram at the same angle, but in the opposite direction, that the reference beam was at when exposing the hologram. The virtual image of the object appears at the original object position. Since for in-line holograms the object and reference beams come from the same direction, this meant that to view Gabor's in-line holograms, the viewing light had to be shining straight into the

2.3. HISTORY OF HOLOGRAPHY

viewer's eyes, or else projected onto a surface [16]. And for Gabor, this viewing light had to be his dim filtered mercury-arc lamp.

Despite the problems with his holograms, Gabor et al. [2] had proved that the interference pattern carries all the information about the original object, and that from the interference pattern you can reconstruct the entire image of the original object. It was for these concepts that in 1971 Gabor was awarded the Nobel Prize for Physics.

Although the first holograms were very interesting, and generated some talk in the scientific world, Gabor was much too early. Lasers still had not been invented, and the reliance on mercury arc lamps meant that it took several hours to expose even a small hologram.

1958. Another key player in the development of the field of holography was Yuri Denisyuk (Figure 2.4). Denisyuk was a Russian scientist that started the work on 'interference photography' (2D holograms) in 1958. After several years he published his work in the Soviet Union, however it was largely ignored.



Figure 2.4: Yuri Denisyuk

An American professor, Emmett Leith, who happened to be the same age as Yuri, independently also created a hologram (Leith and Upatnieks [17]). This sparked off an interest in holography in the US, bringing attention on to Denisyuk's work.



Figure 2.5: Theodore H. Maiman

But Leith's original work was still restricted to using Mercury arc lamps, holding back development of the field in general. Fortunately this situation only lasted a couple of years.

1960. The laser was invented. Maiman (Figure 2.5) created the first laser (*light amplification by stimulated emission of radiation*) providing a powerful source of the coherent, monochromatic light[18, 19]. This reduced the required hologram exposure times from many hours to a few seconds, not to mention the huge impact it had on almost every aspect of science.

Maiman's laser was based on a synthetic ruby crystal, and built in Hughes Research Laboratory. Its importance was immediately recognized, and the legal rights were fought over.

Maiman left the company to form his own company, Korad, to build lasers and to further develop the technology.

1962. Leith and Upatnieks experimented with the lasers to also create transmission holograms. Originally these were also in-line transmission, bringing along all the mentioned problems with viewing such a hologram. However the laser had a much longer coherence length, allowing them to independently discover off-axis holography (Gabor had already proposed this some 12-14 years before). Off-axis holography is a technique where the laser beam is split into an

2.3. HISTORY OF HOLOGRAPHY

object and reference beam. The object beam illuminates the object, and is scattered onto the film. The mutually coherent reference beam is shone onto the film, from the same side but at a different angle. The two beams interfere and the interference pattern recorded. This means that on replay, the reconstructing beam is no longer coming from the same place as the virtual object.

Leith and Upatnieks [20, 21] applied communication theory [10] and the reconstruction process of Gabor et al. [2] to produce a mathematical analysis of wavefront reconstruction in three dimensions.

1968. Two-step white light transmission holography, also known as rainbow holography, is invented by Stephen Benton [22]. This technique allowed transmission holograms to be viewable in ordinary light. Benton et al. [23] went on to discover one-step white light transmission holography.

At this stage, holography begins to branch out and to really take off. The problem with creating the holograms optically is that it requires an actual physical object, and that the object must be of the same size as the hologram. The larger the object, the more difficult it is to keep it stationary (To within an order of the wavelength of light) during an exposure, and the more powerful the laser required. Objects up to the size of a car could be just about be created, taking many hours to expose, but holograms of people and natural soft objects was impossible. The invention of the pulsed laser, and thus pulsed laser holography, happened rather quickly, allowing for moving objects to captured (For example portraits of people by Bjelkhagen [24]).

De Bitetto [25] invents a new method of creating a hologram using slits. The motivation is that the eye only requires horizontal parallax in order to see something as '3D'. De Bitetto [26] showed that by using a thin vertical slit held against the film, with a photograph or other image behind it, a realistic hologram could be made. This technique has an additional benefit that there is no chromatic aberration due to the vertical parallax.

2.3. HISTORY OF HOLOGRAPHY

A basic holographic printer utilizing an LCD screen [27] used an optical vibration isolation table with a split-beam Continuous Wave (CW) laser. The object beam transmissively illuminates an LCD screen and projects the image onto a diffusive screen. This screen acts as the object in traditional holography illuminating the hologram plate. However only a small area of the hologram plate is illuminated – the rest is blocked off with a large slit aperture. The image is changed on the LCD screen, and another area of the hologram plate is illuminated. In this fashion the hologram plate is exposed to multiple images – each image offering a slightly different perspective. The images can be either taken by a camera or be computer generated.

The mutually-coherent reference beam is arranged to simultaneously illuminate the hologram plate, generating the required wave-interference spatial pattern on the light sensitive emulsion. The area exposed for illumination can be one of 2D array of rectangles/squares, producing full-parallax holograms at the cost of longer print times, or one of a 1D array of slits, producing single-parallax holograms.

This technique however relies on a CW laser and a diffusive screen, making it very sensitive to vibrations.

McGrew [28] side steps the need for a diffusion screen by directly exposing the laser light onto the holographic plate. But this still suffers from vibration problems.

1969. Benton develops the rainbow hologram, requiring two recording steps (termed two-step holography). A master hologram is recorded from a real object with conventional off-axis holographic techniques. The rainbow hologram is then recorded from the image of the master [27].

The technique of recording a master hologram offers a significant advantage; it allows for the mass production of the rainbow hologram without the physical object, making commercial holography a real possibility. Commercial ma-

2.3. HISTORY OF HOLOGRAPHY

chines are still available today for the purpose of mass production from a master hologram[29]. Two-step holography also has various beneficial side-effects. Because the recording of the hologram is done in two steps, the copy can be a slightly blurred version of the master, hiding any pixillation effects, hiding any seams, etc. It also allows objects in holograms to appear to lie both inside and outside the hologram plane, since the copy hologram can be placed in the master hologram's real object plane.

The draw back, however, is that two-step holography requires a high powered laser. The larger the hologram, the more powerful the laser required (or the longer the exposure time), as ideally the whole hologram needs to be copied at the same time. Two-step holography also introduces significant complexity into the design, making it impractical for a small studio.

Chen and Yu [30] used imaging by a lens to produce a one-step process for creating rainbow holograms in a single step. This method had the advantages that:

- Conceptually and mechanically fairly simple – a hologram can be directly printed.
- The laser does not need to be as powerful – a small part of the image can be exposed at a time , particularly when creating the hologram in slits.
- Tiling holograms is possible, to make particularly large holograms.
- Non-standard viewing windows are possibly.
- In the future, one-step holography could use dry-processing (e.g. photosensitive polymers [31])

1970. Salvador Dali used a ruby pulsed laser to produce holographic works of art. The quality of holograms increased rapidly over the years, as new emulsions were made available.

2.3. HISTORY OF HOLOGRAPHY

By this stage, people wanted more flexibility in what they could create holograms of. To create a hologram of a large building, say, or a fictional monster, a small miniature model had to be created.

One way to get around this was to make holograms of photos. King et al. [32] showed that by using a different photograph for each angle, the photographs could be optically multiplexed to compose a hologram. With this method a building or an outside scene could be effectively holographed².

By this time, computers were starting to become useful and available. For King et al. [32] and Kock [33], the next logical step was to use a computer to generate the images of a scene, and multiplex those images onto a hologram.

Late 1970's. An alternative technique to produce holograms of fictional objects, was to be more direct. Gabor had already shown, some 25 years earlier, that the interference pattern could be calculated. Using computers, or otherwise, the interference pattern for an arbitrary scene could be calculated, and then mechanically or chemically[34] etched in some way onto a material.

This now allows for the creation of holograms of arbitrary objects. A hologram of any object, real or fictional, can now be created, as long as you can work out the interference pattern for it.

There are many drawbacks to commercially producing holograms by mechanically etching on interference lines however. There is mechanical abrasion, resulting in requiring frequent tip changes and mechanical upkeep. It is also very slow to produce even small holograms, and the groove spacing is unlikely to be anywhere near the wavelength of visible light, resulting in a low fidelity hologram.

Despite the commercial drawbacks, it was a success in demonstrating truly that the interference pattern for an object could be calculated and a true hologram produced.

²Holographed – like photographed, but with holograms.

2.3. HISTORY OF HOLOGRAPHY

Briefly looking at the next twenty years of development in holography field:

1979. McGrew [35], working with the Diffraction Company, develops an embossing mass production technique for surface relief holograms. McGrew went on to form his own company, Light Impressions Inc, which was the first company to bring the embossed hologram to the commercial market with a set of embossed images of 3D subjects.

Early 1980's. Benton proposes the use of a movie camera mounted on a linear rail to obtain images of an object at different angle, as opposed to rotating object on turn table[36].

1988. F. Iwata and K. Ohuma, of Toppan Printing Co Ltd, made a novel process for making animated diffractive patterns by making lots of small tiny dots of gratings. Although crude, it is effective. It allows for very fine diffraction gratings, giving a high efficiency, while maintaining a crude control of the image (by deciding whether to put a dot in a particular place, etc.)

Davis [37] and Newswanger [38] independently improved on this by modulating the object, allowing crude 3D images to be built up of 'pixels'.

This thesis follows a similar method as pioneered by Davis and Newswanger – building up a hologram by printing in a 'dot matrix' style of 'pixels' in a grid. Throughout this thesis, the printed 'pixels' on the hologram will be referred to as holopixels, to emphasize their iridescent nature.

1992. By the early 1990's, computers and LCD screens were a lot more ubiquitous. Spierings and Nuland [39] replaced film in their Holoprinter with an LCD screen. Nuland and Spierings [40] went one step further over the course of a year, and make color 3D stereograms using an LCD in a single step

1994. Yamaguchi et al. [41, 42] describes a monochrome one-step holographic printer based on a CW laser. This can print small full parallax white-light reflec-

2.4. DIGITAL VERSUS ANALOGUE

tion holograms, but takes 2 seconds per pixel – e.g. 36 hours to do a reflection hologram of 320x224 holopixels.

1998. Some 20 years before, Fujio Iwata et al ([43, 44]) developed a mechanical machine to etch on diffraction gratings on to a substrate. They could calculate the diffraction gratings required by using Gabor's work done 25 years before them. Perlmutter [45] and Hamano and Yoshikawa [46] modernize the etching technique by using a high powered electron beam to etch the grating on. This reduces the mechanical wear and tear, and speeds up the process. However the electron beam is itself very expensive to produce and still very slow. It is also computationally difficult, requiring a significant amount of computing power.

2.4 Digital versus analogue

It is interesting to see the parallels between photography and holography. Both have become increasingly digitalized, with photography leading the way.

Photography, as we have seen, is traditionally the recording of the intensity of light on a light sensitive film. By using color filters we can also record the color of the light, allowing for a crude image suitable for the human eye.

The film can then be chemically processed, with the end result being an analogue photograph.

The analogue camera had various important drawbacks:

- The photographer is forced to wait a long time before the results of a shot can be seen. There were a few solutions – most notably the Polaroid camera which automatically developed the film straight after a photograph was taken.
- Film had to be bought continually – a re-occurring cost

2.4. DIGITAL VERSUS ANALOGUE

- Negatives also had to be stored along with the photographs in case reprints were needed at a later time.

There are many other factors to consider, and the debate between analogue and digital photography is still ongoing today.

The 1990s saw the advent of digital photography. Digital photography allowed for photographs to be captured with CCD based image sensors. The photographs could be modified and then printed to paper if needed.

3

Design of a digital hologram printer

This chapter considers the technical design of a digital hologram printer, beginning with a description of the optical and mechanical components for both the object and reference beam paths. The lens systems in the object beam are examined quantitatively, concluding with a straightforward set of instructions for adjusting the lens system. The chapter finishes with a qualitative examination of the lens system based on testing three different lens arrays.

3.1 Overview

Detailed is a digital hologram printer capable of recording transmission or reflection holograms in an off-axis geometry for subsequent developing and bleaching in order to produce white-light viewable holograms. The printer consists of: a pulsed laser source arranged to produce a visible-light laser beam; a lens system to direct each beam pulse to a photosensitive medium; a display system to

3.1. OVERVIEW

modulate the object beam; a two dimensional positioning track to position the photosensitive medium relative to said lens system; and a computer control system.

The use of a pulsed laser offers the advantage of printing without sensitivity to vibrations or slight temperature changes. The printer utilizes a long-cavity frequency-doubled Neodymium Doped Yttrium Aluminum Garnet (Nd:YAG) pulsed laser which can produce a stable second harmonic TEM₀₀ coherent 532 nm (visible green) beam.

The lens system splits the beam with a Brewster-angle polarising beam splitter into the mutually-coherent object and reference beams. The display system is a reflective LCOS display or a transmissive LCD, placed downstream of the object beam, and upstream of the photosensitive medium.

The use of a reflective LCOS as the display system for a hologram printer is particularly advantageous. The high efficiency and high contrast, compared to the less efficient transmissive LCD, allows ultimately for higher contrast upon hologram replay and increased energy economy during writing, allowing for a less powerful laser source to be used. The high resolution on the LCOS allows for the hologram to have a large depth of view.

Typically a silver halide green-light photosensitive emulsion on a glass substrate is placed upstream in the Fourier plane of the display system, recording the spatial standing diffraction pattern between the reference and object beams. This records a small 'pixel' of the order of 1 mm in diameter. The motorized two-dimensional positioning tracks translate the plate into position for the next pixel to be printed. The plate can then be developed and bleached chemically to produce a white-light viewable reflection hologram.

The hologram printer design outlined in this chapter is based upon the digital hologram printer detailed by Ratcliffe et al. [47]. The patent consists of the general schematic for a monochromatic hologram printer, but lacks key information required for implementation and modification. As is typical for any complicated

3.1. OVERVIEW

machine, intricate knowledge is required for correct fabrication; alignment mistakes will result in a bad hologram (e.g. containing dim, missing or bad pixels).

Because of the design's sensitivity to the layout, a methodical and detailed setup that incorporates previous experience is required. The patent also misses vital theoretical information required for modifying the machine. The lens system used around the microlens array and display system is sensitive to position. This chapter details the setup required to produce high-fidelity images while wasting the minimum amount of energy and controlling the energy density and pixel size of the beam exposed to the holographic plate. This is accomplished with a mix of quantitative and qualitative analysis of the lens system.

The basis of this work is the green pulsed-laser holographic printer detailed by Ratcliffe et al. [47] and illustrated in Figure 3.1 on the next page. The said hologram printer can print $1.0\text{ mm} \times 1.0\text{ mm}$ sized pixels onto a photosensitive glass plate at a maximum rate of 4 pixels per second. The majority of the energy from the laser is lost at various points in the design. The mechanical setup suffered from mechanical vibrations. The laser was also unstable with between 10% to 30% pulse-to-pulse variation in energy. This produces noticeable changes in the hologram. The goal of the work reported was to overcome these shortcomings, increase the printing speed and decrease the pixel size.

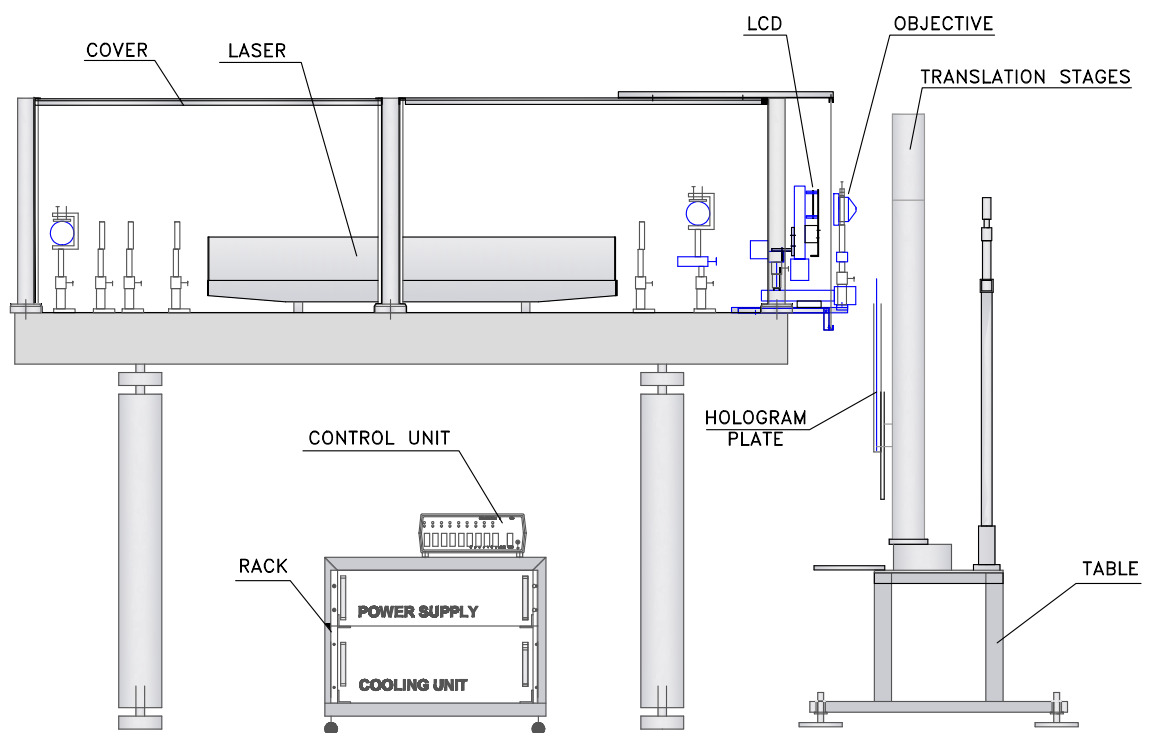


Figure 3.1: Hologram printer with LCD display system by Ratcliffe et al. [47]. For full-page schematics, see also Figure C.2 on page 155 and Figure C.1 on page 154.

3.2 Detail of system components

This section provides a detailed description for the building of digital hologram printer for writing composite 1-step holograms.

Figure 3.2 shows how the final hologram printer looked, after the various modifications, shown here for reference. The laser and various lens systems sit on an optical table. The second harmonic laser beam is split into two beams, and transported to the hologram plate. The object beam goes via the display system and the objective, while the reference beam is reflected off of the rear mirror and strikes the plate from the opposite direction. The hologram plate can be spatially translated by the pair of translation stages, to print each holopixel.

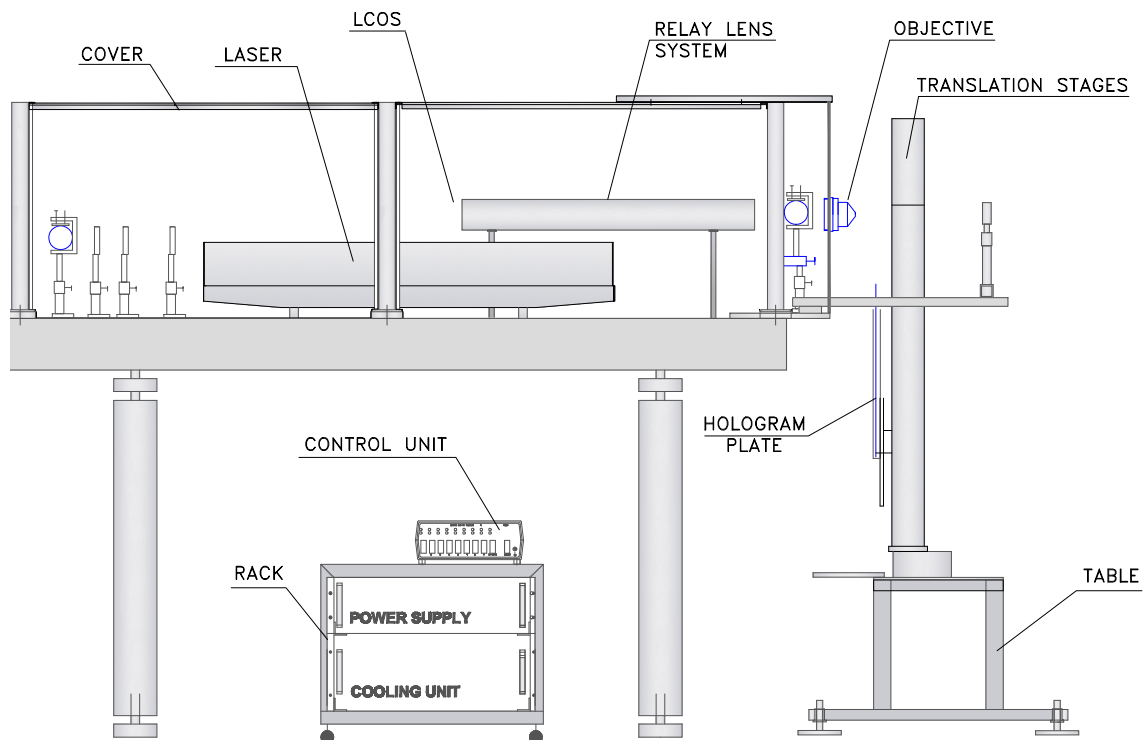


Figure 3.2: Side-on orthographic projection of final hologram printer design with LCOS display system. For full-page schematics, see also Figure C.2 on page 155 and Figure C.1 on page 154.

3.2. DETAIL OF SYSTEM COMPONENTS

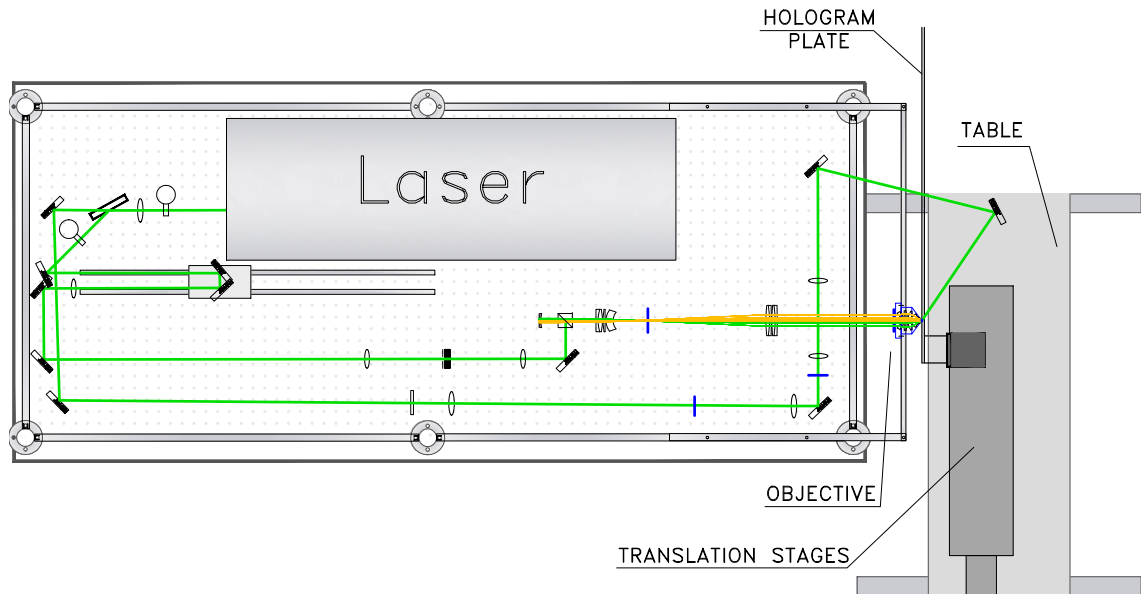


Figure 3.3: Top-down orthographic projection of final hologram printer design with LCOS display system. For full-page labelled schematics see also Figure C.3 on page 156 and Figure C.4 on page 157.

3.2.1 Laser system

Most lasers will rest on their own bread board which in turn stands on legs. The height of the laser can be adjusted; however it is a lot more flexible to adjust the height of the beam by using a system of mirrors instead.

The object beam is raised to the correct height using a triangle of three mirrors, each higher than the last. The beam then passes through a motorized half wave plate which rotates the polarization. The beam then passes through a Brewster-angle split beam polariser. The p-component of the laser light is transmitted through the split-beam polariser, while the s-component is reflected.

It is very important to get the angle of the Brewster polariser correct, otherwise circular polarization of the beam will result. To align correctly, the angle of the $\frac{1}{2}$ -wave plate is set to maximize the amount of reflected light (so that it polarises the light into the p-direction). This is best done by using an energy meter to measure the intensity of the light reflected from the split-beam polariser. By eye, check the profile of the transmitted beam is then checked. If the angle of the split beam polariser is wrong, the beam profile will look poor. The angle of the

3.2. DETAIL OF SYSTEM COMPONENTS

split-beam polariser is adjusted to minimize the intensity of the transmitted beam and produce a good Gaussian beam profile. In this setup the Brewster split beam polariser was coated with an anti-reflection surface, increasing the efficiency. For a non-coated split-beam polariser it is possible that the maximum transmitted energy is not at the Brewster angle [48]. In this case, the best results would probably be obtained by trying to maximise the quality of the beam, rather than the intensity.

3.2.2 Optics for transport of beams

Adjustable object beam path length

Figure 3.4 shows that the object beam is reflected between two sets of mirrors, with one set of mirrors mounted on a sliding base. This allows the distance between the two sets of mirrors (and hence the overall optical path length of the object beam) to be easily adjusted, while keeping the correct beam alignment.

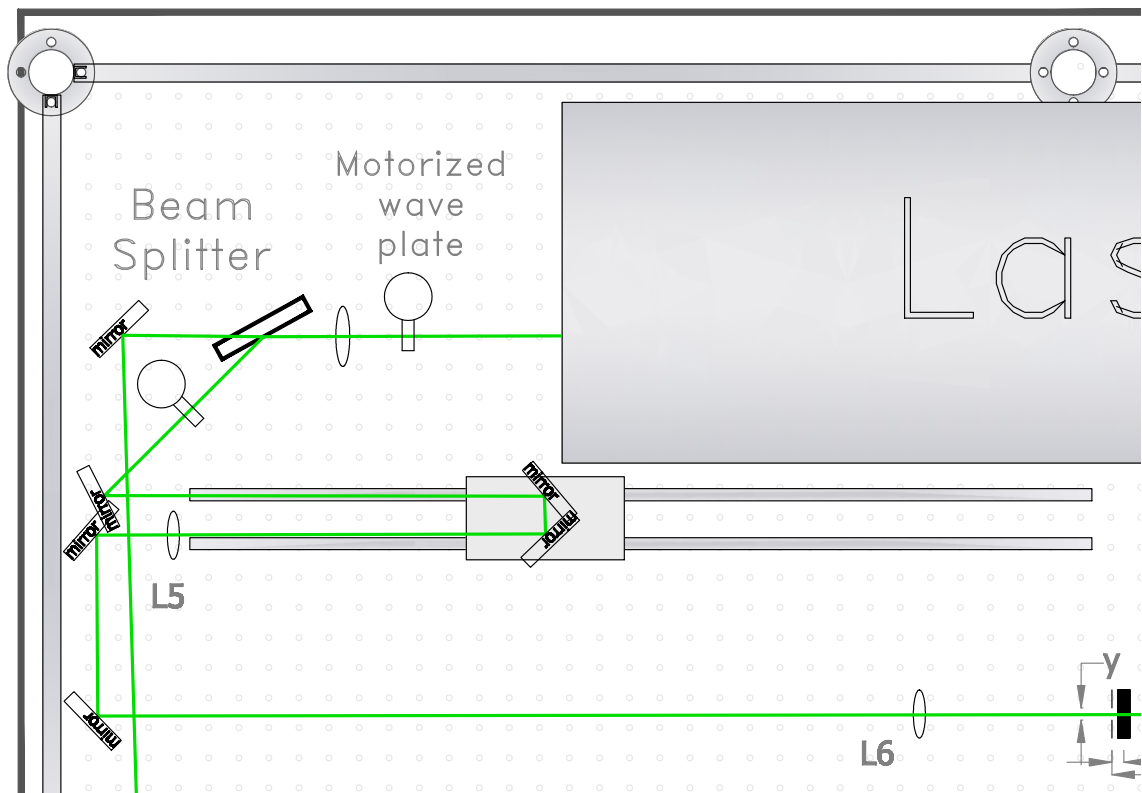


Figure 3.4: Top-down orthographic projection of system to adjust optical-path distance of object beam. See also Figure C.5 on page 158 for a full-page schematic.

3.2. DETAIL OF SYSTEM COMPONENTS

It is important to be able to modify the object beam path length such that the difference in distance travelled by the reference beam and object beam is kept as small as possible. This maximises the temporal overlap of the object and reference beam pulses at the hologram plate. If one beam arrives at the plate before the other, it will expose the plate without any signal, reducing contrast and diffraction efficiency upon replay.

To setup this system of mirrors, all four mirrors were mounted as indicated, with two of the mirrors on a sliding base. The base was moved back and forth while watching for beam movement. The angles of the four mirrors were adjusted until there was no perceptible lateral movement of the beam when the base is moved.

Cleaning up the object beam

To produce a clean Gaussian spatial profile of the object (and reference) beam if required, a pair of positive lenses (Marked L5 and L6 in Figure 3.4 on the preceding page) placed at a distance equal to the sum of their focal lengths can be used, with a pinhole aperture (not shown) placed at their mutual focusing plane to remove any high order defects. This afocal lens system can have the dual purpose of magnifying the beam as required, where the magnification of the laser beam, M_{laser} is dependant on the focal length of L5, f_{L5} and the focal length of L6, f_{L6} as:

$$M_{\text{laser}} = \frac{f_{L5}}{f_{L6}} \quad (3.1)$$

The beam can thus be magnified such that its diameter closely matches the downstream width of object beam aperture, to maximise overall beam efficiency.

3.2.3 Digital display system

In direct write analogue holography, the object beam illuminates a physical object. The illuminated beam is reflected off of the object, modulated by the object,

3.2. DETAIL OF SYSTEM COMPONENTS

and may be considered to scatter as a series of spherical waves. A photosensitive plate is positioned as to capture this light. A reference beam, also incident upon the plate, interferes with the modulated object beam creating a microscopic interference pattern (fringe pattern) that encodes the required information about the object. This fringe pattern is recorded on to the plate as an absorption hologram, to be developed and bleached to create a white light hologram. On replay of the hologram, the object image is reconstructed in its original position.

For digital holography the physical object is replaced with a computer controlled display system. This ultimately allows the production of a hologram using a computer generated model or a series of photographs or some other method that generates a series of suitable images. There are various methods for using a computer controlled display.

The display system used was a LCOS based Spatial Light Modulator (SLM); a small, reflective, high contrast, high fill-rate and high resolution panel. This has the advantages of a small form factor allowing for future miniaturization of the printer; high resolution allowing for holograms with a large depth of field (both in and out of the hologram plane); high efficiency rate increasing overall beam efficiency and allowing for a weaker laser to be used, thus decreasing the cost and increasing the lifetime of the printer; high contrast which in turn allows for high contrast holograms; and a high fill rate of up to 60 Hz, allowing for holograms to be printed at up to this rate of holopixels per second.

Figure 3.5 on the next page illustrates the logical layout required and Figure 3.6 on page 29 is a photograph of the microlens array system downstream of the LCOS.

3.2. DETAIL OF SYSTEM COMPONENTS

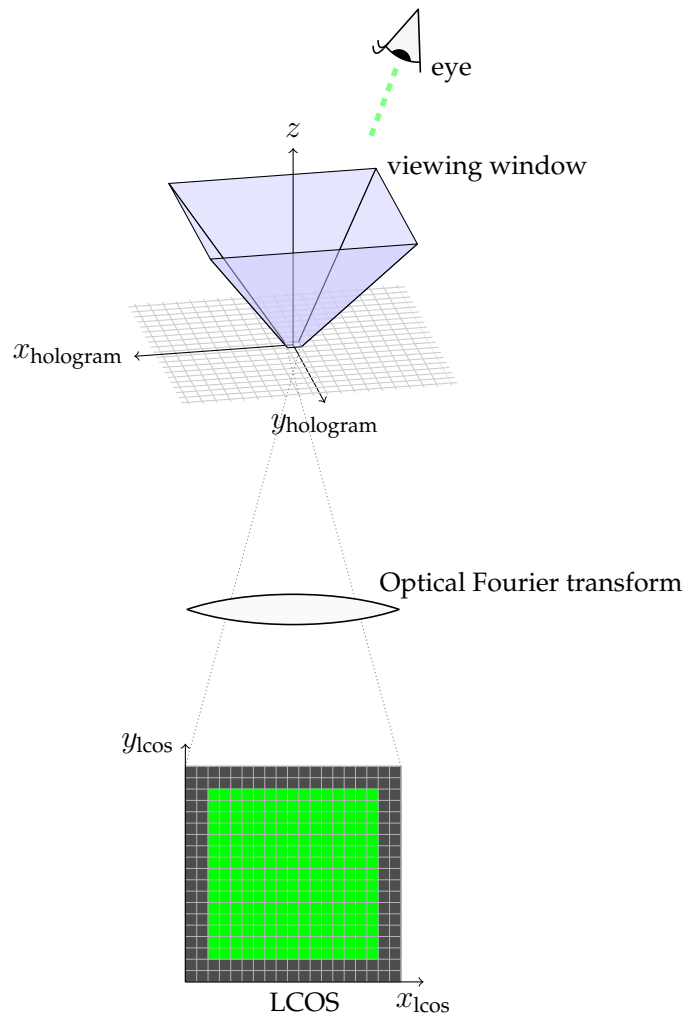


Figure 3.5: The Fourier transform of the image on the LCOS is printed on to the hologram as a single 'holopixel'. Upon replay of the hologram, this recorded Fourier image is reconstructed as an angular intensity distribution.

3.2. DETAIL OF SYSTEM COMPONENTS

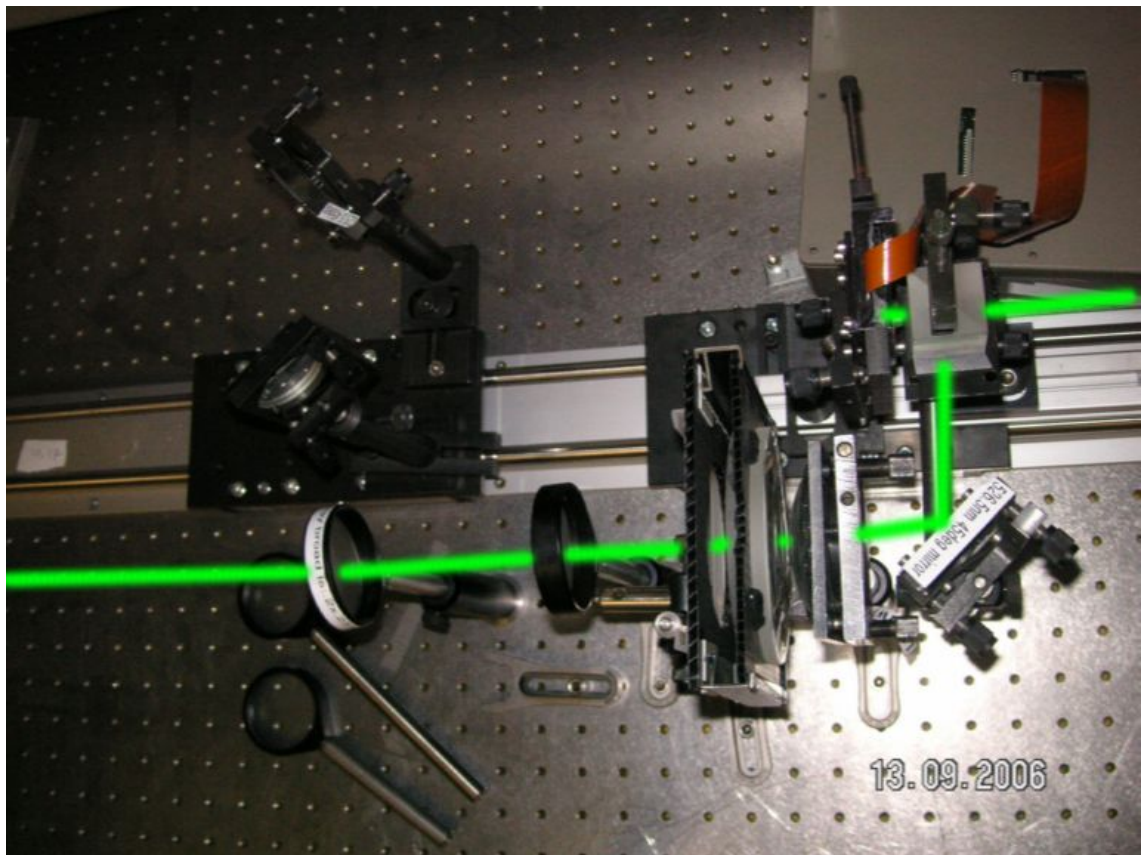


Figure 3.6: Birds-eye-view photograph of LCOS being illuminated, with the beam path indicated.

3.3 Analysis of lens system

The object beam is shaped according to several restrictions. The requirements are that:

- The beam exposes the LCOS uniformly and smoothly.
- Energy losses are minimized – the beam should illuminate the whole of the LCOS display while minimizing losses. Thus the beam profile should be rectangular and of the same aspect ratio and scale.
- The spatial profile of the beam at the plane of the hologram plate emulsion should be of a controllable size and shape. Typically either circular or square with a width of around 1 mm to 0.3 mm.

To achieve these aims, an afocal reversing telescopic lens system with an objective compound lens was designed and optimized using the lens software ZEMAX [49]. The lenses were designed and built by Marcin Lesniewski. The resulting setup is shown in Figure 3.7 on the next page.

The object beam is spatially filtered by the rectangular aperture P which has an aperture width y , as labelled in Figure 3.7 on the following page. The shape of the aperture will ultimately determine the downstream beam's spatial geometry (scaled in size by a factor $1/M_3$) of the pixel in the real image plane I1 and the real image labelled I3 where the photosensitive plate is placed.

The beam travels the distance labelled z to the microlens array A . This is a rectangularly-packed microlens array with spherically curved lenslets. The plane geometry of the lenslets in the microlens array determines the spatial shape of the beam on the LCOS display. Since the LCOS display system is rectangular, the lenslets are also chosen to be rectangular, with the same aspect ratio.

3.3. ANALYSIS OF LENS SYSTEM

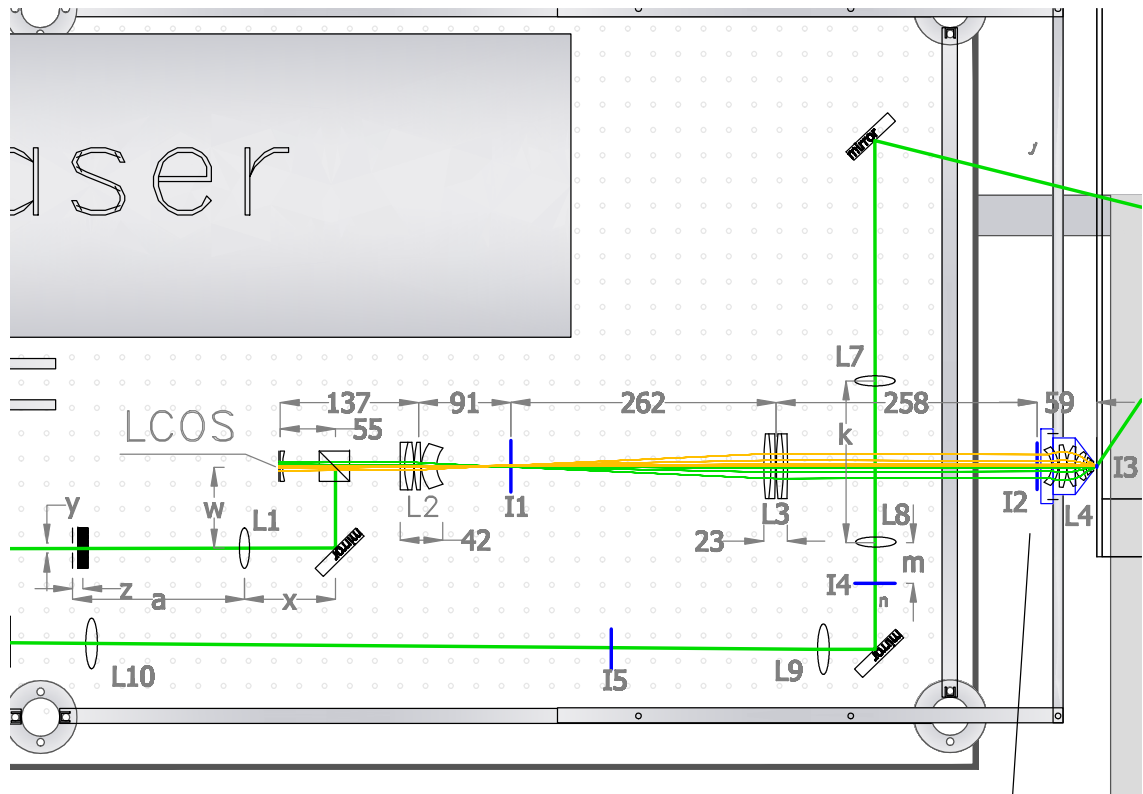


Figure 3.7: Top-down orthographic projection of object lens system in hologram printer. See also Figure C.6 on page 159 for a full-page schematic.

The expanded beam enters the positive lens L1 downstream of the microlens array, is reflected off the right-angled coated mirror, and continues to the polarising beam splitter.

The beam's polarization is already orientated in the direction such that all of the beam's energy is directed by the polarizing beam splitter to the LCOS display system. The lenses between the microlens array and LCOS are arranged such that the beam arrives at the display system with the correct spatial geometry and scaling to match the display region on the LCOS. Preferably the beam should have an even spatial beam intensity profile with minimal defects and speckle in order to produce a replay viewing window with an even intensity. It is conceivable to desire a non-even beam distribution (for example Gaussian) for the purpose of having a brighter optimal replay angle at the sacrifice of dimmer non-optimal replay angles. Such possibilities are not considered further here, and an even spatial beam intensity profile is assumed to be desired.

3.3. ANALYSIS OF LENS SYSTEM

The LCOS twists the polarization of the light at each pixel, to build up a spatial image. For a full intensity pixel, the polarization is rotated 90 degrees. For a black pixel, the polarization is not rotated. For greyscale, it is only partially rotated.

A thin weak lens in front of the LCOS display acts as a field lens to correct for the final image curvature so that the final image from the objective lens L4 is focused on a flat plane. A schematic for the physical mount for the LCOS display, field lens and beam splitter is given in Appendix F, Figure F.1 on page 167. The light beam, now containing the image that was on the LCOS, is now reflected back through the split beam polarising cube, splitting the image into an intensity encoded image and its negative. The negative bounces back along the original path, harmlessly being ignored. The positive image is then sent through a custom LCOS telecentric afocal reversing lens system to be projected on to the hologram plate.

The purpose of the LCOS lens system is to project the image of the LCOS onto a virtual hemisphere, mapping the two dimensional pixel spatial coordinates to longitude and latitude spherical coordinates, projected on to the holographic film.

Upon replay of the final developed hologram, each holographic pixel is iridescent – the brightness of the pixel changes with the angle at which it is viewed from, with the angular intensity profile matching the original spatial pattern that was on the LCOS.

This projection from the flat spatial plane (I1) at the LCOS to a hemispherical plane at the hologram plate (I3) is achieved with the telescopic afocal reversing lens system and objective lens. This lens setup is shown in Figure 3.8 and Figure 3.9 on the following page, with sample ray-traced light paths overlaid on the figure.

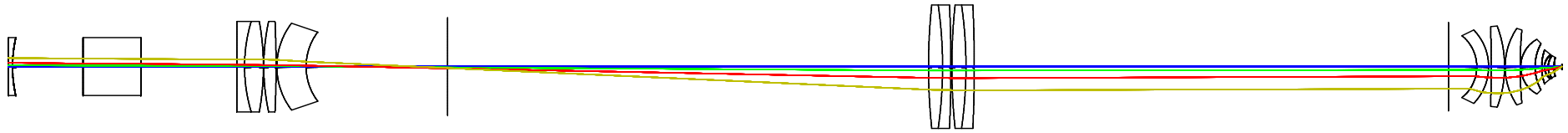


Figure 3.8: Ray-traced lens setup for object beam afocal telescopic reversing lens system. Rays drawn leaving parallel and spatially separated from the LCOS on the left and meeting at a point on the hologram plane on the right - the Fourier transform.



Figure 3.9: Ray-traced lens setup for object beam afocal telescopic reversing lens system. Rays drawn leaving from the same spatial point but at different angles from the LCOS on the left and striking parallel and spatially separated on the hologram plane on the right - the Fourier transform.

See Appendix E for more detailed ray-traced diagrams of this lens system.

3.3. ANALYSIS OF LENS SYSTEM

This complex system of lenses provides near diffraction-limited optical performance, requiring various different optical elements and several different glass materials to correct for various aberrations.

It is, however, desirable to derive a simple set of formulas that describes this lens system. This allows us to determine the effect of the set up of the optical system downstream, on the holopixel that is projected upstream. The size and shape of the final holopixel is determined by both the downstream lens system as well as the telescopic afocal lens system. The lens system was previously set up by a method of trial and error. This can produce adequate results for printing at large pixel sizes, however it is prone to error and makes it difficult to know what the ultimate holopixel size will be for a given lens setup.

For a large holopixel size (around 1 mm), setting up the lens system by eye is feasible and provides results of sufficient quality. However for smaller holopixel sizes (less than 0.5 mm), the system becomes increasingly sensitive to the exact placement of the lenses. Large uncertainties in the beam size translate to large uncertainties in the energy density on the photographic plate. Finding a 'sweet spot' for the correct pixel size and pixel fidelity frequently results in the beam size exceeding that of the optics, resulting in undesirable energy losses.

The purpose of this section is to provide an analytical approach to the problem. To do this, the telecentric afocal reversing lens system is treated as two overlapping relay telescopes. The compound lenses are ray-traced to determine their effective focal lengths. The small weak lens on the LCOS is a field lens for correcting the curvature on the final image, and is thus assumed to be negligible for these purposes.

Since the vertically polarised (the negative) part of the image from the LCOS is discarded by the polarised beam splitter, the phrase 'LCOS image' will be used to mean the reflected horizontally-polarised image (the positive), in order simplify the language required.

3.3. ANALYSIS OF LENS SYSTEM

Consider the image from the LCOS passing through the beam splitter and then continuing through the lens L2. It forms a real image at I1. By considering that L2 and L1 approximately form a relay lens system, it can be seen that the image at L1 will be that of the aperture P, scaled according to the lens relay formulas (considered later). The beam continues through L3, forming an image at I2. By considering that the lenses L3 and L2 form a relay lens, it can be seen that this image at I2 is the image of the LCOS, again scaled according to the lens relay formulas.

The system of lenses at L4 take the image at I2 and focus it at I3 which is thus the Fourier transform plane for the lens system L4. By considering that L4 and L3 form a relay lens, it can be seen that this image at I3 is the image that was at I1, and thus is an image of the aperture P, scaled twice by the two sets of relay lenses. The details of the lens are discussed in more detail later in Section 3.3.5 on page 40.

The image at I3 has a geometrically similar shape (i.e. the same shape but scaled) to that of that of P. It is also the Fourier transform of the image I2.

The thin lens formula in air is:

$$\frac{1}{S_1} + \frac{1}{S_2} = \frac{1}{f} \quad (3.2)$$

Where S_1 is the distance between an object plane and a thin lens with focal length f and S_2 is the distance between the thin lens and the image plane.

For two thin lenses with focal lengths f_1 and f_2 respectively, separated by an optical distance of $f_1 + f_2$, the final convergence of the beam is not altered (making it afocal), but the width of the beam is magnified by a factor of:

$$M = -\frac{f_1}{f_2} \quad (3.3)$$

Thus the object image plane at distance f_1 from the first lens will be relayed to the image plane at distance f_2 from the second lens and inverted.

3.3. ANALYSIS OF LENS SYSTEM

Compound lenses have a front focal length and a back focal length. The front focal length is the distance from the front surface to the principle upstream focal point. The back focal length is the distance from the back surface to the principle downstream focal point. While this is important for the placement and design of the compound lens, for the purposes of determining the magnification, the front and back focal lengths are not of particular interest.

The effective focal length for a compound lens is the distance from a principle plane to its corresponding principle focal point[50].

So if lens 1 has an effective focal length f_1 and is downstream of lens 2 which likewise has an effective focal length f_2 , and if their inner principle planes are separated by a distance of $f_1 + f_2$ then the image plane at a distance f_1 from back principle plane of lens 1 is magnified at the image plane at a distance $f_{2,f}$ from the front principle lane of lens 2 by a factor of:

$$M = -\frac{f_1}{f_2} \quad (3.4)$$

The object beam lens system is shown schematically in Figure 3.10 on the following page. Note that the actual path of the laser beam from lens L1 to the LCOS is via a mirror and the beam splitter. For diagram simplicity it is drawn as if the LCOS is transmissive. The distance labelled b should be interpreted as the optical distance from L1 to the LCOS.

Note that L2, L3 and L4 are compound lenses with different front and back focal distances. As is the convention in optics, the front is defined as in the direction of the beam, and back as the direction in which the beam came from.

This complex system of lenses is particularly sensitive to distances between L1 and L3, requiring an optical collimator for precise alignment. This can be done by mounting the LCOS and its weak correctional mirror together onto the moving platform at one end.

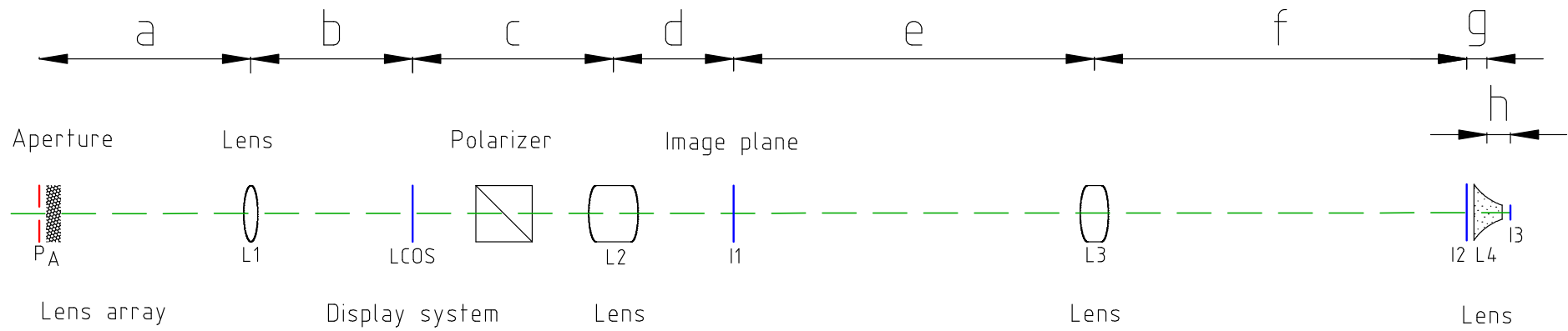


Figure 3.10: Logical diagram of optical beam path layout

3.3.1 Lenses L1 and L2

The object image plane at aperture P is at a distance of a from the center of lens L1, which has a effective focal length of f_1 . The distance from the aperture P to the closest principle plane of lens L1 should be approximately equal to the focal length, not exactly, such that the final pixel shape is a slightly defocused image of the aperture, producing a blurred outline on the hologram film.

The light then travels a total distance of $b + c$ to lens L2, via a mirror, beam splitter, a reflection off of the LCOS, twice passing through a small correction field lens on the LCOS, and back through the beam splitter.

The lenses L1 and L2 act together as an afocal relay lens, imaging the aperture P at the image plane I1.

It turns out that it is sufficient to use a thin lens at L1. Thus the principle plane is at the center of L1. The magnification due to L1 and L2, $M_{P,1}$, can be determined, given that the effective focal length of lens L2 is f_2 .

$$f_1 \approx a \quad (3.5)$$

$$f_1 = b \quad (3.6)$$

$$M_{P,1} = -\frac{f_1}{f_2} \quad (3.7)$$

3.3.2 Lenses L3 and L4

The lenses L3 and L4, with effective focal lengths f_3 and f_4 respectively, likewise act together as an afocal relay lens, imaging the image of the aperture P at I1 to the image plane I3. The image plane I1 is magnified by a factor of $M_{1,3} = -\frac{f_3}{f_4}$ at image plane I3.

The image plane P is magnified by a factor of $-\frac{f_1}{f_2}$ at the real image plane I1, and then magnified again by a factor of $-\frac{f_3}{f_4}$ at the real image plane I3. So the total

3.3. ANALYSIS OF LENS SYSTEM

magnification, $M_{P,3}$ of the aperture P at the image plane I3 is:

$$M_{P,3} = \frac{f_1 f_3}{f_2 f_4} \quad (3.8)$$

So the shape and size of P determines the shape and size of the final holopixel on the holographic film plate, magnified by a factor M_3 . The Zemax software determined the effective local length of the system from the LCOS display to the lens L4 to be $f_{\text{eff}} = -7.669$ mm. Thus:

$$M_{P,3} = -\frac{f_1}{f_{\text{eff}}} \quad (3.9)$$

$$M_{P,3} = -\frac{f_1}{-7.669 \text{ mm}} \quad (3.10)$$

$$= \frac{f_1}{7.669 \text{ mm}} \quad (3.11)$$

3.3.3 Lenses L2 and L3

For completeness, consider the lens system formed by L2 and L3. The image plane of the LCOS is relayed to the image plane I2 by lenses L2 and L3 with effective focal lengths f_2 and f_3 respectively. The image plane I2 has a magnification $M_{lcos,2}$ of:

$$M_{lcos,2} = -\frac{f_2}{f_3} \quad (3.12)$$

3.3.4 Focal length approximations

The surface properties of the compound lenses L2, L3 and L4 were calculated and optimized in the Zemax optics software¹. Table G.1 on page 169 in Appendix G details the lens materials, separation and clear diameter properties.

For lenses L2 and L3, the effective focal length of each of the lenses can be determined from the ray transfer matrices method (See Chartier [1, pages 120-130] and the Chapter Nomenclature on page xxi). Compound lens L4 is significantly more complex and has a much shorter focal length. As a result, the paraxial approximation is not valid for this lens, resulting in inaccuracies in the matrix method. The matrix method calculates the effective focal length of lens L4 to be 19.7 mm, whereas a geometrical calculation based on a raytrace produced by Zemax gives the effective focal length as 16.2 mm. This is shown in Figure 3.11 on the following page. To avoid such inaccuracies, the values calculated by Zemax were used exclusively.

3.3.5 Optical system for microlens array

There are additional factors to be taken into account because of the microlens array close to, and downstream of, the object beam aperture. Without the microlens array, the LCOS display would be illuminated with the 'raw' Gaussian beam. This means that any dust etc that was on any of the mirrors would appear as dark spots on the LCOS along with diffraction rings. The use of a microlens array acts a series of point sources which expand and overlap downstream, spatially averaging out the noise in the beam. The microlens array is also used to apodize² the beam's Gaussian spatial intensity profile into an even spatial intensity profile at the LCOS display.

Unfortunately the use of a microlens array introduces an additional problem

¹The Zemax software is owned by the ZEMAX Development Corporation [49] company and is used to aid in lens design.

²apodize – to purposely change the input intensity profile

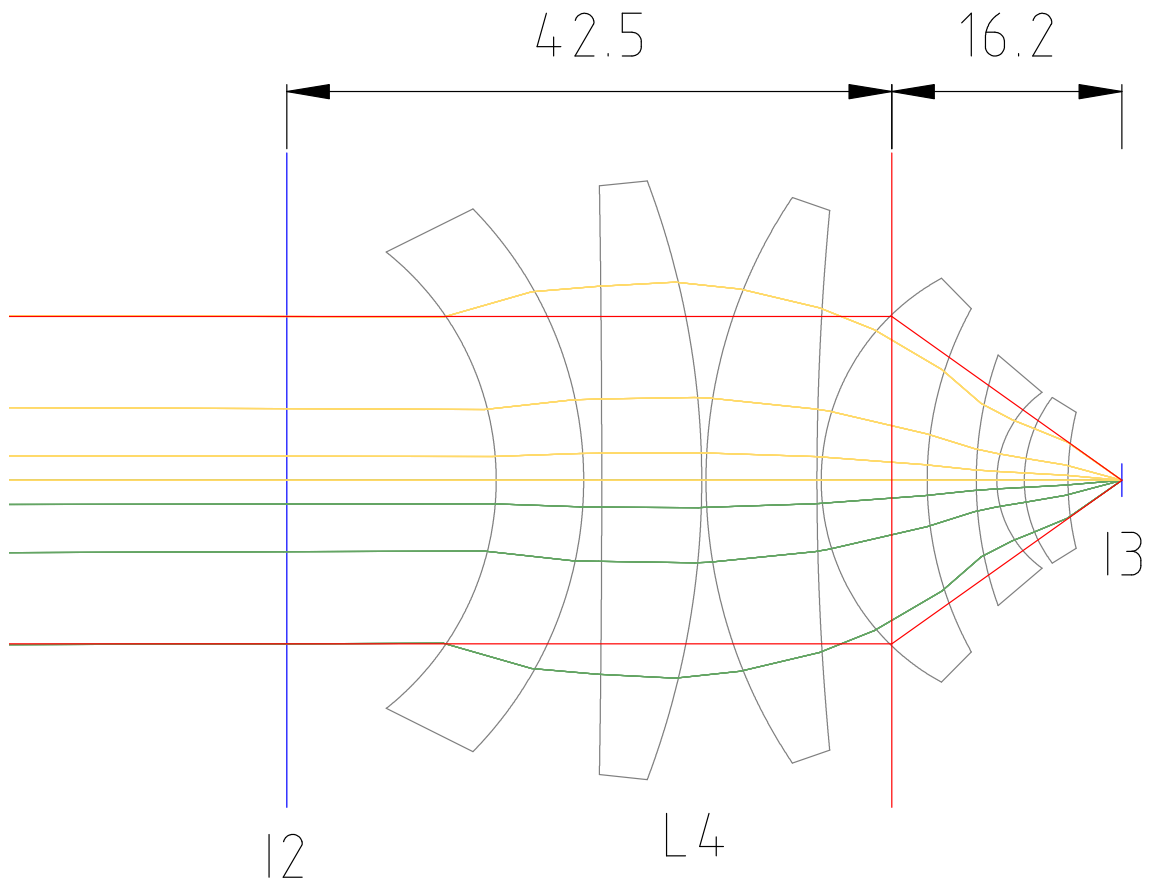


Figure 3.11: Effective focal length of compound objective lens L4 determined from construction lines (drawn in red). The focal length is determined to be $f_4 = 16.2$ mm. Focal lines and ray traced light paths determined with Zemax software.

3.3. ANALYSIS OF LENS SYSTEM

– the overlapping beams are coherent with each other and so interfere, giving a real speckled image. This speckle degrades the image of the LCOS and thus reduces the effective resolution. This will reduce the overall depth of field of the hologram when viewed.

The microlens arrays required in this design are rectangularly packed with an aspect ratio equal or close to that of the LCOS such that the downstream beam is similar in shape and size to the LCOS display. This rotationally asymmetric geometry results in rotationally asymmetric speckle. Rectangular speckle structures are observed in the downstream spatial profile.

In order to analyze the microlens array system, consider the meridional plane only (the vertical plane that crosses through the optical axis). The lenslets have the same aspect ratio as the LCOS and the size of the beam (as we will see later) will be a linear function of the lenslet size, so the beam will have the correct width if the height is correct.

The Gauss conditions will also be assumed and applied – that the beam is parallel to the optics. The assumption that the lenses are thin lens and that the angles are small enough that $\sin(x) \approx x$ will also be used.

First consider light rays travelling near the optical axis such that the rays pass through a lenslet centered on the optical axis. The ray passes through this central lenslet which has a focal length of f_{lenslet} . The ray then travels a distance of a (see Figure 3.10 on page 37), passing through the lens L1 which has a focal length of f_1 . The ray then travels a distance of b to illuminate the LCOS display. Using the thin lens approximation and the paraxial approximation, the matrix method can be used to examine this system (See Chartier [1, pages 120-130] and the Chapter Nomenclature on page xxi). Thus using a combination of lens and transfer matrices the path of the rays travelling through the central lenslet onto the LCOS can be described.

The matrix method requires an input ray, $\mathbf{v}_{\text{lenslet}}$ which can be described as

3.3. ANALYSIS OF LENS SYSTEM

$\mathbf{v}_{\text{lenslet}} = (r, \theta)^T$ where $2r$ is the height and θ is the angle that the ray is travelling from the horizontal. The resulting ray vector on the LCOS is thus $\mathbf{M}_{\text{lenslet}} \cdot \mathbf{v}_{\text{lenslet}}$, where the matrix M for this system is thus:

$$\mathbf{M}_{\text{lenslet}} = \begin{pmatrix} 1 & b \\ 0 & 1 \end{pmatrix} \begin{pmatrix} 1 & 0 \\ -\frac{1}{f_1} & 1 \end{pmatrix} \begin{pmatrix} 1 & a \\ 0 & 1 \end{pmatrix} \begin{pmatrix} 1 & 0 \\ -\frac{1}{f_{\text{lenslet}}} & 1 \end{pmatrix} \quad (3.13)$$

This can be extended to work for an arbitrary lenslet on the lensarray, by simply extending the ray vector as:

$$\mathbf{v}_{\text{lensarray}} = \begin{pmatrix} r & \theta & s \end{pmatrix}^T \quad (3.14)$$

Where r is the height, s is the height from the center of the lenslet that it is passing through, and θ is the angle that the ray is travelling from the horizontal.

Only the lenslet matrix is concerned with the d parameter so this parameter is dropped by the lensarray matrix.

The final matrix for the ray path from the lensarray to the LCOS, $\mathbf{M}_{\text{lensarray}}$, becomes:

$$\mathbf{M}_{\text{lensarray}} = \begin{pmatrix} 1 & b \\ 0 & 1 \end{pmatrix} \begin{pmatrix} 1 & 0 \\ -\frac{1}{f_1} & 1 \end{pmatrix} \begin{pmatrix} 1 & a \\ 0 & 1 \end{pmatrix} \begin{pmatrix} 1 & 0 & 0 \\ 0 & 1 & -\frac{1}{f_{\text{lenslet}}} \end{pmatrix} \quad (3.15)$$

From the matrix method[1], $\mathbf{M}_{\text{lensarray}} \cdot \mathbf{v}_{\text{lensarray}} = \mathbf{v}_{\text{lcos}}$ where \mathbf{v}_{lcos} is the ray vector at the LCOS. Solving:

$$\begin{pmatrix} r - \frac{(a+b) \cdot s}{f_{\text{lenslet}}} - \frac{b \cdot r}{f_1} + \frac{a \cdot b \cdot s}{f_{\text{lenslet}} \cdot f_1} \\ \frac{a \cdot s}{f_{\text{lenslet}} \cdot f_1} - \frac{r}{f_1} - \frac{s}{f_{\text{lenslet}}} \end{pmatrix} = \begin{pmatrix} r_{\text{LCOS}} \\ \theta_{\text{LCOS}} \end{pmatrix} \quad (3.16)$$

For the image of the aperture to be approximately focused, Equation (3.5) on page 38 established the condition that $f_1 \approx a \approx b$.

3.3. ANALYSIS OF LENS SYSTEM

To proceed, it is worth considering some practical implementation aspects. If $f_1 = b$ then the practical significance is that without the microlens array, a collimated beam would be focused by lens L1 to a tiny point on the sensitive LCOS. This means that if the microlens array is ever accidentally removed or knocked over while the laser is on, the LCOS will be instantly destroyed. Given the high cost of the LCOS this is clearly not desirable in machine used for prototyping. From this practical point of view, it is worth making sure that only $f_1 \approx b$. There are no similar concerns for making $f_1 = a$.

Examining the matrix $M_{\text{lensarray}}$, it can be noted that if $f_1 = a$ then the matrix simplifies considerably to:

$$\begin{pmatrix} \frac{f_1 \cdot s}{-f_{\text{lenslet}}} \\ r \\ \frac{f_1}{f_1} \end{pmatrix} + r \begin{pmatrix} 1 - \frac{b}{f_1} \\ 0 \end{pmatrix} = \begin{pmatrix} r_{\text{LCOS}} \\ \theta_{\text{LCOS}} \end{pmatrix} \quad (3.17)$$

Where the matrix has been split into the main unperturbed component and its perturbation for $f_1 \neq b$, for ease of reading. We can confirm that the perturbation approaches zero as f_1 approaches b .

Since f_1 is a positive quantity and f_{lenslet} is a negative quantity, the magnification of the beam is positive so the image is right side up.

Each lenslet has an identical clear height – the height of the lenslet. Consider the top-most and bottom-most ray for a given lenslet of height h_{lenslet} . The size of final illumination on the LCOS will be defined by these two rays and thus has a height of:

$$\begin{aligned} & \left(\frac{f_1 \cdot h_{\text{lenslet}}/2}{-f_{\text{lenslet}}} + (r + h_{\text{lenslet}}/2) \left(1 - \frac{b}{f_1} \right) \right) - \\ & \left(\frac{f_1 \cdot (-h_{\text{lenslet}}/2)}{-f_{\text{lenslet}}} + (r - h_{\text{lenslet}}/2) \left(1 - \frac{b}{f_1} \right) \right) \\ & = \frac{f_1 \cdot h_{\text{lenslet}}}{-f_{\text{lenslet}}} + h_{\text{lenslet}} \left(1 - \frac{b}{f_1} \right) \end{aligned} \quad (3.18)$$

Since the lenslets are rectangular with the same aspect ratio as the LCOS, then

3.3. ANALYSIS OF LENS SYSTEM

the width of the illumination beam on the LCOS will have the correct width if the height is correct.

Considering the perturbation part of the matrix, it can be seen that the rectangular image produced by each lenslet will not exactly overlap. The size of the beam produced by each lenslet will be identical, but the lateral position of each illumination rectangle will be different for each lenslet. The difference between the lowest top-most ray and the highest bottom-most ray can be used to find the height of the area that will be illuminated by all of the lenslets.

If the beam illuminating the microlens array has a height y (equal to the height of the aperture), then the illumination height $H_{\text{lc}}_{\text{os}}$ is:

$$H_{\text{lc}}_{\text{os}} = \frac{f_1 \cdot h_{\text{lenslet}}}{-f_{\text{lenslet}}} - y \left(1 - \frac{b}{f_1} \right) \quad (3.19)$$

The previously mentioned matrix $M_{\text{lensarray}}$ describes the required lens properties for a chosen microlens array can be calculated (i.e. calculate the focal length such that the beam correctly illuminates the LCOS). The required lens is placed at the optical distance approximately equal to the lens' focal length. The LCOS should be protected with a covering (or removed) when first testing the inserted lens, to avoid destroying the LCOS.

The initial beam is of the order of a centimeter and the focal length f_1 of the lens L1 is of the order of 30 cm, so $r \ll f_1$ so $\theta_{\text{LCOS}} \approx 0$. This is important because the beam clear height is determined by the clear height of the intermediate mirror and cube beam-splitter. This puts a restriction on initial beam size, since the larger the initial beam size, the larger the beam divergence.

The magnification of the aperture at the holopixel plane was determined in Equation (3.11) on page 39. This was based on a total effective focal length, f_{eff} of 7.669 mm. For a holopixel size of between 1.0 mm to 0.3 mm and utilizing at least 10.0 mm of the microlens array up to a maximum of 30.0 mm, the magnification

3.3. ANALYSIS OF LENS SYSTEM

factor should be between 10 to 100. Given that the distance b , and thus the focal length f_1 , is restricted to approximately 150 mm, and using the said magnification formula, we obtain:

$$150 \text{ mm} \leq f_1 < 100 \times f_{\text{eff}} \quad (3.20)$$

$$150 \text{ mm} \leq f_1 < 30 \times 7.669 \text{ mm} \quad \text{For holopixel of size 1.0 mm} \quad (3.21)$$

$$150 \text{ mm} \leq f_1 < 230 \text{ mm} \quad \text{For holopixel of size 1.0 mm} \quad (3.22)$$

$$33 \times 7.669 \text{ mm} \leq f_1 < 100 \times 7.669 \text{ mm} \quad \text{For holopixel of size 0.3 mm} \quad (3.23)$$

$$256 \text{ mm} \leq f_1 < 767 \text{ mm} \quad \text{For holopixel of size 0.3 mm} \quad (3.24)$$

Rearranging the unperturbed part of Equation (3.19) on the preceding page:

$$f_1 = -H_{\text{icos}} \times \frac{f_{\text{lenslet}}}{h_{\text{lenslet}}} \quad (3.25)$$

3.3.6 Summary

Choose the required holopixel radius, r . Typically $1.0 \text{ mm} \geq 2r \geq 0.3 \text{ mm}$.

For a given microlens array with lenslets with a height of h_{lenslet} and a focal length of f_{lenslet} , determine the required focal length of lens L1, f_1 .

$$f_1 = -H_{\text{Icos}} \times \frac{f_{\text{lenslet}}}{h_{\text{lenslet}}} \quad (3.26)$$

Ensure that the chosen microlens array sets f_1 within the range:

$$150 \text{ mm} \leq f_1 < 230 \text{ mm} \quad \text{For holopixel of size 1.0 mm} \quad (3.27)$$

$$256 \text{ mm} \leq f_1 < 767 \text{ mm} \quad \text{For holopixel of size 0.3 mm} \quad (3.28)$$

Place the lens L1 at a distance $b \approx f_1$, such that b is a few millimeters different from f_1 , to slightly defocus the holopixel image. Place the microlens array at a distance a from the lens L1 such the $a = f_1$.

Use a square or circular aperture with a height y , placed against the microlens array, where y is:

$$y = 2r \cdot \frac{f_1}{f_{\text{eff}}} \quad (3.29)$$

3.3.7 Example microlens array

The necessary formulas for determining the properties of the microlens array and lenses were established in the previous section. The distance b (From L1 to the LCOS, illustrated in Figure 3.5 on page 28) is restricted by the requirement that the clear height of the diverging beam is set by the clear height of the intervening beam splitter and mirror. The distance is further restricted by the physical minimum spacing between the LCOS, beam splitter and mirror. This restricts the minimum distance of b to approximately 150 mm (Figure 3.3 on page 24).

The display used in this printer is a reflective LCOS display made by the company Brillian. The model is the BR1080HC, and the dimensions are shown in Figure 3.12 on the next page. The LCOS is used in landscape format.

This Brillian LCOS has a display screen height of 10.56 mm (See Figure 3.12 on the following page), requiring that the illuminating beam has a height equal to this to ensure full illumination without unnecessary loss of energy. With this requirement, $H_{\text{lcOS}} = 10.56 \text{ mm}$.

Applying the determined values to the unperturbed term in Equation (3.19) on page 45, the desired ratio of lenslet height h_{lenslet} to lenslet focal length f_{lenslet} is obtained:

$$\frac{h_{\text{lenslet}}}{-f_{\text{lenslet}}} \leq \frac{10.56 \text{ mm}}{150 \text{ mm}} \quad (3.30)$$

$$\implies \frac{h_{\text{lenslet}}}{-f_{\text{lenslet}}} \leq 0.07 \quad (3.31)$$

Consider an LCOS with lenslets with a clear height of $h_{\text{lenslet}} = 0.2 \text{ mm}$ and a focal length of $f_{\text{lenslet}} = -3.0 \text{ mm}$. This satisfies the condition since $0.2 \text{ mm} \div 3.0 \text{ mm} = 0.67$.

3.3. ANALYSIS OF LENS SYSTEM

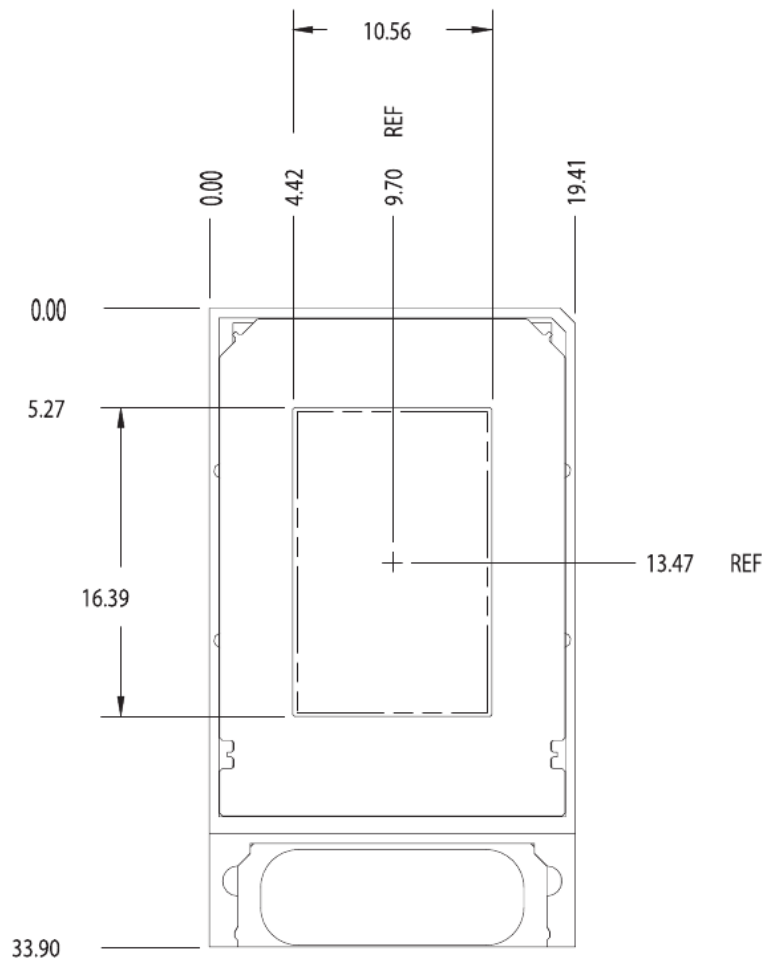


Figure 3.12: Dimensional schematic of the Brillian LCOS Display BR1080HC

http://www.brilliantcorp.com/PDF/projection/BR1080HC_BR_D4.pdf

	First	Second	Third
Lenslet dimensions:	0.40×0.46 mm	0.20×0.23 mm	0.040×0.046 mm
Spherical radius:	1.3 mm	0.65 mm	0.13 mm
Required magnification:	26.4	52.8	264.0
Focal length f_{lenslet} :	-0.4 mm	-0.8 mm	-4.0 mm
Required f_1 :	10.56 mm	42.24 mm	324.92 mm
Aperture size ($r=1.0$ mm):	1.38 mm	5.51 mm	42.37 mm
Aperture size ($r=0.3$ mm):	0.41 mm	1.65 mm	12.71 mm

Table 3.1: Microlens array properties

3.3. ANALYSIS OF LENS SYSTEM

From Equation (3.26) on page 47:

$$f_1 = -H_{\text{lc}} \times \frac{f_{\text{lenslet}}}{h_{\text{lenslet}}} \quad (3.32)$$

$$= 10.56 \text{ mm} \times \frac{3.0 \text{ mm}}{0.2 \text{ mm}} \quad (3.33)$$

$$= 158 \text{ mm} \quad (3.34)$$

For a 1.0 mm pixel the aperture has a height y , from Equation (3.29) on page 47, of:

$$y = 2r \cdot \frac{f_1}{f_{\text{eff}}} \quad (3.35)$$

$$= 1.0 \text{ mm} \cdot \frac{158 \text{ mm}}{7.669 \text{ mm}} \quad (3.36)$$

$$= 20.7 \text{ mm} \quad (3.37)$$

To obtain a circular holopixel that is 1.0 mm in diameter, the aperture needs to also be circular with a diameter y of 20.7 mm. This would utilize approximately $\frac{20.7^2}{0.2^2} = 10712$ lenslets - sufficient to provide smooth illumination.

Three different microlens arrays that satisfy the condition in Equation (3.31) on page 48 are experimentally tested in the next section for a qualitative analysis. The three microlens arrays examined are all composed of an array of rectangular lenslets with a dimensional ratio equal to that of the LCOS. The relevant details along with the required focal length of lens L1 and required aperture height calculated by the methods given here, are given in Table 3.1 on the previous page.

3.4 Experimental evaluation of lens array system

In analogue holography a hologram is made by illuminating a physical object with coherent light. The microscopic roughness of the surface of the object creates speckle which can present a serious visual problem. The final hologram can appear to 'twinkle' or 'sparkle' and the effective resolution of the hologram is several times lower than the diffraction limit [51].

In digital holography using a computer display, the problem of speckle is almost removed. A dot matrix of 'holopixels' is printed, each with their own independent speckle. On replay with a white-light source, the human eye does not observe any sparkling effects. Speckle does pose other problems however. The speckle affects the angular distribution of intensity for each holopixel, as described below.

There is an additional possible problem – speckle on image at the Fourier plane may also affect the diffraction efficiency as the light intensity is not evenly distributed across emulsion, thus not fully utilizing all of the grains.

Section 3.3.5 on page 40 analytically considered the microlens array system to determine the optimal distance based upon the lenslet size, aperture size, pixel size, and distances. However this approach does not take into account the effect of speckle. The microlens array acts as an array of mutually coherent point light-sources. These point sources expand and overlap, each illuminating the microlens array, creating an averaged illumination that hides any defects in the beam quality (due to dust particles etc). An unwanted side-effect however is that the mutually coherent sources interfere with each other creating speckle.

The speckle pattern created on the LCOS results in an effectively reduced resolution of the LCOS display system, reducing the possible depth of field of the hologram (both into the hologram plane, and out of the hologram plane). A severe degree of speckle can result in holograms with low fidelity and contrast.

To reduce the effect of speckle, a simple method was required that introduced

3.4. EXPERIMENTAL EVALUATION OF LENS ARRAY SYSTEM

minimal complexity and cost into the design. A brief summary of existing methods is presented below, with its applicability to digital holography noted. As the speckle is affected by the properties of the microlens array and the optics between the microlens array and the LCOS, the simplest method was to try different microlens arrays and different positions to qualitatively minimize the effect of speckle.

The structure of the speckle is examined, followed by a subjective assessment of the overall image quality. The results are summarized, and the microlens array with the larger lenslets (rectangular lenslets of dimensions $0.40\text{ mm} \times 0.46\text{ mm}$ with a curvature of radius of 1.3 mm) was chosen for future digital holography research.

The raw recorded data is presented in Appendix I.

3.4.1 Previous work

The problem of speckle due to a coherent source on a microlens array has been tackled many times. Goodman [52] showed over 30 years ago that speckle can be regarded as arising from a classical random walk in the complex plane. Reducing the contrast or smoothing the speckle requires diversity in the polarization, space, frequency or time. In the proceeding years, each of these avenues were investigated with varying success for use in many different fields in science. Iwai and Asakura [53] summarize the 30 years of research into each of these different avenues. The applicability of these approaches to digital holography is very briefly given here.

For pulsed holography, time varying the polarization in a pulse would destroy the diffraction gratings on the hologram. Compositing both horizontal and vertical polarizations on to a single pixel may possibly work, although it would present practical difficulties.

Increasing spatial diversity has been used with moderate success in analogue

3.4. EXPERIMENTAL EVALUATION OF LENS ARRAY SYSTEM

holography [54]. This approach could be taken with digital holography by using a spatial mask in front of the microlens array. This would however result in blocking off a significant portion of the beam, reducing the energy efficiency of the holographic printer.

An alternative to introducing spatial diversity without masking the beam is to introduce random or pseudo-random phase shifts. For holography, a common approach is to use a spatial phase mask with a pseudorandom sequence of phase shifts. By keeping some degree of regularity in the phase shifts, speckle can be significantly reduced, while the slight pseudo-randomness removes the noise as intended [55, 56].

Varying the frequency or compounding multiple frequencies has been applied successfully in many other fields of science (Trahey et al. [57] for example). It is not clear however how such an approach could be employed by holography. Recording a hologram with a compound of two (or more) very similar frequencies would result in low diffraction efficiency as the diffracting gratings interfere with one another. Time varying the frequency would also destroy the diffraction gratings required, aside from the practical complications.

Time varying the beam is a common approach to speckle. Often the image is time averaged to visually remove speckle, such as employing the use of a rotating diffuser in the imaging plane of the microlens array[58], or vibrating an optical fibre[59, 60, 61] to produce a time-varying phase-shift[62]. This type of approach is however not particularly suitable for pulsed holography where the beam pulse is on the order of tens of nanoseconds. More complicated approaches have been used such as splitting the speckled beam into several parts and using a delay line to temporally delay each of the beams differently. Recombining the beam averages the speckle, effectively removing it without loss of resolution [63]. This introduces significant complexity into the design, and it is not clear if this type of approach would work for holography.

3.4.2 Experimental setup

The following microlens arrays were considered³:

1. Table I.1 on page 177 examines the first microlens array with each lenslet being rectangular with physical dimensions of $0.40\text{ mm} \times 0.46\text{ mm}$. These lenslets are spherical lenses with a radius of 1.3 mm.
2. Table I.2 on page 179 examines the second microlens array with each lenslet being rectangular with physical dimensions of $0.20\text{ mm} \times 0.23\text{ mm}$. These lenslets are spherical lenses with a radius of 0.65 mm.
3. Table I.3 on page 181 examines the third microlens array with each lenslet being rectangular with physical dimensions of $0.040\text{ mm} \times 0.046\text{ mm}$. These lenslets are spherical lenses with a radius of 0.13 mm.

To test the three microlens array arrays, the lens system was setup as previously described in Section 3.3 on page 30. Each of the three different microlens array arrays were tried at different positions. The pulsed laser was switched producing a projected image from the final objective lens. When printing, the photosensitive hologram plate would be placed a few millimeters away from the objective lens, in the Fourier plane of the image of the LCOS display system. This experiment instead removed any hologram plate, and projected the image of the LCOS on to a white board 1.2 m from the lens objective.

The contrast and intensity of the speckle relative to the displayed image was determined by the properties of microlens array array as well as its position. The overall 'noise' (intensity strength relative to the displayed image) of the speckle was recorded, along with the size and shape of the beam profile where it illuminates the LCOS display system.

The speckle in the projected image also contained a repeating pattern. The size of these repeating patterns was measured by measuring the size of a multiple

³A style note: For those with a colour version of this report, the data for the first microlens array is always plotted and referenced in a blue color, the second microlens array uses purple/red, and the third microlens array uses green. This is purely a visual aid to the reader.

3.4. EXPERIMENTAL EVALUATION OF LENS ARRAY SYSTEM

number of these repeating structures with a ruler.

Appendix I gives the raw recorded data for the three different microlens array arrays at different positions.

As an important experimental note: If the microlens array array focal point is imaged directly onto the LCOS, the energy density on the LCOS can be sufficiently high to risk breaking the LCOS. This was avoided and noted in the tables were applicable.

3.4.3 Image quality

Figure 3.13 on the next page graphs the quality of the projected image of the LCOS display based upon a subjective judgment of the quality of the image. A large range of positions was tested, however the range is limited by the Equation (3.5) on page 38; the microlens array is required to be positioned at approximately the distance of the focal length of the lens that images it onto the LCOS display. Figure 3.14 on page 57, Figure 3.15 on page 58 and Figure 3.16 on page 58 judge a suitable range for the LCOS based upon intensity distribution across the LCOS (A smooth, even distribution is required, as opposed to a Gaussian distribution if the lens array is too close) and the shape of the beam (The whole of the LCOS should be illuminated with little energy wasted).

3.4. EXPERIMENTAL EVALUATION OF LENS ARRAY SYSTEM

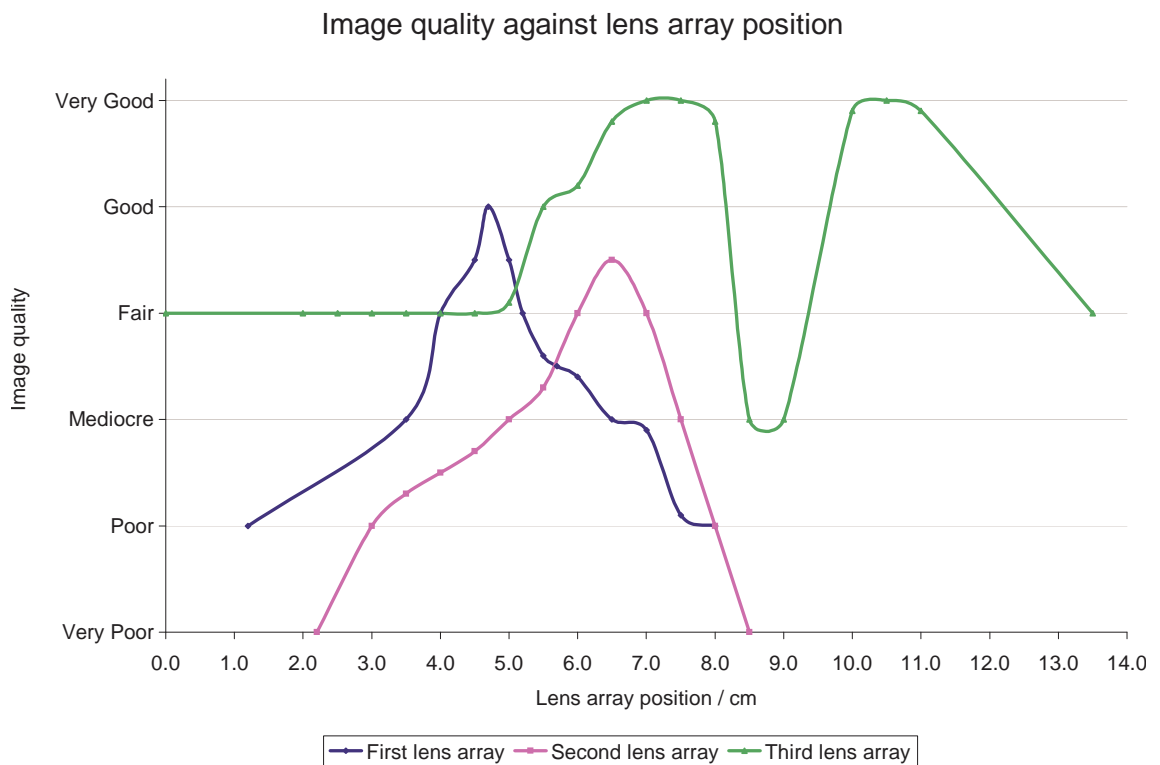


Figure 3.13: The subjectively judged quality of the projected image of the LCOS on a white board 1.2 m away from the objective lens, due to speckle noise. An image judged as Very Good would have a nearly unnoticeable amount of visual speckle. The data is drawn from the recorded data in Appendix I.

3.4. EXPERIMENTAL EVALUATION OF LENS ARRAY SYSTEM

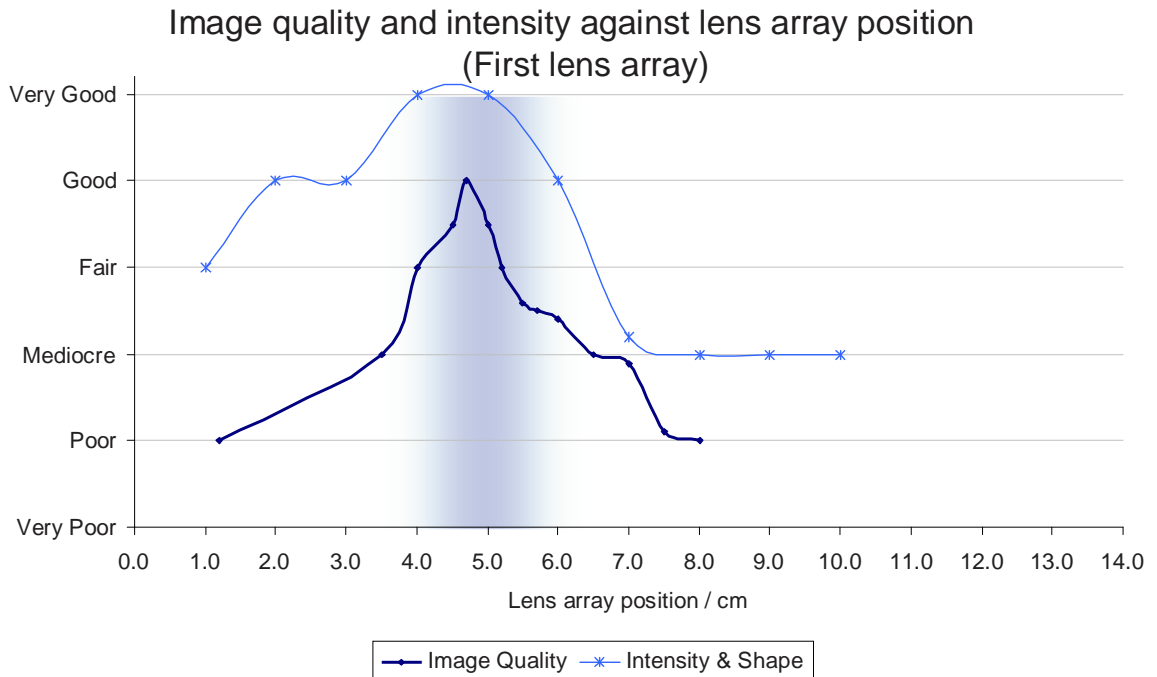


Figure 3.14: The size and shape of the beam must be sufficiently close to the size and shape of the LCOS. Additionally the illumination intensity across the LCOS must be spatially smooth and even. These two factors were considered together, using the recorded data in Appendix I, and drawn here as the 'Intensity & Shape' curve. This is drawn with the Image Quality curve shown in Figure 3.13 for comparison. This graph is shown for the first microlens array. A suitable region for the distance between the microlens array and closest lens such that the image quality, beam intensity and beam shape are all at least acceptable is between approximately 4.0 cm to 6.0 cm.

3.4. EXPERIMENTAL EVALUATION OF LENS ARRAY SYSTEM



Figure 3.15: This graph is similar to Figure 3.14 on the previous page and shown for the second microlens array. A suitable region for the distance between the microlens array and closest lens such that the image quality, beam intensity and beam shape are all at least acceptable is between approximately 5.5 cm to 7.5 cm.

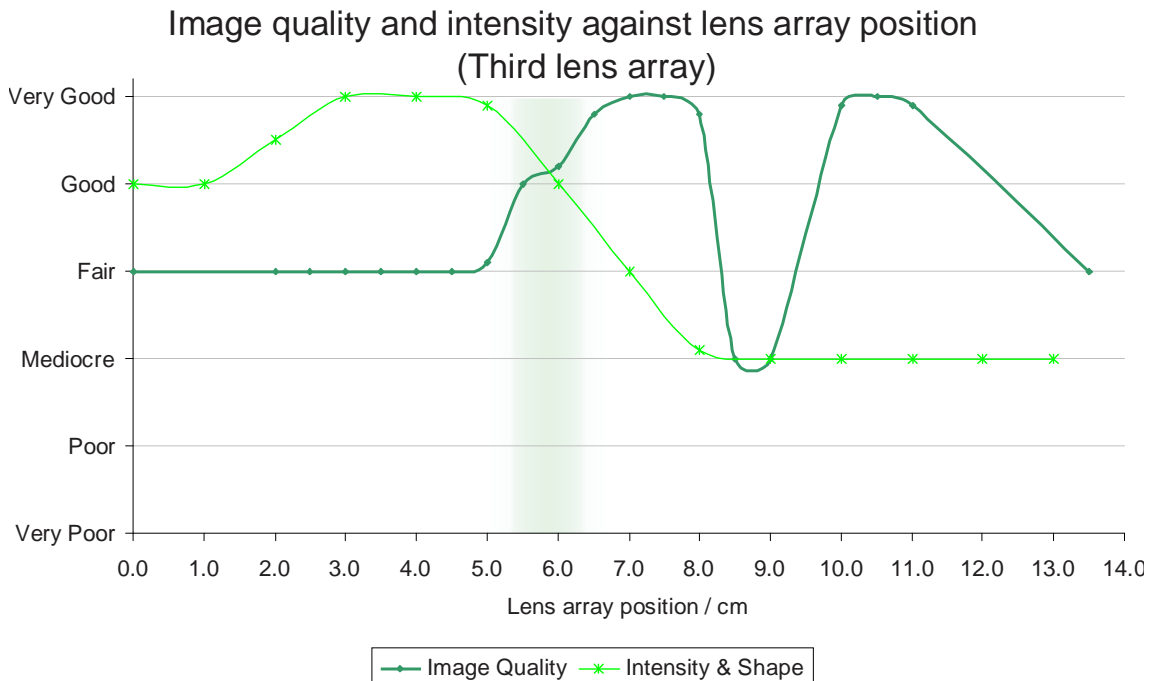


Figure 3.16: This graph is similar to Figure 3.14 on the previous page and shown for the third microlens array. A suitable region for the distance between the microlens array and closest lens such that the image quality, beam intensity and beam shape are all at least acceptable is between approximately 5.5 cm to 6.5 cm.

3.4. EXPERIMENTAL EVALUATION OF LENS ARRAY SYSTEM

3.4.4 Speckle repeating structure size

If the lenslets' focal points are imaged directly onto the LCOS, the energy density on the LCOS can be sufficiently high to risk breaking the LCOS. This was avoided and noted in the tables were applicable.

Table 3.2 summarizes the speckle data that is presented in Appendix I; noting that the uncertainty error was ± 0.5 cm for the measurement of the total size of the sample of repeating structures.

Dist. A	First			Second			Third		
	No.	Total Dist	Distance	No.	Total Dist	Distance	No.	Total Dist	Distance
0.0							6.0	21.5	3.58 ± 0.08
1.2	1.0	1.5	1.5 ± 0.5						
2.0							6.0	19.7	3.28 ± 0.08
2.2				7.0	25.5	3.64 ± 0.07			
2.5							7.0	23.6	3.37 ± 0.07
3.0				4.0	11.5	2.88 ± 0.13	8.0	25.2	3.15 ± 0.06
3.5	10.0	14.8	1.48 ± 0.05	4.0	10.0	2.50 ± 0.13	5.0	11.4	2.28 ± 0.10
4.0	10.0	12.5	1.25 ± 0.05	5.0	10.0	2.00 ± 0.10	8.0	18.7	2.34 ± 0.06
4.5	10.0	12.4	1.24 ± 0.05	10.0	22.0	2.20 ± 0.05	8.0	17.9	2.24 ± 0.06
4.7	10.0	11.1	1.11 ± 0.05						
5.0	10.0	11.5	1.15 ± 0.05	10.0	22.0	2.20 ± 0.05	10.0	22.0	2.20 ± 0.05
5.2	10.0	10.5	1.05 ± 0.05	10.0	21.0	2.10 ± 0.05			
5.5	10.0	10.0	1.00 ± 0.05	10.0	19.0	1.90 ± 0.05	8.0	15.4	1.93 ± 0.06
5.7	10.0	10.0	1.00 ± 0.05						
6.0	10.0	9.0	0.90 ± 0.05	10.0	17.0	1.70 ± 0.05	5.0	7.8	1.56 ± 0.10
6.5	10.0	7.8	0.78 ± 0.05	10.0	15.5	1.55 ± 0.05	6.0	9.3	1.55 ± 0.08
7.0	10.0	4.3	0.43 ± 0.05	10.0	11.2	1.12 ± 0.05	10.0	12.3	1.23 ± 0.05
7.5	30.0	14.5	0.48 ± 0.02	10.0	9.2	0.92 ± 0.05	8.0	8.7	1.09 ± 0.06
8.0	10.0	3.0	0.30 ± 0.05	30.0	19.0	0.63 ± 0.02	10.0	7.1	0.71 ± 0.05
8.5							10.0	5.0	0.50 ± 0.05
9.0							10.0	2.9	0.29 ± 0.05

Table 3.2: Size of repeating speckle structure. Total distance uncertainty is ± 0.5 cm. All values given in cm. Dist. A is the distance between the microlens array array and the closest lens with an uncertainty of 0.1 cm. 'No.' is the number of repeating structures measured for the purpose of reducing uncertainty.

This data is plotted in Figure 3.17 on the next page.

3.4. EXPERIMENTAL EVALUATION OF LENS ARRAY SYSTEM

Speckle pattern size against lens array position



Figure 3.17: Repeating speckle structure size plotting against position of microlens array for each of the three different microlens arrays.

The size of the speckle patterns is smallest for the first microlens array, which is the microlens array with the largest lenslets and with the largest radius of curvature. It is not entirely clear how much effect this structure will have on the final hologram.

3.4. EXPERIMENTAL EVALUATION OF LENS ARRAY SYSTEM

3.4.5 Microlens array focal plane

There is another concern regarding the position of the microlens array. The plane of the aperture that is imaged on to the photosensitive emulsion is very close to the microlens array. As the lenslets have a small focal distance, the aperture is also very close to the virtual image of the focal plane of the microlens array. It is my concern that if the imaged focal plane of the microlens array coincides with the plane of the photosensitive emulsion, this will result in an uneven illumination of the film, significantly reducing diffraction efficiency.

To monitor this effect, the data in Appendix I records the relative distance of the lenslet focal plane from the hologram plate. This distance could not be measured directly, so to measure this a piece of white card was placed inside the afocal telescopic lens system and moved into position such that the focal point of the microlens array was focused onto the card. This could be seen clearly as an array of points of light. The distance between this position and the image plane of the aperture was recorded. All the distances given below are in terms of the distance measured between the imaged focal plane of the microlens array and the corresponding imaged plane of the aperture in telescopic lens system. The position of the aperture remained unmoved and the only variable changed was the position of the microlens array. It is worth noting that moving the microlens array will in turn slightly move the plane that the aperture is focused on near the hologram plane.

Extracting this distance data from the tables for the first, second and third microlens arrays we get Table 3.3 on the following page.

3.4. EXPERIMENTAL EVALUATION OF LENS ARRAY SYSTEM

Micro lens array dist. (cm)	First (cm)	Second (cm)	Third (cm)
0.0			12.5
1.2	8.0		
2.0			10.0
2.2		10.5	
2.5			9.5
3.0		8.0	8.5
3.5	5.5	8.0	8.0
4.0	4.2	7.4	7.5
4.5	4.0	6.4	5.5
4.7	2.1		
5.0	1.5	5.0	2.1
5.2	0.0		
5.5	-0.8	2.0	0.2
5.7	-1.7		
6.0	-4.0	0.0	-1.8
6.5	-6.8	-3.5	-5.0
7.0	-19.0	-10.0	-9.8
7.5		-17.0	-15.0
8.0			-17.0

Table 3.3: Distance measured between the imaged focal plane of the microlens array and the corresponding imaged plane of the aperture in telescopic lens system. All values given with uncertainty of ± 0.5 cm.

3.4. EXPERIMENTAL EVALUATION OF LENS ARRAY SYSTEM

Figure 3.18 graphs the results given in Table 3.3 on the preceding page with a smoothed connecting line for visual clarity.

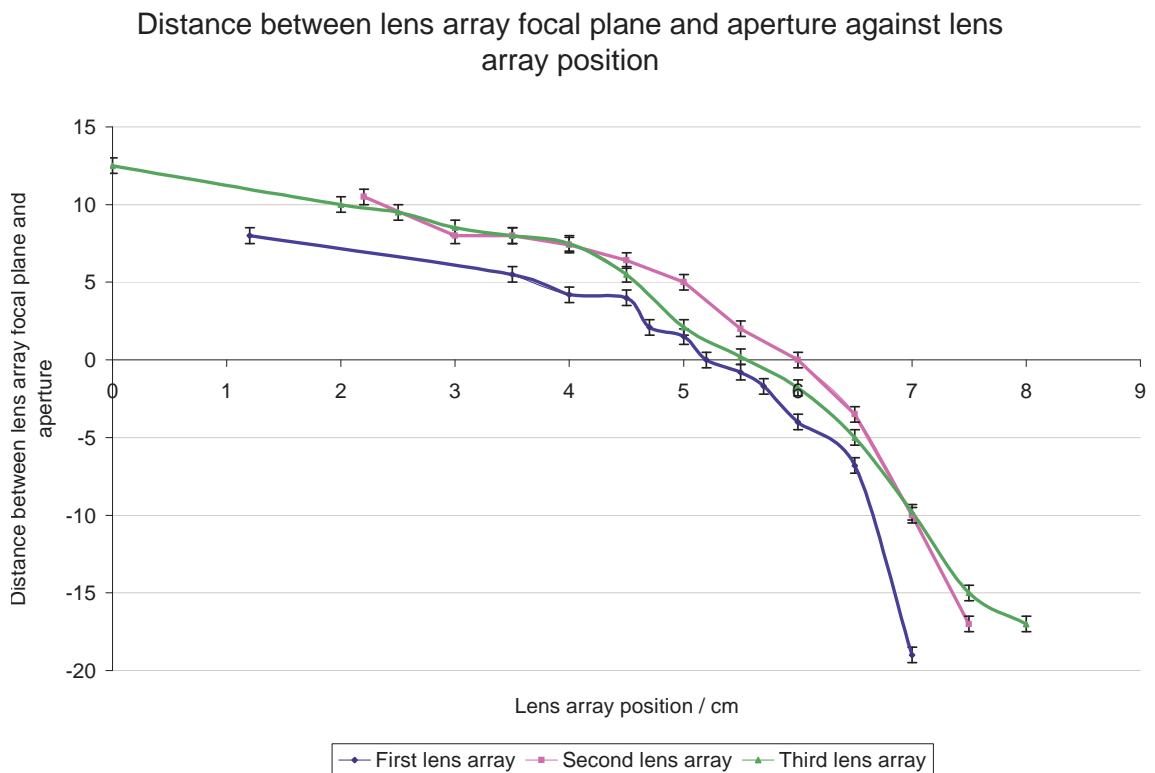


Figure 3.18: Graph of distance measured between the imaged focal plane of the microlens array and the corresponding imaged plane of the aperture in telescopic lens system. All values shown with error bar of ± 0.5 cm.

3.4.6 Summary

The first microlens array had rectangular lenslets with physical dimensions of $0.40\text{ mm} \times 0.46\text{ mm}$ and spherical curvature of radius of 1.3 mm . The best position based upon image quality, beam intensity and shape was at approximately 4.8 cm from the lens. This microlens array exhibited the smallest repeating structure size of 1.2 cm and in this position the focal plane of the lenslets is at small distance away from the plane of the aperture.

The second microlens array had rectangular lenslets with physical dimensions of $0.20\text{ mm} \times 0.23\text{ mm}$ and spherical curvature of radius of 0.23 mm . The best position based upon image quality, beam intensity and shape was at approximately

3.4. EXPERIMENTAL EVALUATION OF LENS ARRAY SYSTEM

6.7 cm from the lens. At this position, the repeating structure size is approximately 1.4 cm, and the focal plane of the lenslets is at a distance away from the plane of the aperture.

The third microlens array had rectangular lenslets with physical dimensions of 0.040 mm×0.046 mm and spherical curvature of radius of 0.13 mm. The best position based upon image quality, beam intensity and shape was at approximately 6.0 cm from the lens. At this position, the repeating structure size is the largest of the three lens arrays at approximately 1.6 cm. The focal plane of the lenslets is close to the plane of the aperture.

There does not appear to be any significant differences between using the three microlens arrays. They each exhibited quite different behavior, but when all of the factors are taken into account, there is no clear superior choice.

For future work, the first microlens array was chosen due to the smaller repeating speckle structure.

3.5 Minimizing beam energy loss in lens system

The Red Green Blue (RGB) digital hologram printer design by Ratcliffe et al. [47] utilizes a long cavity Nd:YAG laser to provide sufficient energy to illuminate the silver halide emulsion. The energy required from the laser, per color channel, is dependant upon the size of the printed holopixel, the efficiency of the hologram printer (lens system, display system) and the sensitivity of the photo-sensitive emulsion to the illumination wavelength and pulse length used.

For the printing of monochromatic green holograms, a green-sensitive monochromatic fine-grain emulsion such as VRP-M (Zacharovas et al. [see 64]) from Slavich [65] is sufficient. This particular emulsion is sensitive to pulse lengths from nanosecond pulses up to CW laser emission. For pulsed radiation with a length of around tens of nanoseconds, the VRP-M emulsion requires an energy density of approximately 60 J/cm^2 for maximum diffraction efficiency⁴.

For the production of true color volume holograms, a panchromatic or dichromatic gelatine emulsion is required, such as the ultra-fine grain emulsion known as PFG-03C [64] from Slavich [65]⁵. The fine size of the grains makes the emulsion less sensitive to radiation, requiring an energy density approximately 3.0 mJ/cm^2 of green-light pulsed radiation⁶ for maximum diffraction efficiency. Some characteristics of the Slavich color emulsion have been presented by Markov [66], with a further more theoretical analysis on selective characteristics of single layer color holograms by Markov and Khizhnyak [67]. An overview of the current state of colour reflection holography is given by Bjelkhagen et al. [68].

Ratcliffe et al. [47] proposes the use of a long cavity Nd:YAG pulsed laser, produced by Geola Technologies, which has a repetition rate of up to ten pulses per second and can provide ample energy for such a system (Typically around

⁴<http://www.geola.com/45.asp>

⁵A photographic company outside Moscow. See References.

⁶<http://www.geola.com/48.asp>

3.5. MINIMIZING BEAM ENERGY LOSS IN LENS SYSTEM

15 mJ for the second harmonic). In this context, the energy efficiency of the system is not of high importance.

There are however many advantages to minimizing energy loss. Increasing the laser repetition rate is technologically simpler if the energy in each shot is decreased. Likewise if a short cavity laser is utilized instead of a long cavity laser, a more stable output is achieved at the sacrifice of shot energy. The use of a short cavity laser also offers a simpler design, making the system cheaper due to less components required and a shorter build and maintenance period of time.

The biggest loss of energy in the system by Ratcliffe et al. [47] is in the LCD display system. The system detailed in the section utilizes an LCOS system to increase the efficiency by approximately 30 percentile points, and a series of magnifying relay lenses to minimize energy loss at the apertures.

An extra system of magnifying relay lenses can be used to reduce the energy loss on the apertures on both the reference and object beams by reducing the beam size to the size of the apertures. Such a system of magnifying relay lenses is also useful to control the size of the object beam at the plane of the microlens array. The spatial profile of the beam at the microlens array is geometrically similar to the spatial profile of the beam on the hologram plate. To clean the reference beam, a small aperture was placed at the mutual focal point of the magnifying relay lenses and adjusted with the aid of a laser beam spatial profiler placed upstream.

3.6 Summary

A digital hologram printer was developed and built based upon the design by Ratcliffe et al. [47]. The steps required reproduce the creation of a hologram printer are given, mixed in with lessons learned from the accumulated experience of building and maintaining three such printers. A new display system (LCOS display) was investigated and found to have a significant advantage over the LCD display system used by Ratcliffe et al. [47]. The lens systems were analytically examined by various approximations and methods to determine a simple set of formulas to allow the holopixel spatial size to be easily adjusted by the hologram printer operator.

Three microlens arrays were qualitatively analyzed by a series of experiments and they were found to perform almost equally well, demonstrating that the properties of the microlens array do not have a significant effect on the hologram quality, within the parameter space tested.

A brief mention on increasing the energy efficiency of the design was made, with the goal of replacing the long cavity laser with a short cavity laser. A short cavity laser would have the advantage of increasing the laser energy point-to-point stability while also lowering the overall cost. Minimizing energy loss is discussed further in Chapter 5.

Figure 3.19 on the next page demonstrates the working hologram printer.



Figure 3.19: Photograph of green dragon hologram with $1\text{ mm}\times 1\text{ mm}$ pixels printed on the described hologram printer. Note that there are occasional incorrectly-dim pixels due to the laser energy instabilities. This is discussed and fixed in Chapter 6 on page 113.

4

White logo

This chapter looks at a common problem with printing digital holograms that have a large contrast range. A specific hologram is studied to study this problematic 'ghosting' effect and the cause is identified. A set of Matlab programs are written to test possible solutions and their effectiveness is determined.

4.1 Overview

Figure 4.2a on page 74 is a photograph of a white-light-viewable full-color hologram that was printed on a RGB hologram printer that is similar in design to that described in this thesis. In particular, the same Brillian LCOS display system was utilized, along with the same lens systems. The photograph was taken at an angle normal to the hologram. The intended result was to produce a hologram that looks similar to the rendered image for that angle, as shown in Figure 4.2c on page 74.

4.1. OVERVIEW

As can be seen in the photograph, the hologram has the highest intensity between the letters. This visually appears as a 'ghosting' or a 'shadow' effect. This effect is due to an unintended side effect that is due to the decrease in the effective viewing angle of that holopixel, and thus a decrease in the viewing window. Figure 4.1 on the following page illustrates the problem; the LCOS display system spatially modulates the object beam with the angular intensity distribution required for a particular holopixel. This spatially-modulated beam is optically Fourier transformed and arranged to interfere with the reference beam. The resulting signal is recorded onto the hologram plate. After chemical development and bleaching, upon illumination of the hologram, the angular intensity distribution for that holopixel is replayed.

If the original image on the display system looks similar to that as shown on the left-hand side of Figure 4.1 then the range of viewing angles in which the pixel appears illuminated is large. If the original image on the display system is significantly smaller than the display, as shown in the right-hand side of Figure 4.1, then upon replay a smaller range of viewing angles in which the pixel appears illuminated is obtained.

The problem, however, is that the large viewing window results in the total energy being spread over a large area. Thus the intensity of the light in any particular direction is less than it would be for a small viewing window. So if the two holopixels indicated in Figure 4.1 were printed, the viewer would observe the holopixel indicated on the left-hand side as being brighter than the holopixel indicated on the right-hand side, despite that the corresponding pixel on the display system in both cases has the same angle.

To correct for this problem, the intensity of each pixel on the LCOS must be adjusted as a function of the entire image on the LCOS. Artists also need to be aware of the limitations - pixels that will illuminate in all directions appear as bright as pixels that only illuminate in very specific directions.

A mathematical analysis of this problem would be presumably be possible

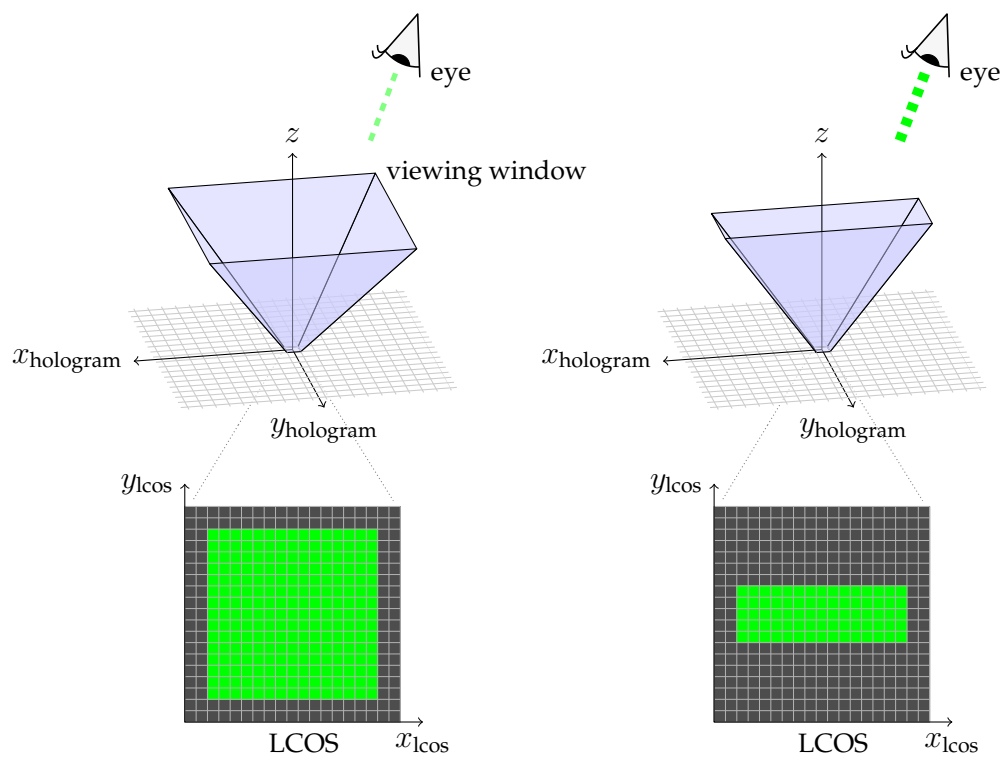


Figure 4.1: The Fourier transform of the image on the LCOS is printed on to the hologram as a single 'holopixel'. Upon replay of the hologram, this recorded Fourier image is reconstructed as an angular intensity distribution. If the viewing window is smaller, as shown on the right, then the overall intensity as seen by the eye will be larger.

based on considering the continuous wavelet Fourier transform and subsequent interference of the LCOS image to the recorded holopixel (Such as the wavelet Fresnel techniques by Liebling [69]). The non-linear properties of the photosensitive film would ideally be then taken into account. The determined white-light reflection holograms can then be analyzed with the same wavelet techniques to reconstruct the final image (For example, the work by Sandoz [70], Recknagel and Notni [71] and the statistical approach by Sotthivirat and Fessler [72]). However such an approach would be both tricky and computationally demanding. Correct sampling, for an example of the trickiness involved, is a key issue in such reconstruction algorithms, with extensive research (For example see [73, 74, 75]). To avoid such complications, an experimental approach was taken instead.

To research and solve the problem experimentally, three distinct steps were required.

The first step was to compare the photograph of the White Logo hologram against the rendered images. This is done in Section 4.2 on the next page.

The second step was to precisely determine the relative diffraction efficiency of the pixels of the hologram in a consistent and accurate way. This required the building of a framework to hold the hologram, a spectrometer, and a halogen lamp, and is explained further in Section 4.3 on page 80.

Thirdly, a mathematical approach to the physical system is required to determine an algorithm to correct the intensity of the pixels shown on the LCOS. This is discussed in Section 4.4 on page 85.

4.2 Photograph analysis

To better understand the problem, the photograph of the White Logo hologram (Figure 4.2a on the following page) was analyzed against the series of rendered images that were used to create the said hologram.

To compare the photograph and the rendered images programmatically, the photograph and images were carefully cropped and scaled such that the photograph could be matched pixel-wise with the image. This was done by the following Linux command that utilizes the ImageMagick *convert* program:

```
for f in white_0*.png; do
    convert $f -crop "295x108+97+115" \
        -geometry 557x205! ../WhiteLogoPngMine/$f
done
```

Where the parameters were found through a trial-and-error effort.



(a) Photograph of White Logo hologram



(b) Rendered image #0663 taken with the virtual camera on the far-right hand side of the track



(c) Rendered image #0360 taken with the virtual camera approximately in the center of the virtual track at a similar angle to that used by the real camera that took the photograph



(d) Rendered image #0000 taken with the virtual camera on the far-left hand side of the track

Figure 4.2: White Logo photograph and rendered images

4.2. PHOTOGRAPH ANALYSIS

Appendix D gives the program listing for the code used to analyze the difference between the photograph and the rendered images. The results are shown in Figure 4.3. There is a strong correlation for the low intensity pixels (the black areas of the image) and a much weaker correlation for the high intensity pixels.

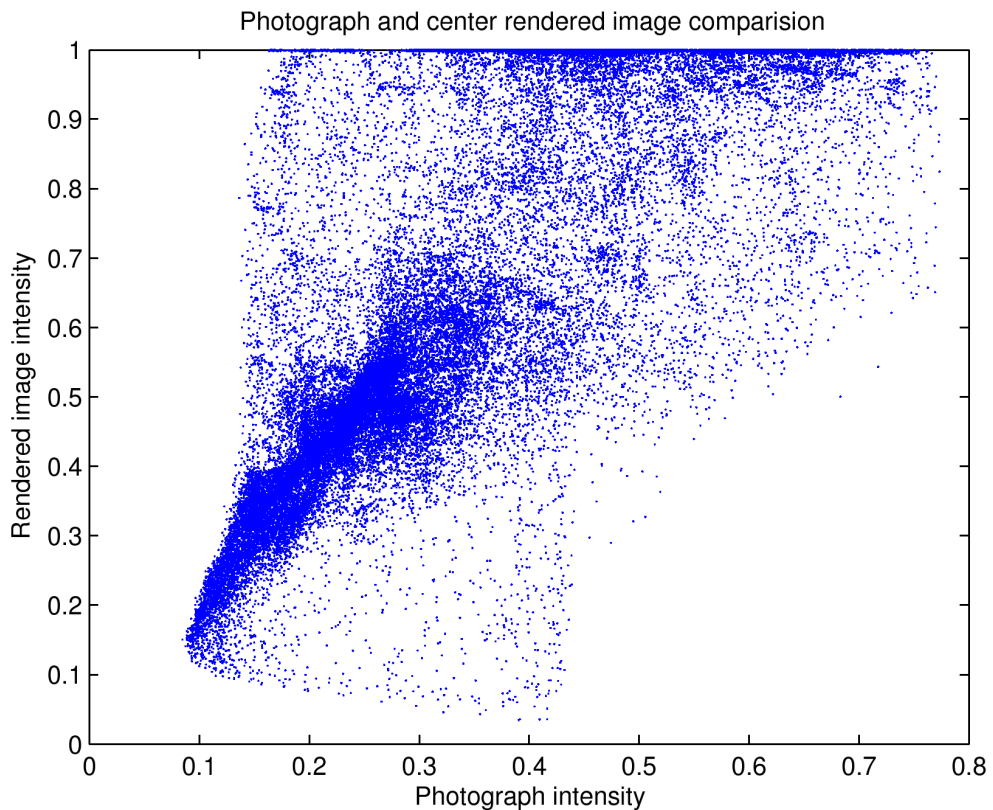


Figure 4.3: A plot of the intensity of each pixel on the photograph of the White Logo hologram plotted against the corresponding pixel on the rendered image shown in Figure 4.2c on the previous page. The intensity scale is arbitrarily between 0 and 1 where 1 is a brighter, and 0 is darker. The images were converted to greyscale and a Gaussian blur of 2 pixels in the horizontal direction applied first.

It is the difference in intensities between the photograph (actual intensity) and the center rendered image (intended intensity) that we are interested in, as it is this difference that we need to compensate for. This difference is a function, f , of the corresponding pixel on all of the rendered images. Indicating the photograph intensity at a point (x,y) as $P(x,y)$, the intensity of the center rendered image as

4.2. PHOTOGRAPH ANALYSIS

$I_{\text{intended}}(x, y)$, the intensity of a rendered image number 'i' as I_i , we obtain:

$$P(x, y) \approx f(I_{\text{intended}}(x, y), I_1(x, y), I_2(x, y), \dots) \quad (4.1)$$

The simplest non-trivial possible function is a simple summation of the intensities of a given pixel on all the rendered images (termed 'total intensity'). This function will be tried, as so:

$$P(x, y) \approx f\left(I_{\text{intended}}(x, y), \sum^i I_i(x, y)\right) \quad (4.2)$$

A plot of the difference in actual and intended intensity against the total intensity is given in Figure 4.4 on the following page. This shows a mostly-linear correlation of approximately $y = -1.8x + 0.04$ or, rearranging, $x = -0.54y + 0.02$. Putting this into Equation (4.2):

$$P(x, y) \approx -0.54 \times \sum^i I_i(x, y) + 0.02 + I_{\text{intended}}(x, y) \quad (4.3)$$

Using Equation (4.3) the photograph can be modified to attempt to retrieve the intended image. Applying the formula to the color photograph produced a few intensities that were outside of the range 0 to 1. Where this happened, the value was rounded down to 1. The final results are shown in Figure 4.5 on the next page. While this is a large improvement, it is clear that the separate colors need to be handled separately. Since the hologram was printed with red (770 nm), green (532 nm) and blue (440 nm) laser light, the image was analyzed in the RGB color space.

4.2. PHOTOGRAPH ANALYSIS

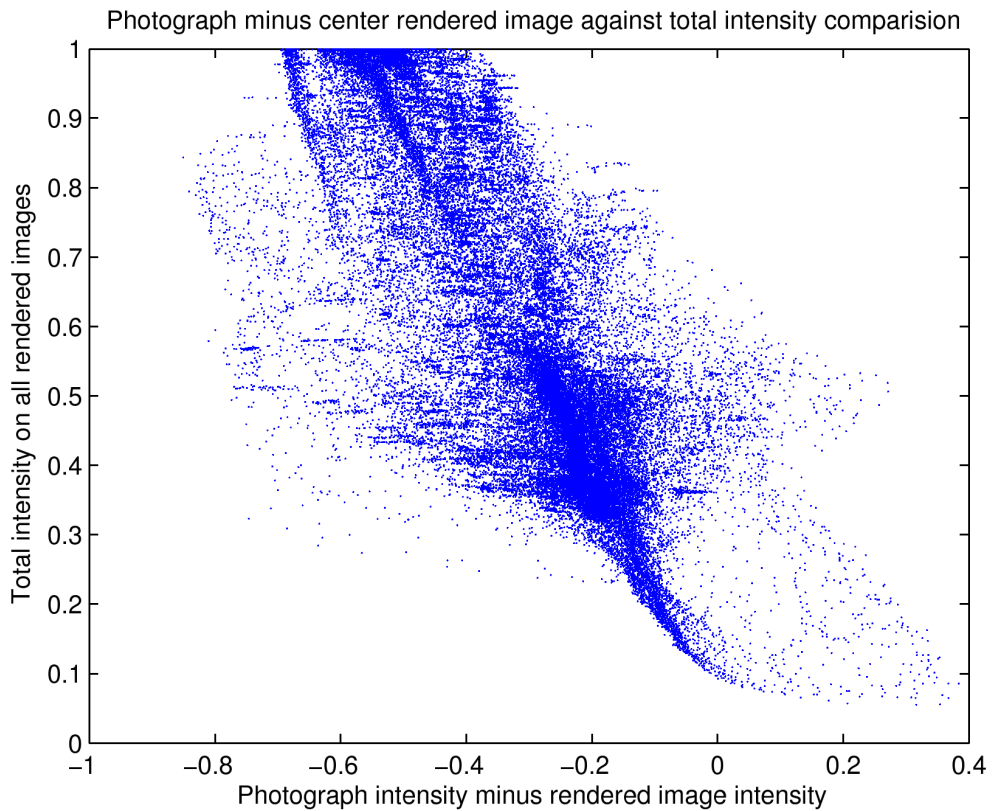


Figure 4.4: A plot of the intensity of each pixel on the photograph minus the intensity of the corresponding pixel on the center rendered image of the White Logo hologram, plotted against the corresponding total intensity of that pixel. The total intensity is a summation of the intensities of the given pixel for all of the rendered images. The intensity scale is arbitrarily between 0 and 1 where 1 is a brighter, and 0 is darker. The images were converted to greyscale and a Gaussian blur of 2 pixels in the horizontal direction applied first.



Figure 4.5: The photograph shown in Figure 4.2a on page 74 with Equation (4.3) on the previous page applied to each pixel

4.2. PHOTOGRAPH ANALYSIS

To attempt to produce better results, each channel was processed separately in the RGB color space, and the results are shown in Figure 4.7 on the following page.

The graph of the red channel, Figure 4.7a, has the least correlation, but attempting a correlation anyway we get a linear correlation of approximately $y = -1.5x + 0.2$ or, rearranging, $x = -0.67y + 0.08$.

The green channel, Figure 4.7b, has better correlation but strongly appears to be non-linear. Attempting a linear correlation anyway, we get a correlation of approximately $y = -2.0x$, or $x = -0.51y$.

Finally, the blue channel, Figure 4.7c, has a strong linear correlation of approximately $y = -2.8x - 0.2$, or $x = -0.36y - 0.07$.

Using these corrections with Equation (4.2) on page 76 but applying the correction separately to each channel, Figure 4.6 is obtained.

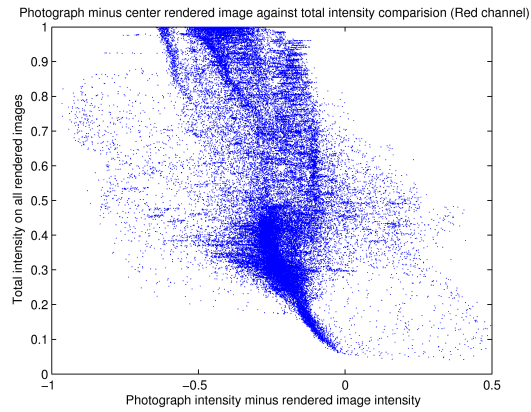


Figure 4.6: The photograph shown in Figure 4.2a on page 74 with the correction applied to each pixel. Each color channel was corrected separately, in RGB color space.

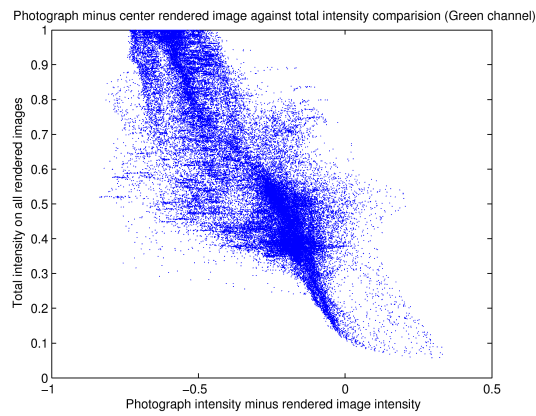
This is subjectively better, but not entirely satisfactory. It is still clearly brighter in between the letters. Further work would be required on this.

To get a better analysis of the hologram, a spectrometer was used instead of a photograph. This required a framework to support the spectrometer. This is discussed in the next section.

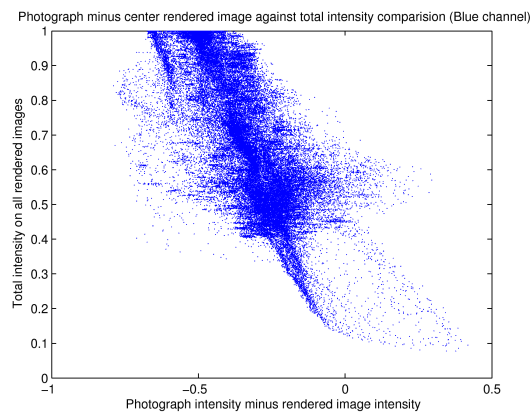
4.2. PHOTOGRAPH ANALYSIS



(a) Red channel



(b) Green channel



(c) Blue channel

Figure 4.7: A plot of the intensity of each pixel on the photograph minus the intensity of the corresponding pixel on the center rendered image of the White Logo hologram, plotted against the corresponding total intensity of that pixel. Each color channel has been plotted separately.

4.3 Spectrometer

To measure the diffraction efficiency of the hologram, a framework was required to hold a hologram, a light source, and a spectrometer in a reliable and consistent way. This was to allow the visible-light spectra and intensity of individual pixels to be compared between multiple points on a hologram, and between multiple prints of hologram.

The framework shown in Figure 4.8 was constructed for this purpose and is suitable for any white-light viewable visible-light reflection hologram. This framework consists of: a heavy metal screen which is securely mounted onto an optical table; a gantry system to allow two dimensional movement parallel to the screen; a fine-control mount with three degrees of freedom; a spectrometer and a light, mounted to the fine-control mount; and a Personal Computer (PC).

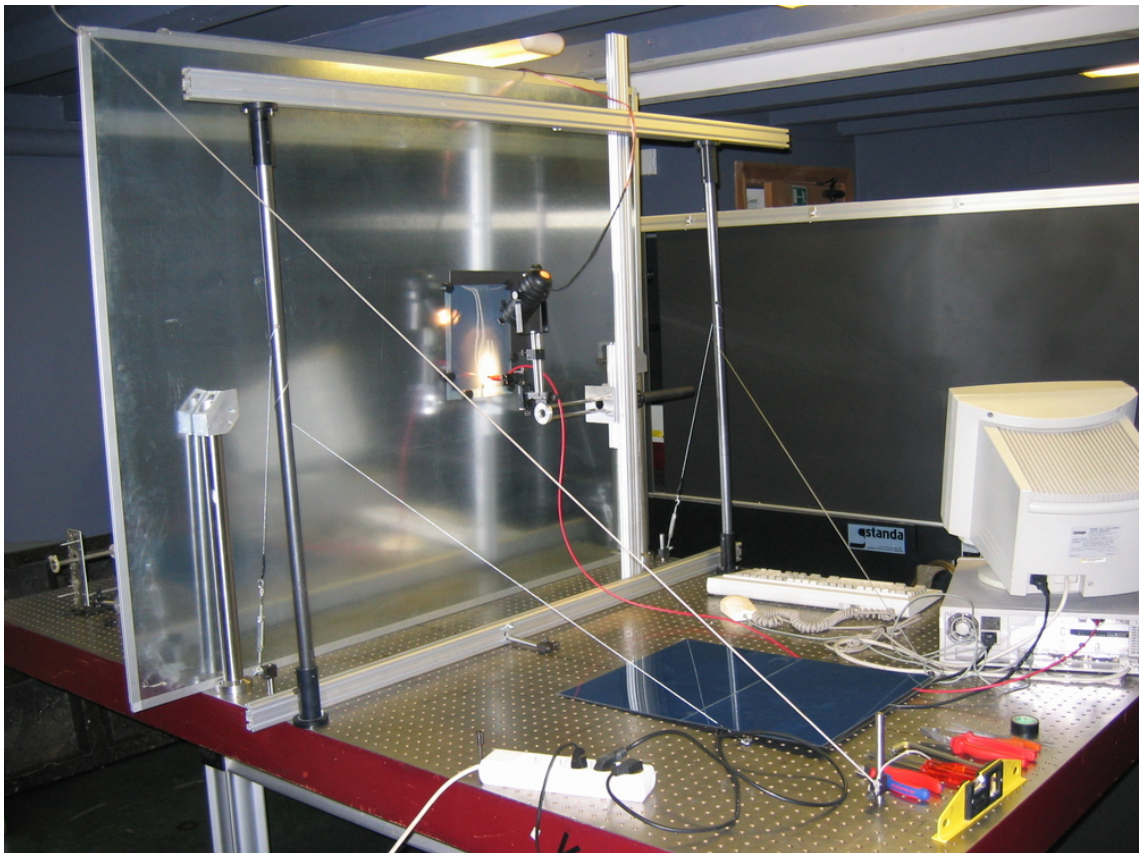


Figure 4.8: Photograph of framework for spectrometer and halogen light

4.3. SPECTROMETER

The metal screen can hold a hologram of up to $1.5\text{ m} \times 1.5\text{ m}$ in size and is magnetic, allowing fragile holograms to be held in place with magnets. The main 2D gantry system was greased for easy movement and can be locked in place with thumb-screws, to prevent accidental movement. The fine-control mount allows the 60W halogen light to be held at almost any angle and height relative to the spectrometer, and allows movement both parallel and normal to the screen. This can also be locked into place to prevent accidental movement. The angle of the halogen was set to the designed replay-angle for the holograms – equal to the reference beam angle, 37° to the normal of the hologram, as shown in Figure 4.9.

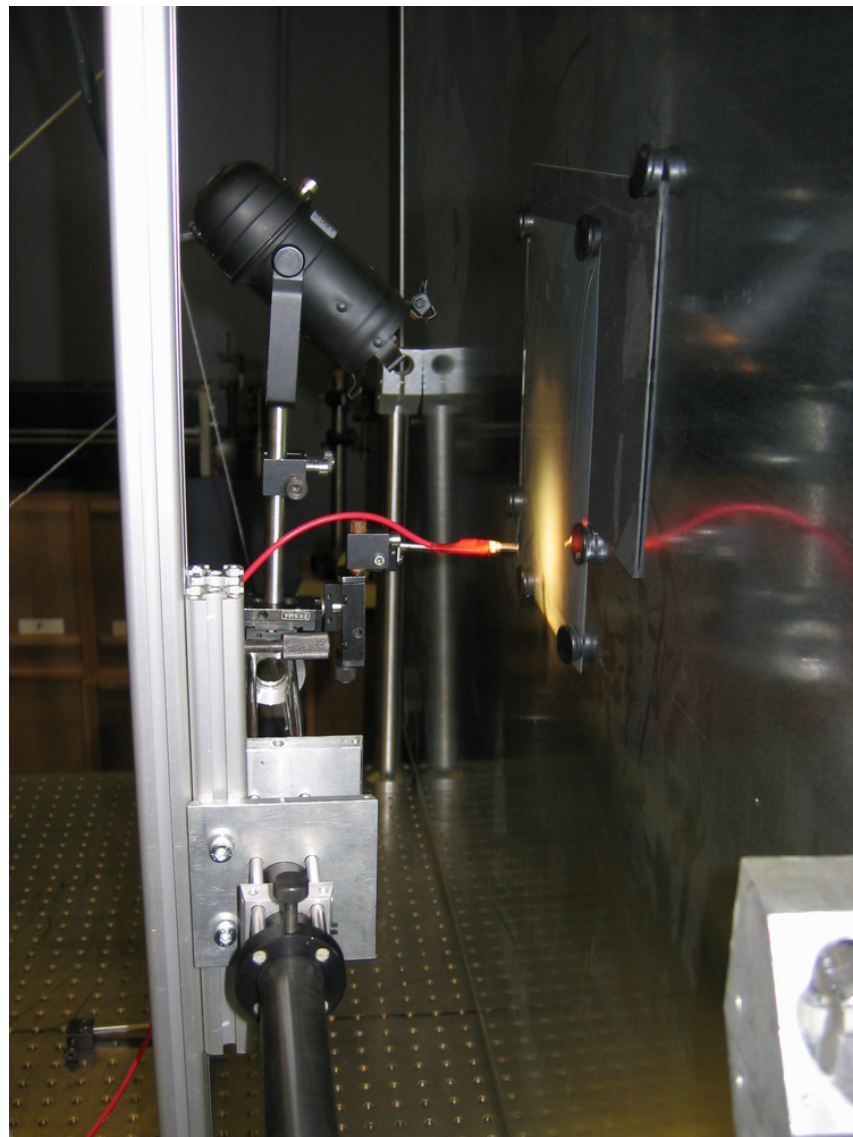


Figure 4.9: Photograph of fine-control spectrometer mount

4.3. SPECTROMETER

The details of the spectrometer are given in Table 4.1. The spectrometer was connected to a PC running *OOIBase for Windows* and *SpectraWin*, and was calibrated against a sheet of glossy white paper. Figure 4.10 shows the framework in use on a white-light reflection hologram.

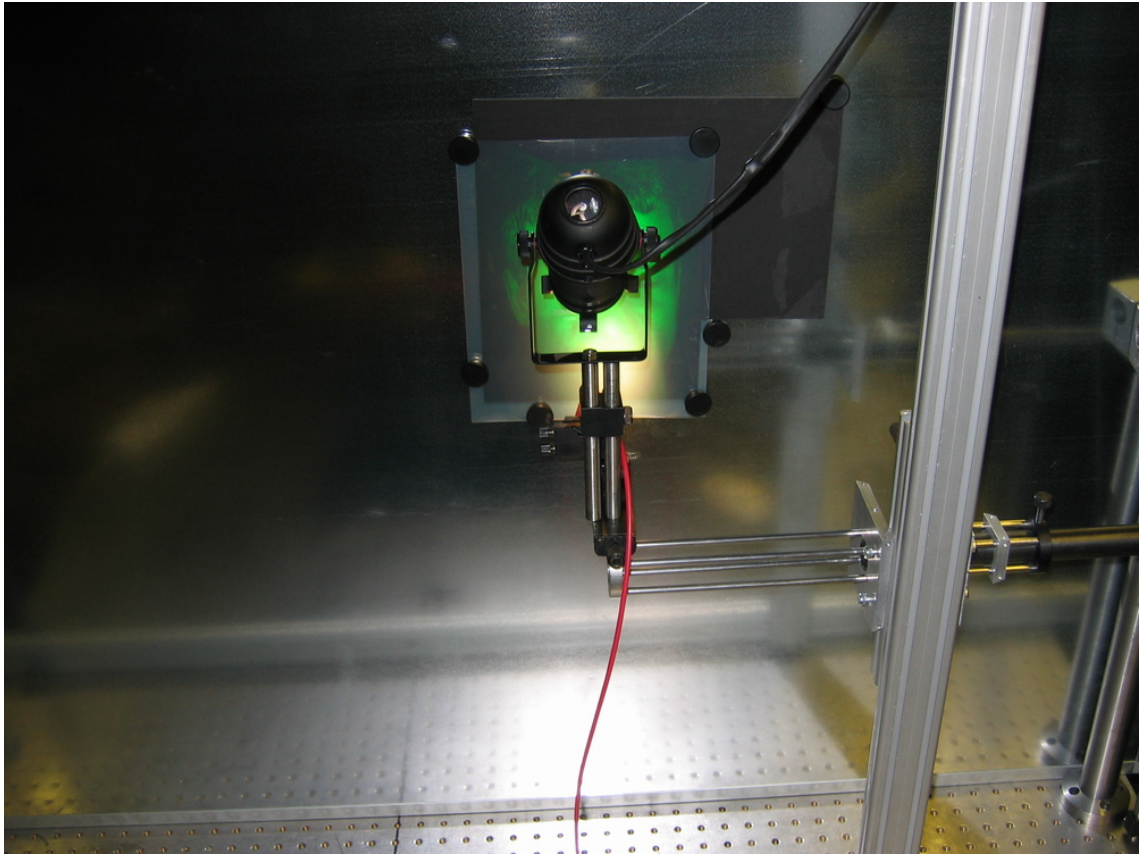


Figure 4.10: Photograph of spectrometer in use

Company:	Ocean Optics Europe
Model:	PC2000-ISA
Description:	PC Plug-in Fiber Optic Spectrometer
Grating:	600 lines blazed at 500 nm
Bandwidth:	350-1000 nm
Options Installed:	25 μm Slit
Serial:	PC2E637
Sample time:	from 3 ms to 60 s

Table 4.1: Technical details of spectrometer

4.3. SPECTROMETER

Using the spectrometer framework on the White Logo hologram, the results shown in Table 4.2 were obtained.

Position	Red Channel		Green Channel	
	Wavelength	Intensity	Wavelength	Intensity
White Region	625	33	505	28
In between the 'n'	627	145	508	106
Next to top of H	628	120	509	85
Next to the dot in 'i'	628	131	508	94
Next to floating sphere	629	181	509	150
In the middle of the 'c'	628	110	509	73
In the middle top of 'c'	629	194	509	133

Table 4.2: Wavelength and counts per minute for peak counts per minute in red and green channel. Wavelength is in nanometers, and intensity in counts per minute, as measured by the spectrometer detailed in Table 4.1 on the previous page.

To test the accuracy the photograph of the White Logo hologram (Figure 4.2a on page 74), the equivalent pixels in the photograph were compared against the intensity recorded by the spectrometer. Table 4.3 shows the RGB values for the equivalent pixels in the photograph, and Figure 4.11 on the following page is a graph of the two sets of results plotted against each other, for each pixel and for each channel.

Position	Red Channel	Green Channel	Blue Channel
White Region	130	114	125
In between the 'n'	208	135	164
Next to top of H	179	133	150
Next to the dot in 'i'	174	118	149
Next to floating sphere	178	129	151
In the middle of the 'c'	171	124	149
In the middle top of 'c'	211	151	171

Table 4.3: Photograph intensity for the same position and angle as used by Table 4.2. The values have the range 0 to 255, with 255 being the maximum intensity.

4.3. SPECTROMETER

Spectrometer readings against pixel intensities on photograph for White Logo hologram

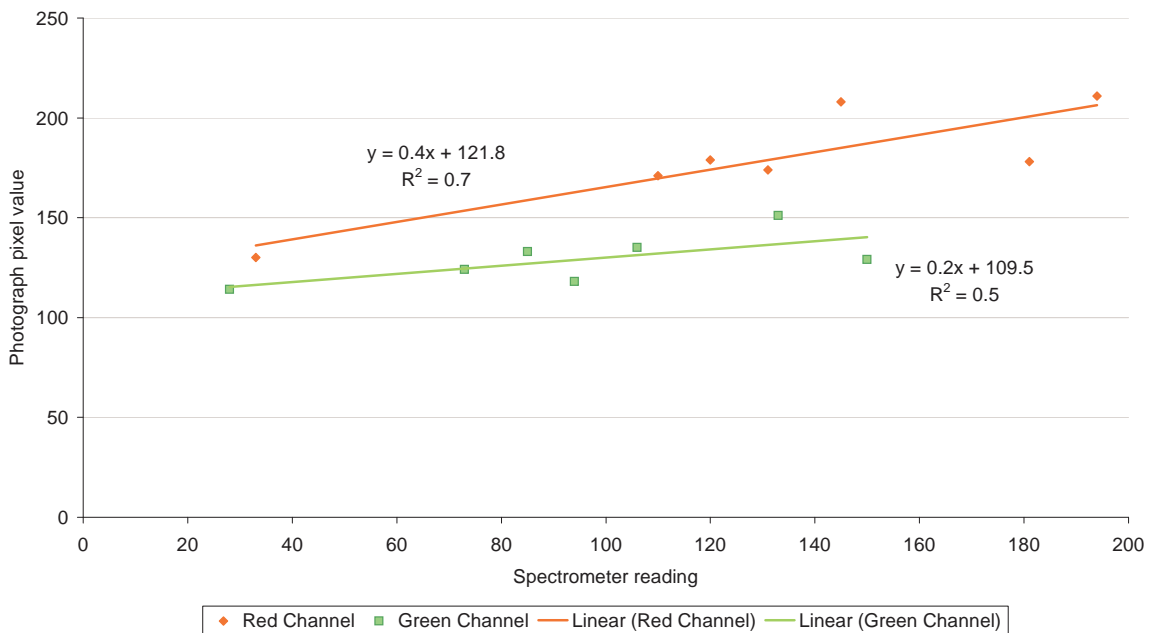


Figure 4.11: Spectrometer readings (From Table 4.2 on the previous page) plotted against the intensity value recorded by the camera for the same position and same angle (From Table 4.3 on the preceding page). A linear-regression best-fit line is shown for the two color channels. The blue channel was not measured.

Figure 4.11 shows that the results from the camera do not match to sufficient precision to the results from the spectrometer. This could be due to experimental error, or an indication that the chosen camera was not of sufficiently quality to capture a true-image of the scene. If the image from the camera was not an accurate depiction of the light from the hologram, then this may explain some of the noise in the results found in Section 4.2 on page 73.

4.4 Future work

A more accurate correction algorithm that could remove most of the ghosting problems would be a useful future work. This work could be based on a theoretical approach to the problem, using coupled-wave theory to determine the exact correction algorithm required. This algorithm can then be applied to the rendered images so that the final printed hologram appears without any ghosting effects.

To provide a better avenue for investigation, a hologram was printed such that the width of the viewing window is decreased for each holopixel, from left to right. This was achieved by displaying a solid green rectangle of decreasing width on the LCOS display. The results are given in Figure 4.12 on the next page. The twelve lines were all printed the same, to allow for a more accurate analysis.

It is clear that the larger viewing window (to the left hand side of the photograph) results in a dimmer image in the direction normal to the hologram. It would be useful future work to use the photographs to better analyze, and correct for, this problem. To further help with the problem, several holograms were also printed with the object beam energy decreasing in steps. This was achieved by changing the intensity of the rectangle display on the LCOS after every five rows. Figure 4.13 on page 87 shows a photograph of a such a hologram. It is left as future work to analyze these.

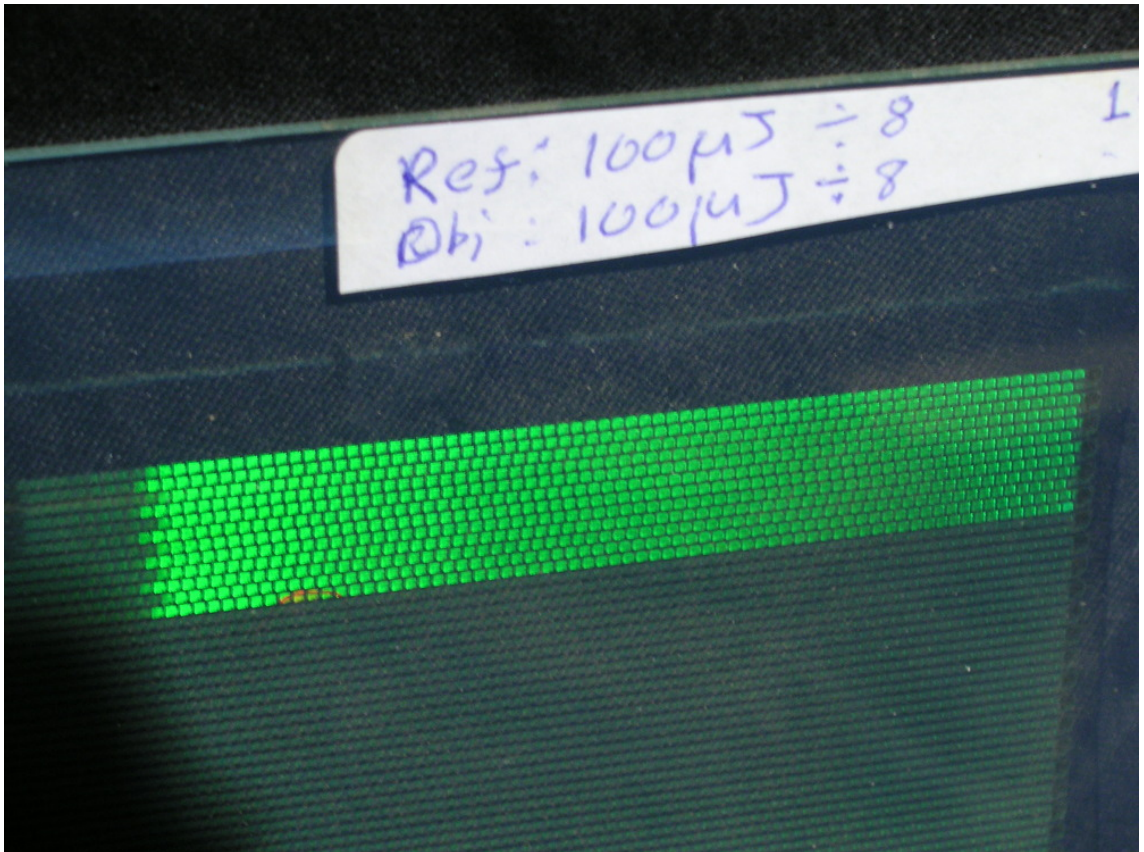


Figure 4.12: Photograph of hologram with decreasing viewing window. The holopixels on left hand side of the photograph have the smallest viewing window. Note that the label is indicating the laser energy was $100 \mu\text{J}$, as measured after the wave plates and polarisers. This was then decreased by a factor of eight through the use of Neutral Density Filters (NDF). The '1' in the top right indicates that this was the first attempt, for the case that the hologram had to be reprinted. The pixels are square and 1.0 mm wide with a 2.0 mm separation between centers. The photograph was taken with a $f/5.0$ aperture and $1/6$ second exposure time. One complete row is approximately 7.5 cm across.

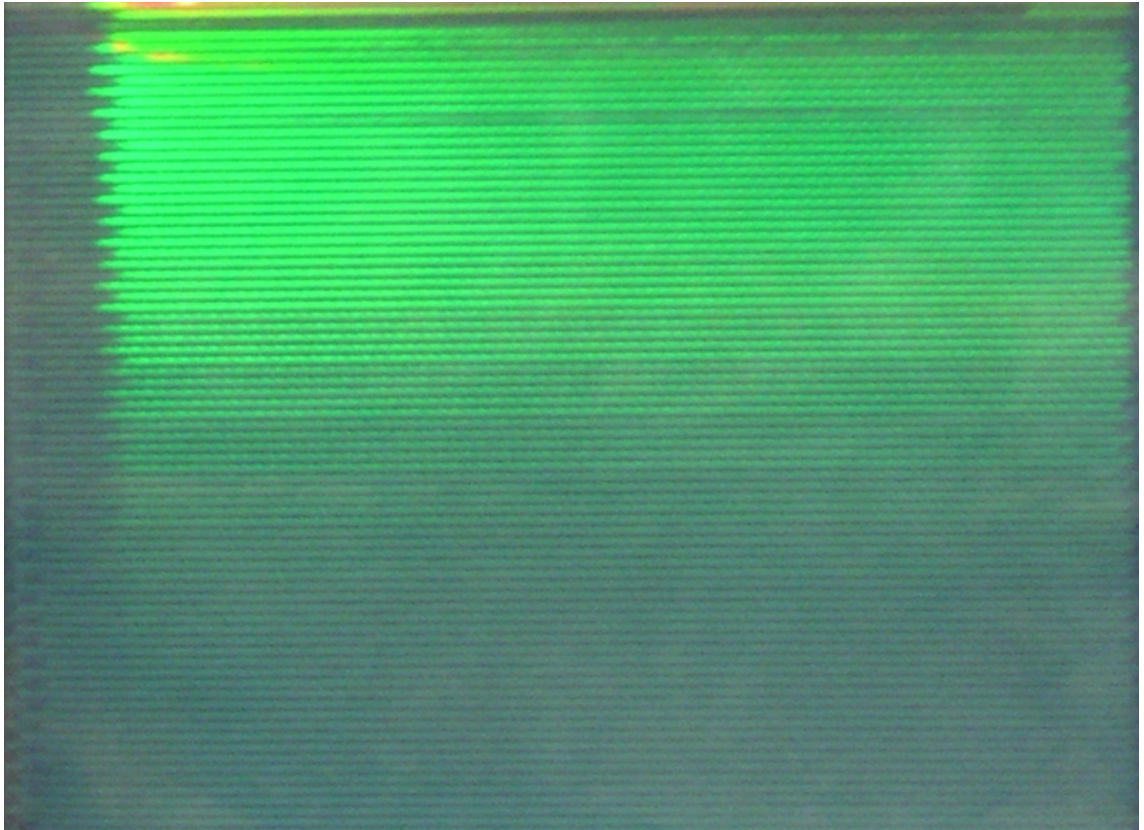


Figure 4.13: Photograph of hologram with decreasing viewing window from left to right and decreasing reference beam energy top to bottom. The reference beam energy is decreased in steps, with 5 rows printed for each energy. The pixels are square and 1.0 mm wide with a 2.0 mm separation between centers. The photograph was taken with a f/5.0 aperture and 1/3 second exposure time.

4.5 Summary

A sample hologram was found to have visual 'shadows' or 'ghosting' where the size of the viewing window of a holopixel was determined to be affecting the apparent brightness of the holopixel in any given direction. A photograph of the hologram was compared to the set of rendered images and the intended image, and correction algorithms were proposed. The correction algorithms were applied to the photograph and found to improve the image. These algorithms can be applied to rendered images before printing to correct for ghosting.

The algorithms can also be used to inform the artists where ghosting would occur, to allow them to adjust the model to remove any problem areas.

To better measure the hologram, a framework was built to hold and position a spectrometer and halogen light. This gave good results and preliminary tests indicate that the camera was not accurately photographing the hologram intensity.

Future work is required to find a more optimal algorithm for correcting for ghosting, using a similar spectrometer framework and analysis code.

5

Printing speed and resolution improvements

This chapter investigates methods to speed up the printing of digital holograms and ways to increase the holopixel resolution. Sensitivity analysis methods are applied to determine the required mechanical stability of the hologram plate holder. In addition to various other improvements, the power supply is replaced, the PC software driving the printer is improved to run at a faster speed, and the LCD display is replaced with an LCOS display.

5.1 Overview

A monochromatic hologram printer similar to that described by Ratcliffe et al. [47] is investigated for possible speed increases. The printer design described by Ratcliffe et al. is limited by both hardware and software to printing at four pixels

per second.

This is an acceptable printing speed when printing 1.0 mm by 1.0 mm pixels on a small plate. A small holographic plate produced, for example, by Slavich [65] is typically around 127 mm by 102 mm - a total of 12954 pixels at 1.0 mm × 1.0 mm. At 4 pixels per second, it would take just under an hour (54 minutes) to print.

This quickly becomes undesirable for a larger plate or for a higher resolution. It can take many hours or even days to print a large one meter squared hologram. Additional problems can occur if the printing times are too long; the initial pixels 'fade' by the time the last pixels have been printed. Various techniques have been established with varying success in an attempt to compensate for this. One technique is to use a dim incoherent white-light source, such as a 25 W lamp at a meter or so from the hologram. This technique is known as latensification, and its effect on green pulsed holography has been shown to be effective [76].

With a high resolution print with pixels of size 0.3 mm x 0.3 mm, it would take approximately 9 hours to print even the small plates mentioned.

To speed up the printing, both hardware and software adjustments were required.

5.2 Power supply

The laser used inside the hologram printer detailed by Ratcliffe et al. is flash-lamp pumped, requiring the power supply to provide bursts of energy at precise regular intervals. The power supply was fundamentally limited to 10 Hz, thus limiting the number of laser pulses to a maximum of 10 per second. This was replaced with a newer design of power supply provided by Geola Technologies Ltd [77], capable of an operation of up to 50 Hz. The new power supply contains a larger charging unit and uses a standard simmer system to keep the flash lamp semi-powered continually. This also increases the lifetime of the flash lamp

by two to five times longer. The technical specification of the laser are given in Appendix H.

5.3 Stability

With a faster operation, the motors provided more vibrations requiring the system to have a higher mechanical stability. Because the beam pulse is short (approximately 50 ns) compared to the vibrations, the system is essentially completely still during the exposure – vibrations on the microscopic scale do not affect the exposure or the print. This is different to that of CW hologram printers that do suffer from even the slightest of vibrations. At the macroscopic scale, however, small vibrations can move the point that the reference beam exposures laterally, causing the reference and object beams to overlap only partially, or even not overlap at all. This effect is more pronounced at higher resolutions because of the smaller overlap area. At high translational velocities the stage motor vibrations can also compound this effect to further reduce the overlap area.

Figure 5.1 on the next page shows the intersection of the object and reference beams at the hologram plate. It is important to maintain some minimum overlap of the object and reference beams, O and R respectively, at the plane of the holographic plate (see Figure 5.2 on page 93).

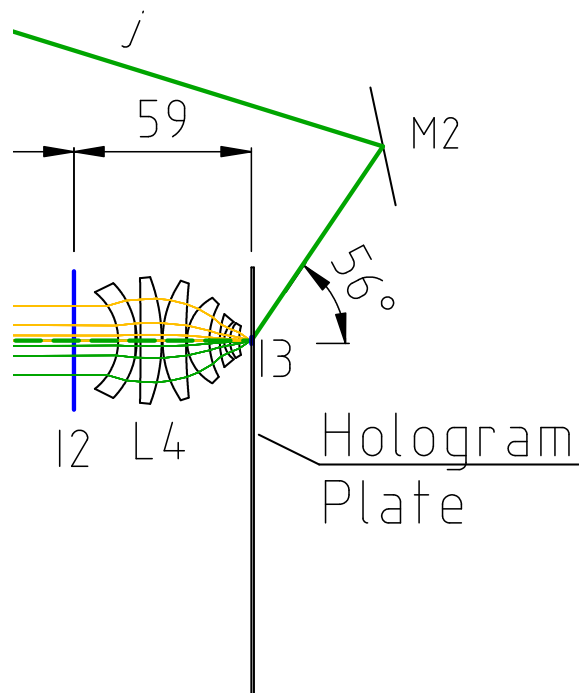


Figure 5.1: Diagram showing the plane of intersection of the hologram plate and the object and reference beams (shown in dashed and solid lines respectively). The object beam is also shown raytraced through the objective lens for clarity. A full diagram is shown in Figure C.4 on page 157.

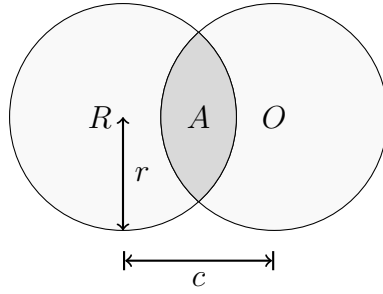


Figure 5.2: The object (O) and reference (R) beam profiles, of radius r , at the plane of the hologram plate can become misaligned by a distance c .

Since the two beams are approximately circular they have reflectional symmetry about the chord that crosses through their intersection points. Thus we can find the area in one half of the intersection, and double that to obtain the total area of overlap.

The total area, A , of overlap of two circles of radius r and distance c between the centres of the two beams, is thus given by:

$$A = 2(q \cdot r^2/2 - \sin(q) \cdot r^2/2) \quad (5.1)$$

$$= r^2(q - \sin(q)) \quad (5.2)$$

where

$$q = 2 \cdot \cos^{-1}(c/(2r)) \quad (5.3)$$

Since the area of a circle is $\pi \cdot r^2$, dividing through by this obtains the percentage overlap, $P(c, r)$, of the two beams:

$$P(c, r) = \frac{(q - \sin(q))}{\pi} \quad \text{where} \quad q = 2 \cdot \cos^{-1}(c/(2r)) \quad (5.4)$$

To get a numerical feel for these equations, two different beam sizes and two different minimum overlaps will be considered. The design described by Ratcliffe et al. [47] uses circular pixels with a radius of 0.5 mm. For the purpose of setting

a specific target, this will be compared to using round pixels with a radius of 0.15 mm - a pixel that is one order smaller in area.

For a minimum overlap of 90% of the two beams on the photographic plate, with the object and reference beams both having a radius of 0.15 mm (and hence a height and width of 0.3 mm), and by solving the above equation numerically¹, it can be seen that the distance between the two centres must not be greater than 0.02 mm. The results shown in Table 5.1 are obtained by solving the equation for the larger beam size of 1.0 mm in radius, and also repeating with a higher resolution beam separation of 0.3 mm.

Overlap	Beam size	Separation
70%	1.0 mm	0.24 mm
	0.3 mm	0.07 mm
90%	1.0 mm	0.08 mm
	0.3 mm	0.02 mm

Table 5.1: Maximum reference and object beam separation distance for certain beam diameters and a minimum beam overlap

To increase the resolution of a hologram by changing from a pixel size of 1.0 mm diameter to pixels with a 0.3 mm diameter, the alignment needs to be approximately four times better to achieve the same overlap area. A sensitivity analysis shows that the relative sensitivity of the percentage overlap, P , as the distance c between the centers of the two beams is changed is²:

$$\text{Relative sensitivity of } P \text{ w.r.t. } c = \frac{c}{P} \cdot \frac{\partial P}{\partial c} \tag{5.5}$$

$$= \frac{2c(\cos(q) - 1)}{(q - \sin(q))\sqrt{4r^2 - c^2}} \tag{5.6}$$

Equation (5.6) shows that the sensitivity increases with the beam separation, c , and inversely with the beam radius, r . However the sensitivity remains quite

¹Equation solved numerically in Maxima with the command: `find_root((2*acos(c/(2*r)) - sin(2*acos(c/(2*r)))) / %pi - p, c, 0, 0.15), r=0.15, p=0.9;`

²Equation solved analytically in Maxima with the command: `P(c) := (2*acos(c/(2*r)) - sin(2*acos(c/(2*r)))) / %pi; factor(diff(P(c), c) * c/P(c)); % , 2*acos(c/(2*r)) = q;`

5.3. STABILITY

low for the values we are considering. For example, for a beam radius of 0.15 mm, and a separation of 0.07 mm (giving an overlap of 70%), the sensitivity of P with respect to c is only 40%; the percentage overlap of the two beams will increase by only 40% of the percentage change in the separation of their centres.

Likewise, the sensitivity of P with respect to the beam radius r is³:

$$\text{Relative sensitivity of } P \text{ w.r.t. } r = \frac{r}{P} \cdot \frac{\partial P}{\partial r} \quad (5.7)$$

$$= -\frac{2c(\cos(q) - 1)}{(q - \sin(q))\sqrt{4r^2 - c^2}} \quad (5.8)$$

This is of the same magnitude as the relative sensitivity of P with respect to c .

For a maximum beam movement of 0.05 mm laterally, the reference beam mirror (labelled M2 in Figure 5.1 on page 92) must also remain stationary by approximately the same amount. To achieve this, the mirror was mounted on a metal rod, which was secured to the table. Lateral movement was restricted by an 'A'-shaped structural support system. This was found to be sufficient to mechanically damp vibrations from the motors, and also withstand the occasional accidental knock without knocking the system out of alignment.

Further mechanical stability adjustments are detailed in Section 5.6 on page 99 in the context of speeding up the movement of the stages. The subject comes up again in Section 5.7 on page 100 in the context of decreasing the size of the pixels.

³Equation solved analytically in Maxima with the command: `P(r) := (2*acos(c/(2*r)) - sin(2*acos(c/(2*r))))/%pi; factor(diff(P(r),r) * r/P(r)); % , 2*acos(c/(2*r)) = q;`

5.4 Software

The original software for the hologram printer was designed for low speed printing. The basic algorithm of the code is listed in Algorithm 1.

```

1 Calculate the speed at which to move the plate vertically;
2 Move vertical stage to first pixel to print;
3 foreach vertical row of pixels do
4   Start moving the vertical stage downwards at the calculated speed;
5   foreach pixel in the vertical row do
6     Display next pixel information on the LCD/LCOS screen;
7     Call the windows function sleep(int milliseconds) to wait
      until the stage has moved into position;
8     Trigger the laser to fire a pulse;
9   end
10  Start moving the horizontal stage by the width of one pixel;
11  Start moving the vertical stage back to the starting position;
12  Wait until both stages are in position;
13 end

```

Algorithm 1: Printing algorithm suitable for printing at low speed

There are several significant problems with this algorithm when trying to scale it to faster speeds:

- The granularity of the sleep function is by default 10 milliseconds.
- There is no attempt to deal with ‘drift’ – it assumes that the sleep will be for a time specified, and that there will be no unforeseen delays. Any problems will not be corrected for.
- The LCD/LCOS takes a while to display the next image. At high speeds we risk the LCD/LCOS not being updated by the time we print.
- At faster speeds, the stage can have a significant inertia, resulting in a non-negligible acceleration time.
- At low speeds, moving the vertical stage back to the starting position is many times faster than the printing. At fast speeds it starts to take up a significant amount of time compared to the printing itself.

Consider the first of these points. The sleep time required will depend upon the speed at which we print. For printing at 4 Hz, we will need the total time between printing pixels to be approximately 250 milliseconds. For printing at 30 Hz, we will need the total time to be approximately 33 milliseconds.

From profiling the code, we found it takes approximately 20 milliseconds to fetch the next pixel data and display it on the screen. The system must then sleep for approximately 230 milliseconds at 4 Hz, and 13 milliseconds at 30 Hz.

By default, the sleep function has a granularity of 10 ms. So a call to sleep for, say, just under 225 ms will actually sleep for 230 ms – an error of 2%. A sleep for 13 ms will sleep for 20 ms, however, an error 65%. For short sleep times, the error is actually much worse than this⁴ (See Figure 5.3). This is because the kernel can take an arbitrary amount of time in processing interrupts, I/O calls etc. While handling interrupts etc, even a real time process cannot be scheduled.

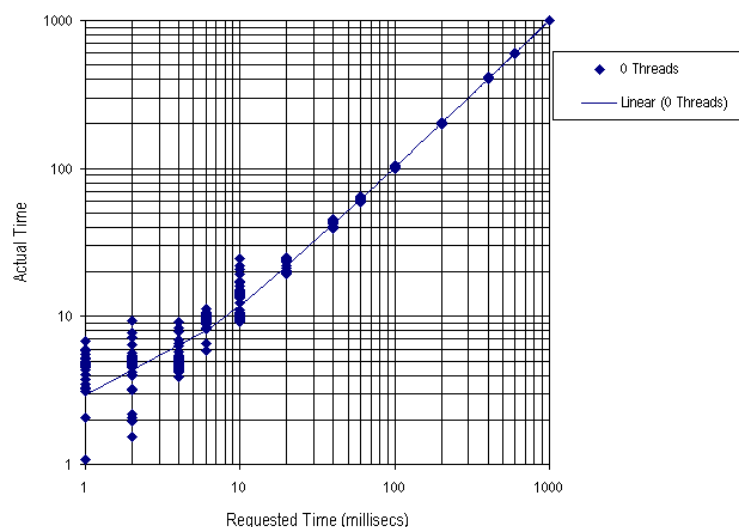


Figure 5.3: Behavior of Microsoft Windows `sleep()` function

The first step to solving this is to increase the time granularity. We can use the system call: `timeBeginPeriod(1)`; which sets the granularity at around 1 or 2 milliseconds. This reduces our average error at 13 ms to $2\text{ ms}/13\text{ ms} = 15\%$. However the situation is worse than this because it will always sleep for a mini-

⁴Source <http://www.codeproject.com/system/sleepstudy.asp>

5.5. DISPLAY SYSTEM REFRESH RATES

imum of the time we give it i.e. the error is always in one direction, never lower than the specified time. This means that the error will accumulate much faster than the usual random walk $\log(n)$; we would drift by a whole pixel after printing around 33 pixels, or 1 cm of printing. A drift of one pixel per centimeter is clearly not acceptable.

One possibility it to write our own sleep function that further increases granularity by getting the CPU time and spin-lock until the time desired is reached. However this is known to be unreliable under high Input/Output (I/O) activity, which we may have from reading the hard disk.

Instead we opted for using the one millisecond granularity sleeps combined with continually adjusting the sleep time to compensate for drift. This should insure that the system is never more than one millisecond out of step. The drift is tracked by using the win32 system function `timeGetTime()` and comparing the returned result against the expected time. The delta is then subtracted from the base sleep time. For better results, this should ideally be done on a real time Operating System (OS), such as a real-time MS Windows kernel, or a real-time Linux kernel. Alternatively the timing could be handled in hardware.

5.5 Display system refresh rates

The design detailed by Ratcliffe et al. [47] utilizes an LCD transmission display system, with a native 800×600 pixel resolution and capable of a refresh rate of 20 Hz. This means that with a simple implementation, the hologram printer can print up to ten holopixels per second (so that you are guaranteed at least one complete screen refresh before the pixel is printed.) With a more careful implementation, synchronizing the laser pulses to the video Vertical Synchronization (VSYNC), it would be possible to print at exactly twenty holopixels per second, but with little flexibility. The timing would need to be much more precise, and possible required dedicated timing hardware.

Instead a Liquid Crystal On Silicon (LCOS) display system was used. In particular the Brillian BR768HC LCOS which is capable of a refresh rate of 60 Hz with an 18 ms response time. The LCOS also has many other advantages, including a higher contrast of 2000:1 and a higher native resolution (1280×768).

5.6 Stage movement

The origin design's method of printing was to print a vertical column of pixels, from top to bottom, then returning the vertical stage back to the top while moving the horizontal stage across by one pixel.

There are multiple reasons for this method of operation:

- Moving the vertical stage back to the top is much faster than moving the vertical stage during printing. Thus as a percentage of time, it is insignificant.
- Without the timing auto-correction system as described in Section 5.4 on page 96 (Software), the pixels would drift from their correct positions. This can be crudely compensated for by always printing in the same direction. In this manner the drift is approximately the same for each column, and so does produce a noticeable effect.
- Simpler code. The pixel data can be loaded and processed sequentially.
- Mechanical stability. The horizontal stage needs time to move and settle down; it is an order slower than the vertical stage as the load is much higher (the horizontal stage carries the vertical stage).

The first point is no longer valid at fast speeds. At 30 Hz, the vertical stage moves almost at its maximum speed while printing. The second point will not be a problem when using the timing auto-correction system previously mentioned. The third point is not that significant.

5.7. INCREASING PRINTED HOLOPIXEL RESOLUTION

The mechanical stability was dealt with in two ways. The first step was to mount the vertical stage off-center on the horizontal stage. This added a frictional force which acted to stabilize the vertical stage. The second step ties in with one of the original problems, restated for convenience:

- At faster speeds, the stage can have a significant inertia, resulting in a non-negligible acceleration time.

By adding a small 'buffer' space above and below the plate, such that the vertical stage moves higher and lower than the bounds of the hologram plate, the vertical stage is given time to accelerate and the horizontal stage is given time to settle down. In practice, a buffer of 1cm on the top and bottom was sufficient.

5.7 Increasing printed holopixel resolution

The previous section dealt with increasing the speed at which 'holopixels' could be printed. Many of the improvements detailed had a secondary purpose in preparing the system for increasing the resolution of the hologram i.e. decreasing the size of the holopixels and decreasing the distance between their centres. The increased mechanical stability, for example, paves the way for more precisely placing the holopixels and hence allowing smaller holopixels.

Additional mechanical modifications were needed at higher resolutions, and these are specified below.

The vertical stage is mounted on a horizontal stage. To move the plate sideways, the horizontal stage is activated, thus moving collectively the vertical stage and plate holder horizontally. Although this is obvious, it is not so obvious that the angle of the axis that the horizontal stage moves along is not critical. The angular placement of the horizontal stage is not critical.

However it is critical that the hologram plate is held by the vertical stage in the correct way; it must be parallel to the axis of motion of both the horizontal and

5.7. INCREASING PRINTED HOLOPIXEL RESOLUTION

vertical stage. If the plate is not parallel enough, then during printing the part of the plate that is being exposed will move in the orthogonal direction, away or towards the main lens (indicated as lens L4 in Figure C.6 on page 159).

For an idea of the accuracy required, consider the case that we wish to print a hologram to a photosensitive plate with dimensions $W \times H$. Without loss of generality, we consider the horizontal direction only. If the plate is held at angles $\theta_{x,\text{error}}$ and $\theta_{y,\text{error}}$ to horizontal and vertical motion respectively, then when the furthest corner pixel is printed, the hologram plate will have moved a total distance, in the direction normal to motion, of:

$$\sqrt{W^2 \sin^2(\theta_{x,\text{error}}) + H^2 \sin^2(\theta_{y,\text{error}})} \quad (5.9)$$

Since $\theta_{x,\text{error}}$ and $\theta_{y,\text{error}}$ should be very close to zero, the approximation $\sin(x) \approx x$ is suitable. The situation can be simplified by considering a square plate (such that $W = H$), and by assuming that $\theta_{x,\text{error}}$ and $\theta_{y,\text{error}}$ are approximately equal and both cause normal motion in the same direction (the worst case scenario). Thus the maximum distance of normal motion, z_{max} , is:

$$z_{\text{max}} = \sqrt{2} \cdot W \theta_{\text{error}} \quad (5.10)$$

This affects the hologram because the reference beam strikes the hologram plate at an angle $\phi_{\text{reference}}$ to the normal of motion of the hologram plate. ($\phi_{\text{reference}}$ will be typically around 56° , close to the Brewster angle for glass). As the exposed area of the plate moves away from the lens L4 due to unwanted normal motion, the point at which the reference beam strikes will move laterally, ultimately resulting in the object beam and reference beam no longer fully overlapping.

5.7. INCREASING PRINTED HOLOPIXEL RESOLUTION

The maximum distance, c_{\max} , that the reference beam will become misaligned due to z_{\max} , is thus:

$$c_{\max} = z_{\max} \sin(\phi_{\text{reference}}) = \sqrt{2} \cdot W \theta_{\text{error}} \sin(\phi_{\text{reference}}) \quad (5.11)$$

Rearranging:

$$\theta_{\text{error}} = \frac{c_{\max}}{\sqrt{2} \cdot W \sin(\phi_{\text{reference}})} \quad (5.12)$$

If we assume that the beams are perfectly aligned in one corner, then the maximum distance between the centres of the two beams, c , will be equal to x_{\max} . We found previously that if we want to maintain at least a 70% overlap when both beams have a diameter of 1.0 mm, then the distance between the centres of the two beams must be at a maximum of 1.0 mm. Considering a plate of size, say, $W = 0.5$ m, and angle $\phi_{\text{reference}} = 56^\circ$ we can get an idea of the maximum angles of error. These are listed in Table 5.2.

Overlap	Beam Size	Separation
70%	1.0 mm	410 μrad
	0.3 mm	120 μrad
90%	1.0 mm	140 μrad
	0.3 mm	34 μrad

Table 5.2: Maximum tolerated angle deviation from the plane of a photographic plate for certain beam sizes and minimum overlap, at $\phi_{\text{reference}} = 56^\circ$ and $W = 0.5$ m

To achieve the high level of precision needed, an adjustable holding frame was made for the glass plate to allow adjustment of the angle of the plate. This was made from a Standa lens holder that allowed for two dimensional angle adjustments with an accuracy of between 1 to 2 μrad , sufficient for this application.

Alignment was done by eye. The beam energy was reduced to a few percent of the normal energy level (for both safety reasons and because it is easier to align when the beam is dim). A blank glass plate can then be covered in white masking

tape, and placed in the holder, with the masking tape closest to the main lens (where the emulsion would be located). It is best to use an actual hologram plate, as it is important that the glass plate is of the same thickness as the hologram plate that will be employed.

The plate was then moved (using computer control or otherwise) to one corner (meaning that the glass plate is moved so that the object and reference beams are illuminating one of the corners of the plate). The reference beam mirror (labelled M2 in Figure 5.1 on page 92) can then be adjusted until the beams overlap, judging this as best as possible by eye.

The glass plate is then moved (by computer control) so that the other corner is exposed. If the beams no longer overlap completely, the angles are adjusted, and the process repeated.

Although somewhat crude, this actually works fairly well in practice.

5.8 3D model

The produced holograms were based upon two different 3D models. The low resolution holograms used a 3D model of the KDE mascot, Konqi. For the higher resolution holograms, a greyscale, high contrast and high detail model was required. For this, the kind permission from Doug Ollivier was granted for the non-commercial use of his model of a futuristic tank model.

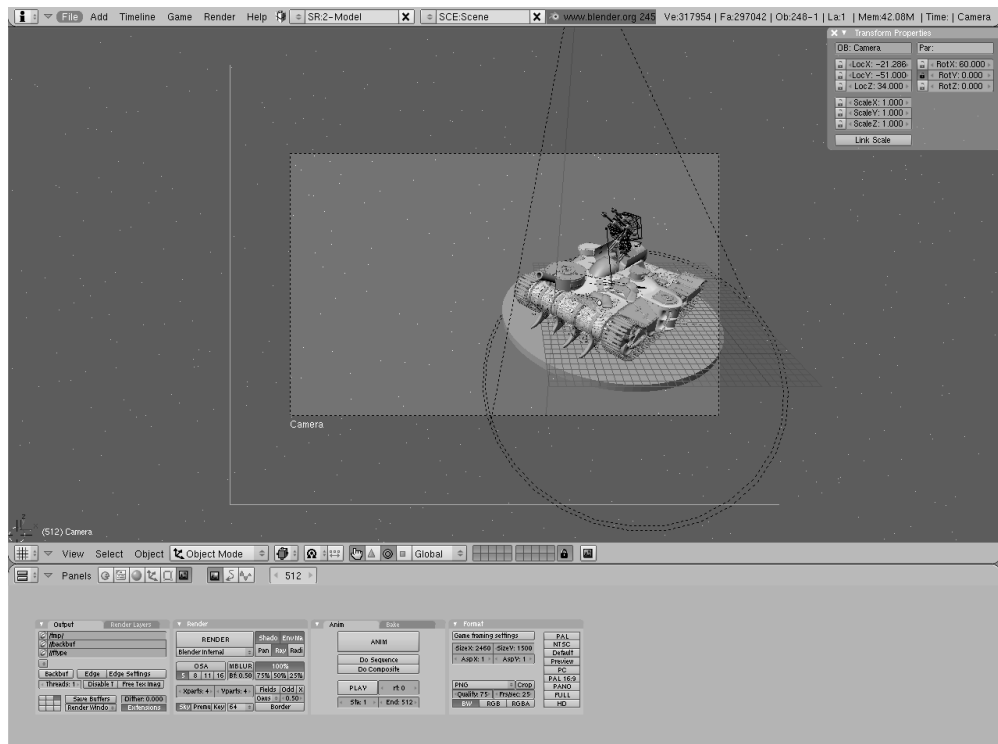
The increase in holopixel resolution meant that higher resolution images of the model are required. Additionally, the increase in pixels on the LCOS (1280×768 on the LCOS compared to 800×600 on the LCD) potentially means that more rendered images can be used, to provide a greater depth of the field. The LCOS is used in landscape orientation in the hologram printer, meaning that for single parallax holograms, up to 1280 separate images are required, each rendered from a slightly different angle. For full parallax, up to $1280 \times 768 \approx 1$ million images would be required.

To determine how to render the images from the 3D model for the horizontal parallax case only, an intuitive approach can be taken. The scene needs to be rendered from many different angles, producing an image for some discrete set of angles. By moving the virtual camera along a virtual track, keeping the camera pointed at the center of the scene, we can produce the required series of images. However these images will need to be algorithmically distorted as each image is taken at a different angle.

Instead, the camera was set to capture a view that was twice as wide as the scene. The virtual camera was first calibrated such that its field of view was equal to the field of view produced by the imaging lens system of the LCOS onto the hologram plate. The camera was then placed at a distance such that the scene took up exactly the whole of the right half of the view (see the scene setup in Blender in Figure 5.4a on the next page). This established the start point of the camera track (see the rendered image in Figure 5.4b). The camera was then moved parallel to the scene into a position such that the scene took up exactly the whole of the left half of the view. This established the last point of the camera track (see Figure 5.4c).

A linear track was then made between these two points, discretized such that N_{images} number of images was produced. These images are then cropped with a sliding window such that the new image has the same height, but half the width, resulting in a series of N_{images} images, all with the scene centered in each image (see Figure 5.4d and Figure 5.4e). Since these images need to be cropped, it is advantageous to be able to crop by an integer number of pixels to avoid the need for interpolation. This means that the sliding cropping window must move by an integer number, k , of pixels each time. Writing the cropped image width as W_{image} pixels, the uncropped image width is thus $2 W_{\text{image}}$. This gives us the restriction that $2 W_{\text{image}}/k \in \mathbb{N}^*$ and that it is equal to the number of images, N_{images} .

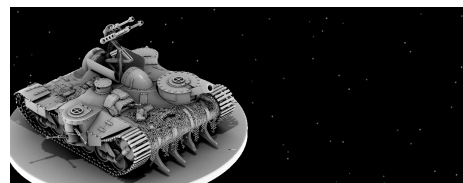
So the width of the uncropped images, $2 W_{\text{image}}$, must be some integer multiple of number of images rendered. The width of a rendered and cropped image,



(a) Setting up the scene in Blender



(b) Rendered left-hand side



(c) Rendered right-hand side



(d) Cropped left



(e) Cropped right

Figure 5.4: Rendered model images



Figure 5.5: Large rendered model image

in pixels, also corresponds to the width, in holopixels, of the final printed hologram. Likewise, the height of the rendered image corresponds to the height, in holopixels, of the final printed hologram.

A further restriction can be made from the LCOS resolution. Consider the holopixel at coordinate (x, y) being printed, with x and y in units of pixels. The LCOS must display an image such that the same (x, y) coordinate pixel from each image is mapped to a pixel on the LCOS. The solution can be simplified by imposing the restriction that the effective⁵ horizontal resolution of the LCOS is $W_{\text{lc}} = m N_{\text{images}}$ where $m \in \mathbb{N}^*$.

To summarize, the following restrictions were imposed in order to optimize the code:

$$N_{\text{images}} = \frac{2 W_{\text{image}}}{k} \quad (5.13)$$

$$N_{\text{images}} = \frac{W_{\text{lc}}}{m} \quad (5.14)$$

$$H_{\text{image}} = H_{\text{hologram}} \quad (5.15)$$

$$W_{\text{image}} = W_{\text{hologram}} \quad (5.16)$$

Where N_{images} is the number of rendered images, W_{image} and H_{image} are the width and height respectively of the cropped image, W_{lc} is the effective width of the LCOS, W_{hologram} and H_{hologram} are the effective width and height in pixels respectively of the hologram, and m and k are arbitrary non-zero natural numbers.

To print the test model for the purpose of evaluating the printer, a holopixel size of approximately 0.3 mm was used. A resolution of 0.3 mm between pixel centers is approximately 85 Dots Per Inch (DPI), similar to that of the resolution of a computer screen. To aid in the visual evaluation of the completed hologram, however, the distance between the pixels was increased to 0.5 mm, leaving a gap between each pixel (See Figure 5.7 on page 111).

⁵Sometimes it is advantageous to only use a portion of the LCOS screen, hence the prepended qualifier 'effective'.

The hologram was printed on a large Slavich VRP-M glass plate of dimensions 60 cm×40 cm in landscape. With a 0.5 mm inter-pixel spacing, the maximum width and height of the hologram in pixels is thus:

$$W_{\text{hologram}} \leq 60 \text{ cm} \div 0.5 \text{ mm/pixel} = 1200 \text{ pixels} \quad (5.17)$$

$$H_{\text{hologram}} \leq 40 \text{ cm} \div 0.5 \text{ mm/pixel} \approx 800 \text{ pixels} \quad (5.18)$$

For the Brilliant LCOS BR1080HC display system with a resolution of 1280×768 used in landscape format, $W_{\text{lc}} = 1280$. To produce a slightly brighter hologram, the hologram replay viewing window was reduced by reducing the effective width of the LCOS to 984 pixels. This particular size was chosen to allow the image size to be nice resolution.

Rearranging Equation (5.13) and Equation (5.14) on the previous page:

$$W_{\text{image}} = \frac{k}{2m} W_{\text{lc}} \quad (5.19)$$

Setting $m = 2$ & $k = 5$:

$$1230 = \frac{5}{4} \times 984 \quad (5.20)$$

$$N_{\text{images}} = \frac{2 \times 1230}{5} = 492 \quad (5.21)$$

An image height of 960 was chosen. 492 images were thus rendered at 2460×960 and cropped to 1230×960 using the program listed in Appendix A.

A single rendering of the test model at this resolution took approximately five hours to do on a single CPU PC. Extrapolating, this would take a total rendering time of 1280×5 hours = 1 month. To reduce this time, the rendering farm company ResPower was used, completing the render in just under 24 hours. If maximum resolution and maximum depth was used instead, the rendering would have taken an estimated 1.5 years of rendering time - around a week on the ResPower rendering farm.

5.9 Analysis

After several attempts, a successful bright hologram was produced. With just over a million pixels, the hologram took around 11 hours to print at rate of 30 pixels per second. This speed was experimentally pushed up to 42 pixels per second for smaller holograms without noticeable problems.

To protect and display the hologram, the hologram was printed back to front and then the emulsion side spray-painted black. A few different brands of spray paint were tested to find one that not harm the emulsion. The best performing paint was a cheap quick-dry car matt-black spray-paint. This caused the hologram to color shift slightly, but had no noticeable adverse affect on the brightness.

Figure 5.6 on the following page shows a photograph of the final hologram. This was taken with a 0.625 second exposure and a $f/4.2$ aperture. The ghost-like artifacts are due to reflections from the glass, and are not prominent when viewed by eye.

A single attempt was made to try to print with an inter-pixel size of 0.28 mm. This produced a dim hologram that is visible to the eye but too dim to photograph with a standard digital camera. This failure was most likely due to a bad alignment of the object and reference beams on the holographic emulsion, and further experimentation is required.

Figure 5.7 on page 111 shows an enlarged portion of the hologram. Notice that the pixels are perfectly aligned in both axes (The tilt of the y-axis is just due to the angle of the hologram when the photograph was taken. The axes are orthogonal.) The spacing between the pixels has been left slightly larger than the actual pixel size (Approximately 0.5 mm spacing) to make such analysis of the final hologram easier.

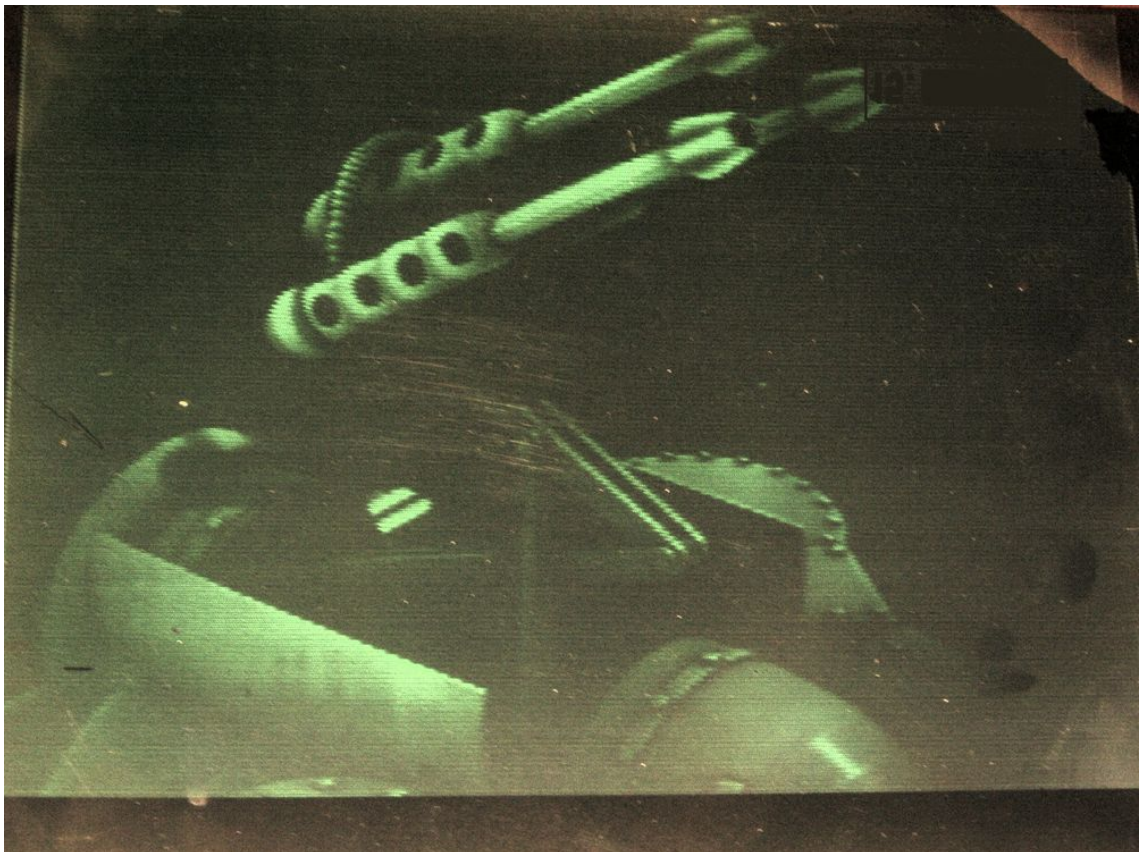


Figure 5.6: High resolution (0.3 mm in diameter pixels) hologram of futuristic tank. Some of the low contrast and low detail are due to the difficulty in capturing the image with the camera.

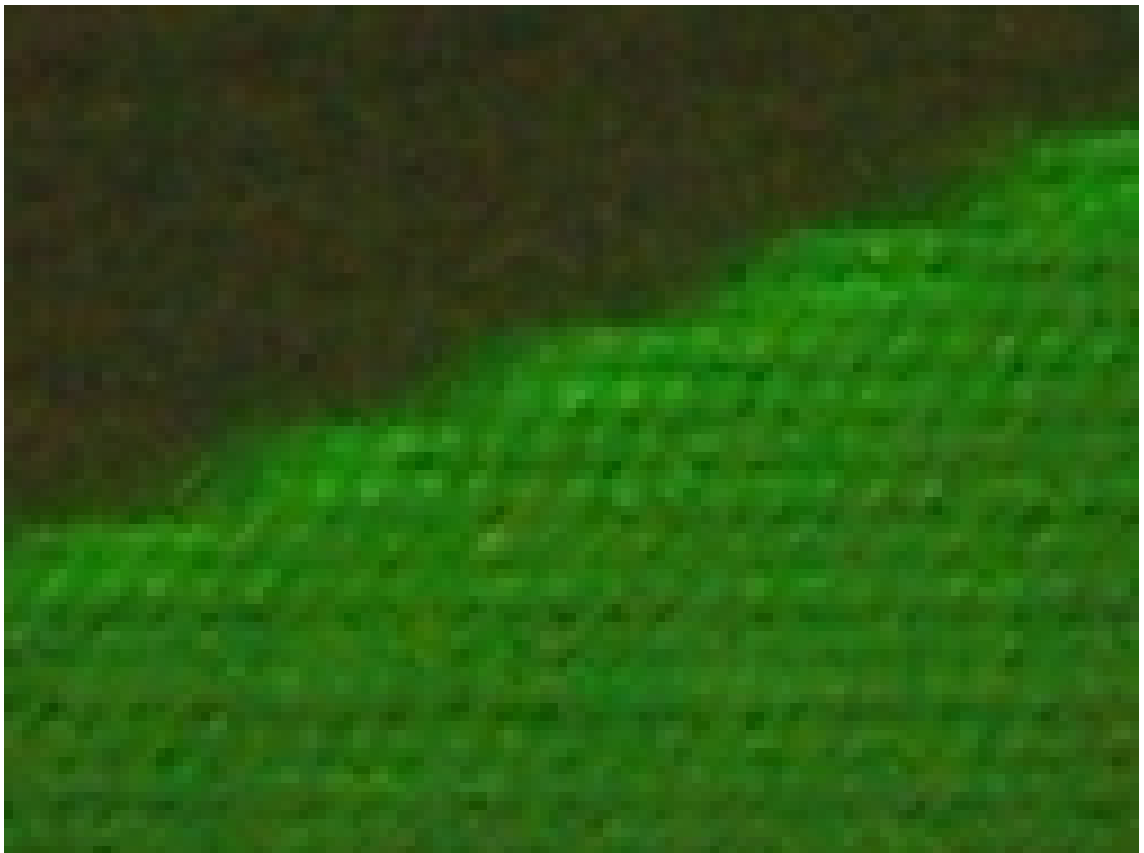


Figure 5.7: Zoomed in on a small section of the high resolution hologram. Blurriness and artifacts are due to the difficulty in capturing the image with the camera.

5.10 Summary

Various printing speed and resolution improvements to the digital direct-write monochromatic hologram printer described in Chapter 3 were investigated and implemented. The printing speed was successfully increased from 4 holopixels per second to 40 holopixels per second through a variety of software and mechanical improvements along with a newer design of a laser power supply. The printing resolution of holopixels was increased, with the holopixel diameter reduced from 1.0 mm to 0.3 mm - a factor of ten increase in resolution. The rendering of the input images was also discussed along with the restrictions required for optimal holograms.

It was found that achieving the required high precision timing on a normal PC for printing at 40 holopixels per second is possible but that further improvement to printing speed would require a realtime operating system with high performance hardware timers.

A demonstration of the final results is given in Figure 5.4a on page 105.

6

Temperature-energy feedback

This chapter details the custom energy meter and heating system that was built to improve the pulse to pulse laser energy stability by reducing laser mode beating. A computer controlled heating system was created for adjusting the position of the laser cavity rear mirror and was driven by a temperature-energy feedback algorithm. The heating system was additionally used for maintaining a constant temperature within the laser, to further help with stability. The effectiveness of these improvements is determined.

6.1 Problems with laser instability

The particular laser investigated for use in the hologram printer is an infrared 1064 nm passively Q-switched long-cavity pulsed laser. The fundamental beam has a frequency of 1064 nm beam which is frequency doubled to 532 nm (visible green). The laser produces up to 50 pulses a second, each with 50 ns pulse width,

6.1. PROBLEMS WITH LASER INSTABILITY

and has a single TEM₀₀ beam mode. The full technical specifications are given in Appendix H.

The pulse energy was found to be unstable with between a 10% to 30% pulse-to-pulse standard deviation in energy. This produces noticeable defects in the replay of the printed hologram (as seen in Figure 3.19 on page 68), as the pixels are printed with different energy densities. This in turn affects the hologram because the maximum diffraction efficiency of the final developed hologram is a function of the incident energy density [78]. The exact nature of this function varies between emulsions, but typically has a peak diffraction efficiency at some particular energy density with a gradual decrease in diffraction efficiency with increasing energy density, as shown in Figure 6.1 on the following page. The energy stability required from the hologram printer laser is thus dependant on the slope of this curve. By inspection of the relationship between energy density and diffraction efficiency, and from experience of printing holograms, we found that for the Slavich monochromatic emulsion Slavich VRP-M and the panchromatic Slavich PFG-03C, a pulse-to-pulse standard deviation of less than 10% is not noticeable under normal viewing conditions.

It is worth mentioning that the contrast of the image is related to the interference term which relies on the relative intensities of the reference and object beams. Since the two beams originate from the same laser source, the relative intensities remain unaffected by laser instability.

The pulse-to-pulse standard deviation changes due to uncontrolled changes to optical length of the laser resonance cavity due to temperature fluctuations, changes in moisture, etc[79]. The laser is designed to be locked to a certain mode by the combination use of a thin and thick etalon. However if the cavity optical length changes sufficiently, a second mode frequency can be selected. If multiple mode frequencies can coexist in the resonance cavity, they compete, producing mode beating which causes a drop in the beam intensity. It is this drop in the beam intensity that can cause some pixels on the final hologram image to appear

6.1. PROBLEMS WITH LASER INSTABILITY

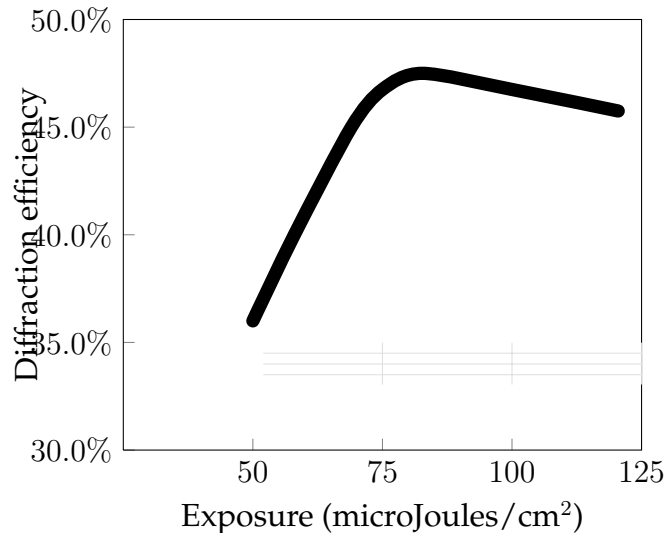


Figure 6.1: Diffraction efficiency curve for Slavich VRP-M monochromatic emulsion suitable for holography at 532 nm (Data source: [64]). Diffraction efficiency curves for other emulsions are similar[64, 78].

much dimmer than others in replay. Severe mode beating can often be observed to the naked eye as an occasional flickering of the beam.

We have argued for the need for improved energy stability in order to produce high quality holograms, and that the reason that the laser is unstable is because it uses a long resonance cavity that can change its effective optical size due to temperature, moisture, etc. fluctuations.

This was approached on two fronts. The first was to try to limit the temperature fluctuations. The laser was enclosed in a case with a heated breadboard. The breadboard was heated with a temperature feedback system that continually measures and heats the breadboard to maintain a stable temperature.

The second step is to have an active way to adjust the cavity length size. By implementing a system that can change the physical cavity length, we can counter changing air densities, and other changes, in an attempt to keep the optical cavity length constant.

To achieve this, the rear mirror of the cavity was mounted onto one end of a metal block. The other end was mounted in a holder for mounting in the laser. Two resistors were affixed to the metal block to provide the ability to heat the block, along with a thermiresistor to measure the temperature of the block. When

6.2. CUSTOM ENERGY METER

the metal block is heated the block expands, adjusting the position of the rear mirror. In this way the position of the rear mirror can be adjusted to high precision (see Equation (6.2)) to compensate for uncontrolled resonance length variations.

Aluminum was chosen for the material of the metal block. Aluminum has a coefficient of linear thermal expansion of $23 \times 10^{-6} \text{ K}^{-1}$. As we will see, the temperature of the block can be controlled to within an accuracy of $0.01 \text{ }^\circ\text{C}$. For an aluminum block of length 1.5 cm , the thermal expansion for a change in temperature of $0.01 \text{ }^\circ\text{C}$ is:

$$\Delta L = 1.5 \times 10^{-3} \text{ m} \times 23 \times 10^{-6} \text{ K}^{-1} \times 0.01 \text{ K} \quad (6.1)$$

$$\approx 0.35 \text{ nm} \quad (6.2)$$

This is of sufficient accuracy for a fundamental mode of 1064 nm .

Rather than attempting to determine the optical cavity length at any given time, in order to compensate for its changes, the energy can be measured instead and used as the basis for adjusting the position of the rear mirror. A feedback system was implemented to monitor the beam energy. If temperature/moisture/etc fluctuations cause the optical cavity length to change, the beam energy changes, and the feedback system can adjust the position of the rear block to compensate.

Both the energy-feedback system and the breadboard heating system require a heating and monitoring component, with its own feedback system, to heat to a given temperature. The same system was used for both of these needs, and will be hereby referred to as the Digital Temperature Controller (DTC).

6.2 Custom energy meter

To control the energy stability, a computerized system is required to measure the energy in each beam pulse. For this task, a custom energy meter was built. Although off-the-shelf energy meters exist, a simple and cost effective device was

6.2. CUSTOM ENERGY METER

required that worked at low energies (of the order of micro Joules). Since it was to be fixed in place and communicate only to a computer, a display etc was not required. Since the energy stability is the key piece of information that is required, overly accurate calibration and preciseness was also not required.

A general overview of the custom energy meter is discussed below, followed by a discussion of methods for diverting the energy beam into the custom energy meter. Next the calibration of energy meter is explained, concluding with a comparison of energy readings with an off-the-shelf energy meter from the company Ophir.

6.2.1 Overview of custom energy meter

A small portion of the beam to be measured is diverted onto the surface of an awaiting photodiode. The 50 ns laser pulse used is too short to measure directly, so current from the photodiode is collected onto the plates of a capacitor. The capacitor is then allowed to leak to ground through a resistor. The capacitor leaks in a consistent way, with the voltage across it following a very specific profile which is determined by the initial charge collected. By using an Analogue-Digital (A-D) converter to measure the voltage across the capacitor with time and timing how long it takes for the capacitor to discharge, the initial collected energy can be deduced. From that, with calibration, we can deduce the energy that was in the incident laser pulse.

6.2.2 Methods for diverting beam

Since the feedback system needs to be working continually, a real-time monitoring system needs to be put in place; blocking the beam in order to measure its energy is clearly not desirable. As stated before, the laser has a fundamental frequency of 1064 nm which is frequency doubled to 532 nm. Either of these are suitable for monitoring the energy, but the visible second-harmonic (532 nm) is

6.2. CUSTOM ENERGY METER

the more obvious candidate. There are various methods for diverting a small amount of the beam in order to measure the energy. Two different approaches were evaluated. The first approach tried was to measure the back leakage from one of the various 90° reflective mirrors used (Figure 6.2a).

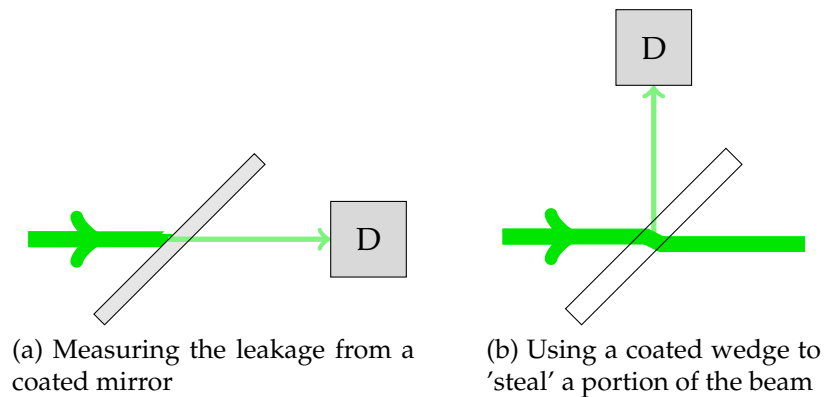


Figure 6.2: Two possible layouts to deflect energy to the detector, D.

The mirrors, although coated, are not 100% perfect – a small amount of the beam energy transmits ('leaks') through the mirror and would be normally discarded.

The second approach tried used a thin glass wedge coated on one side, placed in the beam. The wedge reflects around 3% of the beam energy to the waiting photo-diode (Figure 6.2b) ¹.

The second approach used a thin glass wedge two glass right-angled coated wedges, placed next to each other in the beam. The wedge reflects around 3% of the beam energy to the waiting photo-diode (Figure 6.2b).

The calibration of the energy meter is discussed later, but the results regarding the method for deflection are mentioned here, for the sake of continuity.

The first method was found to give unreliable results. The percentage of leakage through the mirror was not predictable with time. This can be demonstrated by a plot of the energy readings taken from the off-the-shelf pre-calibrated Ophir meter and comparing them against the readings from the custom energy detec-

¹In practice, two right-angled coated wedges were used, with one rotated by 180°, to act as a single wedge.

tor. There should be a one-to-one mapping between the two sets of readings with some small margin of error. Instead there appears to be two distinct clusters, as can be seen in Figure 6.3².

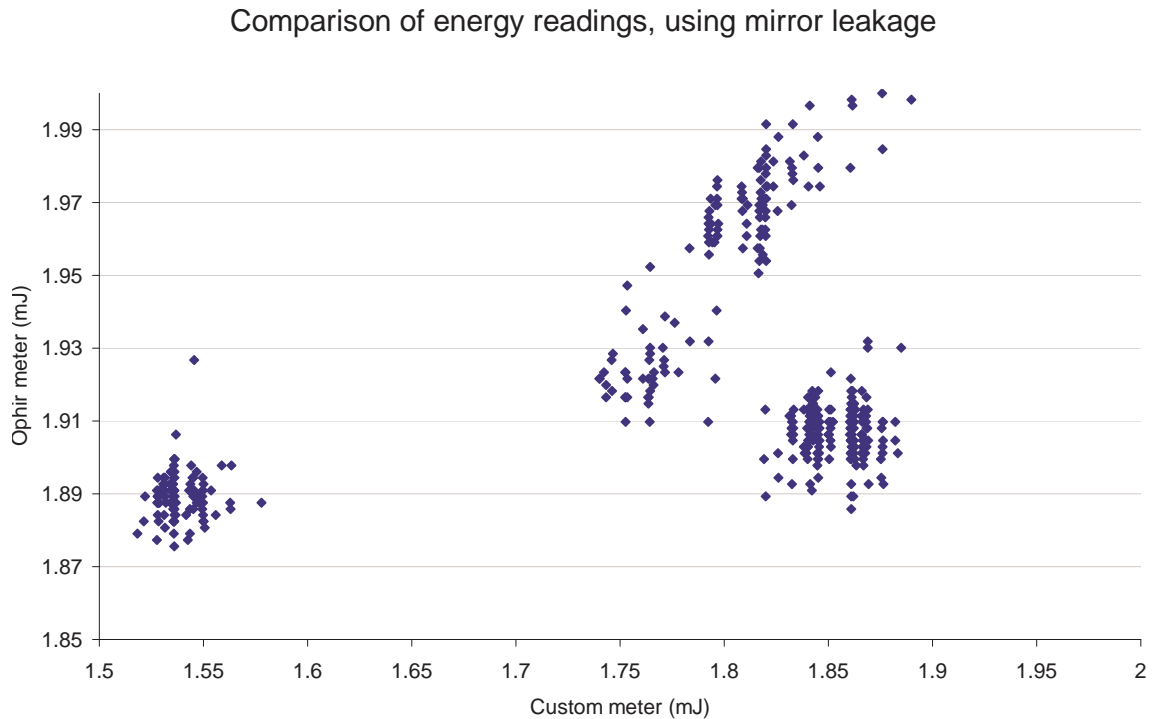


Figure 6.3: Comparison of energy readings from the Ophir energy meter and the custom energy meter, obtained for mirror-leakage.

The second method, to use a thin coated wedge, was found to give more reliable results. Testing shows a strong, and time-constant, correlation between the energy reading given by the custom energy meter and the energy reading given by the Ophir energy meter. All future graphs and values are given for this second method, unless otherwise noted.

6.2.3 Calibrating custom energy meter

The 50 ns laser pulse used is too short to measure directly, so current from the photodiode is collected onto the plates of a capacitor. The capacitor is then allowed to leak to ground through a resistor. The capacitor leaks in a consistent way, following a very specific profile which is determined by the initial charge

²Note that the scale for the readings from the custom energy meter are somewhat arbitrary, given that no sensible calibration can be obtained

6.2. CUSTOM ENERGY METER

collected. By using an A-D converter to measure the voltage across the capacitor with time and timing how long it takes for the capacitor to discharge, the initial collected energy can be deduced. From that, with calibration, we can deduce the energy that was in the incident laser pulse.

To calibrate the photo-detector, an off-the-shelf calibrated energy meter was placed in the optical path of the 532 nm beam and the beam energy adjusted to calibrate and check the photo-detector software. The energy meter triggers sending the voltage reading data to the PC when the voltage suddenly spikes – i.e. at the start of a pulse. The first few readings saturate the A-D converter and just return the maximum value – 4096. Then as the voltage drops we measure the decay curve. Two example pulses with different energies are shown in Figure 6.4.

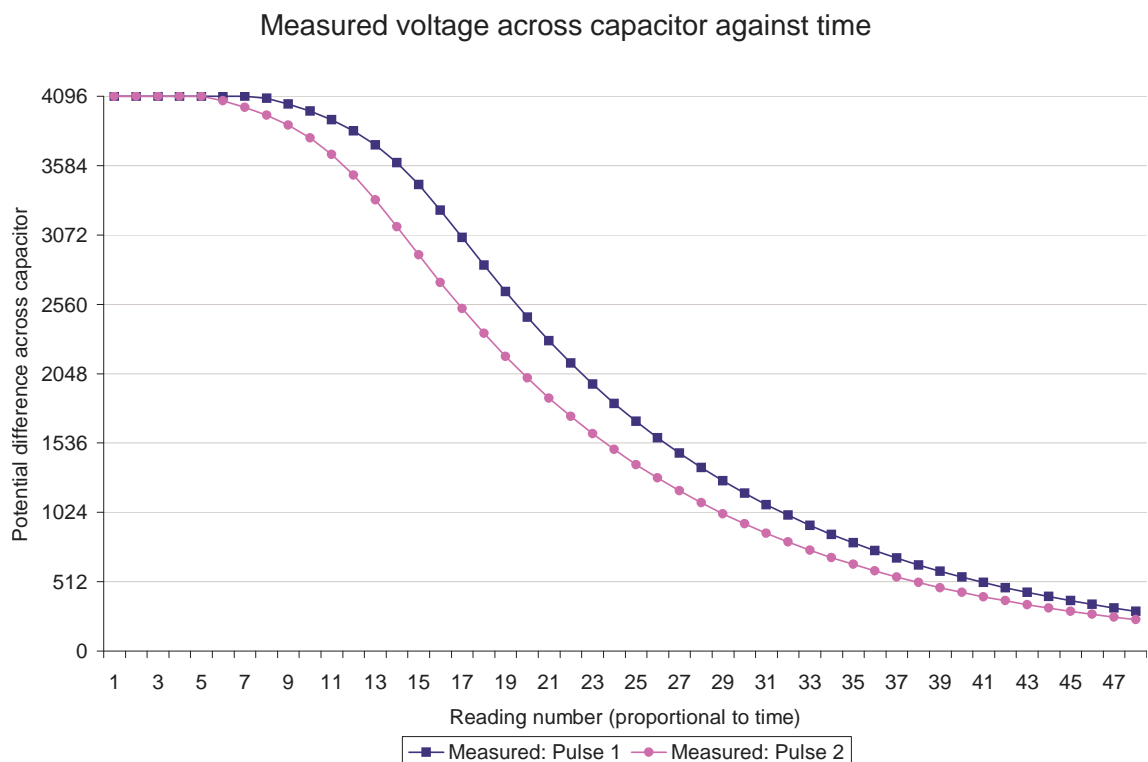


Figure 6.4: Measured voltage across the energy meter’s capacitor against time, after a pulse (Arbitrary units)

To determine the energy from this curve, the values between 2400 and 1000 were considered only.

The potential difference across the capacitor curve follows a characteristic ca-

capacitor decay curve of:

$$V_t = V_0 e^{-t/RC} \quad (6.3)$$

The energy in capacitor is related to the potential difference across the capacitor by the equation:

$$E = \frac{1}{2} CV^2 \quad (6.4)$$

So indicating initial energy as E_0 we obtain:

$$V_t = \sqrt{\frac{2E_0}{C}} e^{-t/RC} \quad (6.5)$$

Using variable substitution of $A = \frac{2}{C}$ and $k = \frac{2}{RC}$:

$$V_t = \sqrt{AE_0} e^{-kt/2} \quad (6.6)$$

By using the data measured for the voltage across the capacitor after a single pulse and setting E_0 to one we can use the least squares algorithm to determine the best fitting A and k constants. Repeating this process for many pulses, different values A will be obtained, but the k values will be very similar. The average value of k thus determines the calibration k constant. An arbitrary value for A can be chosen as A simply sets the calibration scale of the energy. After calibration, we obtain a fit as shown in Figure 6.5 on the next page.

With the now determined values of A and k in hand, it is useful to rearrange the Equation (6.6) to obtain the energy in the pulse in terms of the measured potential differences, as so:

$$E_0 = V_t^2 \cdot A^{-1} e^{kt} \quad (6.7)$$

So using the measured values for the voltage across the capacitor, V_t , and our determined values for k and A , the initial energy (measured on some arbitrary scale) of the pulse, E_0 , can be found.

An estimate for the energy for any pulse can now be determined. Using an

Measured and theoretical voltage across capacitor

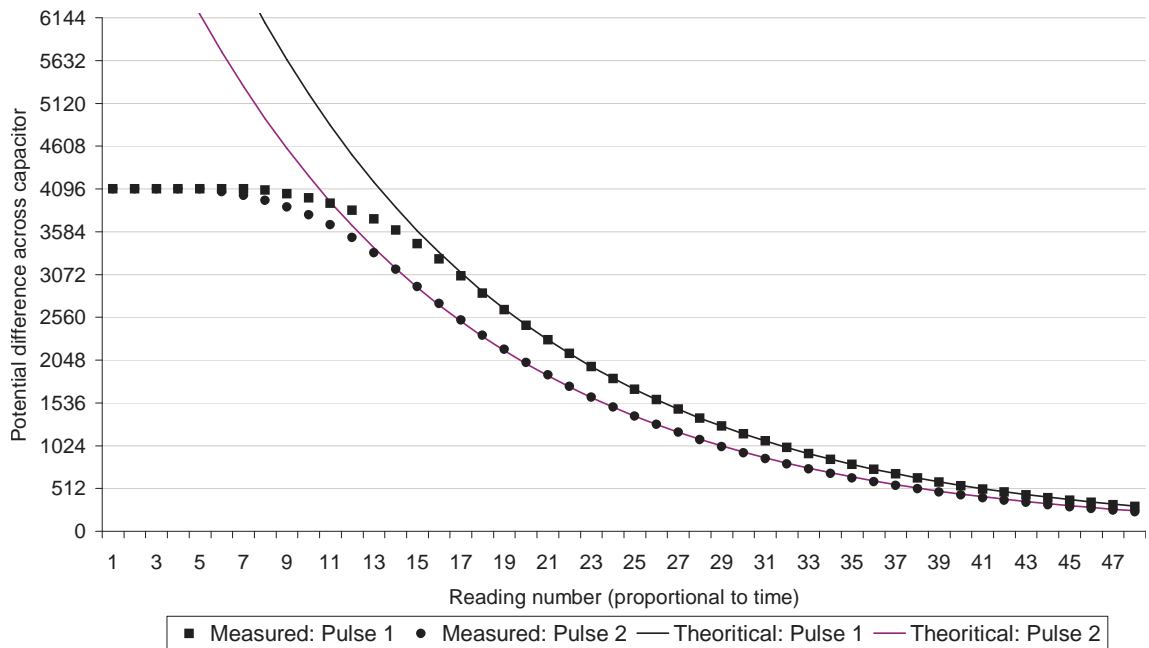


Figure 6.5: Measured and theoretical voltage curve of capacitor for energy meter

energy meter that has already been calibrated, the value of A can be determined such that our energy is measured in Joules.

A comparison of the energy measured by this device against the energy measured by an off-the-shelf energy meter by the company Ophir is given in Figure 6.6 on the next page. For this graph the photodiode was using the energy leakage from a mirror. The two graphs do not fit perfectly, although it is adequate for the energy-temperature feedback system.

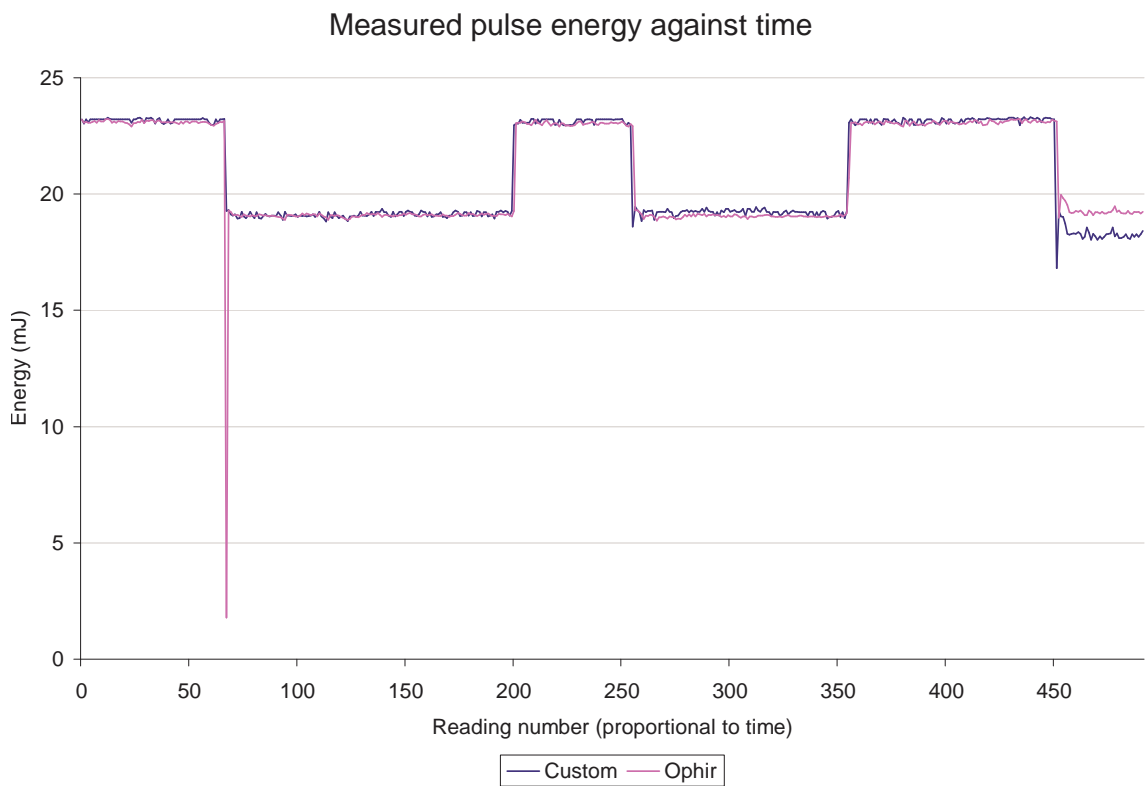


Figure 6.6: Comparison of energy meter and the Ophir energy meter measuring energy against time

6.3 Digital temperature controller

As mentioned previously, two resistors were affixed to a metal block that holds the rear mirror, along with a thermiresistor to measure the temperature of the block. To control these components, the PIC18F876A microprocessor was used. This microprocessor contains 8k x 14-bit internal non-volatile EEPROM memory, and a 20MHz clock.

These hardware components are mounted on a small custom made controller Printed Circuit Board (PCB) board as shown in Figure 6.7. Several of these DTC boards were mounted on the underside of the laser breadboard as well to carefully control the temperature of the breadboard and components on it. The PCB board, named the DTC, communicates via the serial communications protocol RS485.

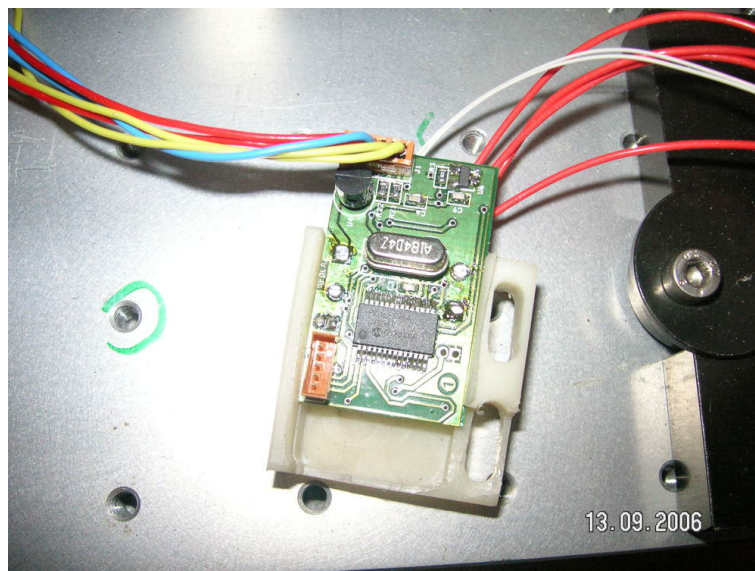


Figure 6.7: Photograph of the final DTC board. The two white wires on the right lead to the thermiresistor, the four red wires on the right lead to a pair of resistors for heating, and the rest of the wires on the left provide power and communication lines to the PC.

6.4 Temperature feedback algorithm

The Digital Temperature Controller has one input (the current measured temperature) and one output (whether to heat or not). There is a time delay between switching on the heating and the new temperature registering on the thermometers. This is because it takes time for the resistors to heat up and time for the heat to be conducted through the material. This means that if we simply heat until we measure the required temperature and then switch off the heating, we will find that the measured temperature continues to climb, overshooting the target temperature. If we are too cautious in heating then we risk taking a much longer time to heat than necessary.

This can be solved by using a **Proportional Integral Derivative (PID)** controller algorithm [80]. This is a general purpose control-loop feedback algorithm that is widely used in industrial control systems.

The PID controller attempts to correct the error between a measured input variable (the temperature) and a desired target (the temperature we want to heat to) by calculating and then outputting a corrective action that can adjust the process accordingly (by heating).

There are 3 steps to this algorithm.

The first step is a **Proportional** response that changes the output proportionally to the current temperature error. The constant of proportionality is labelled K_p .

The second step is an **Integral** response that changes the output based on the accumulated instantaneous temperature readings over time. The integral gain constant is labelled K_i .

The final step is a **Differential** response that changes the output proportionally to the rate of change of the temperature error. The differential gain constant is labelled K_d .

6.4. TEMPERATURE FEEDBACK ALGORITHM

Using a fairly standard adaptation, the integral response was changed to limit the time period over which the integral is done. This is omitted from the pseudo code for sake of clarity.

This algorithm was implemented in the computer language C and run on the Digital Temperature Controller boards. The pseudo code is shown in Algorithm 2.

```
1  $\Delta T_0 = 0;$ 
2  $t = 1;$ 
3 repeat
4    $\Delta T_t = T^{\text{Target}} - T_t;$ 
5    $P_t = Kp \cdot \Delta T_t;$ 
6    $I_t = I_{t-1} + Ki \cdot \Delta T_t \cdot \Delta t;$ 
7    $D_t = Kd \cdot \Delta T_t - \Delta T_{t-1} / \Delta t;$ 
8   output =  $P_t + I_t + D_t;$ 
9   heat output;
10  wait for time  $\Delta t;$ 
11   $t = t + 1;$ 
12 until finished ;
```

Algorithm 2: Digital Temperature Controller feedback using PID algorithm

Calibration of the parameters Kp , Ki and Kd was done manually. They are dependant upon many factors – mechanical setup, size of the mechanical blocks, thermal insulation, heating resistor used, etc. The resistors were tested against various target temperature functions and the optimal set of parameters chosen. The time period across which to integrate was limited to the previous 32 seconds.

The final values decided on were:

$$\begin{aligned} Kp &= 0.7 \\ Ki &= 0.02 \\ Kd &= 0.7 \end{aligned} \tag{6.8}$$

This results in the fit shown in Figure 6.6 on page 123.

6.5 Temperature feedback system on rear mirror

As mentioned before, the rear mirror in the laser cavity was mounted on one end of a metal block whose other end is mounted in a holder. One of these DTC boards was used to control the temperature of this rear mirror metal block.

This gives a response such as that shown in Figure 6.8 on the following page. The light gray line indicates the target temperature, T^{Target} , as a function of time. The black line shows the measured temperature T_t as a function of time. To increase the temperature, the system responds rapidly. It takes approximately 20 seconds to increase the temperature by 4 °C. Cooling down requires simply waiting for the excess heat to be carried away, requiring about one and a half minutes to decrease the temperature by 4 °C.

Such large temperature changes are not, however, useful to us for any normal operation. It is shown simply to check the behavior of the system.

We can use the same temperature system to control the temperature of the bread board.

Figure 6.9 on the next page shows the same system working for heating the breadboard. The target temperature is set here at 33 °C, and kept constant. This shows that there was a large source of noise arising from somewhere, but despite the noise the feedback system still managed to cope exceptionally well. After fixing the various noise problems, the temperature looks like that shown in Figure 6.10 on page 129. The standard deviation of the temperature is a lot better than it might appear from the graph – around 0.02%. For the holographic printer, the temperature of the breadboard is kept at 37.50 ± 0.02 °C.

6.5. TEMPERATURE FEEDBACK SYSTEM ON REAR MIRROR

Feedback reaction to extreme temperature changes

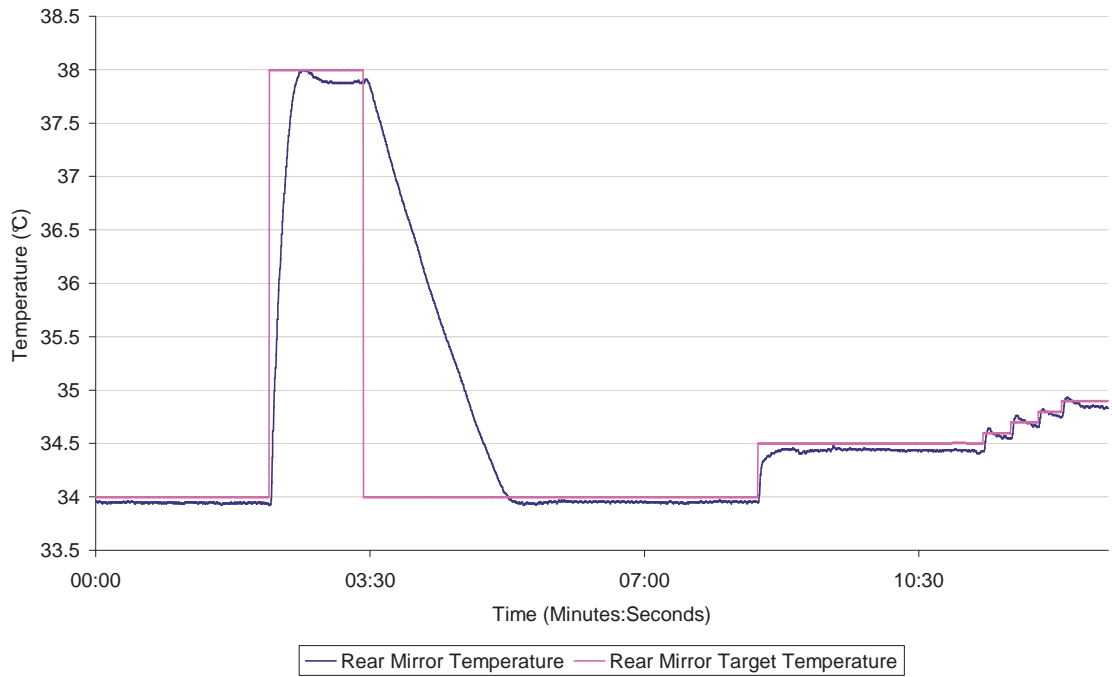


Figure 6.8: Digital Temperature Controller PID response to target temperature changes

Feedback reaction to noise in temperature readings

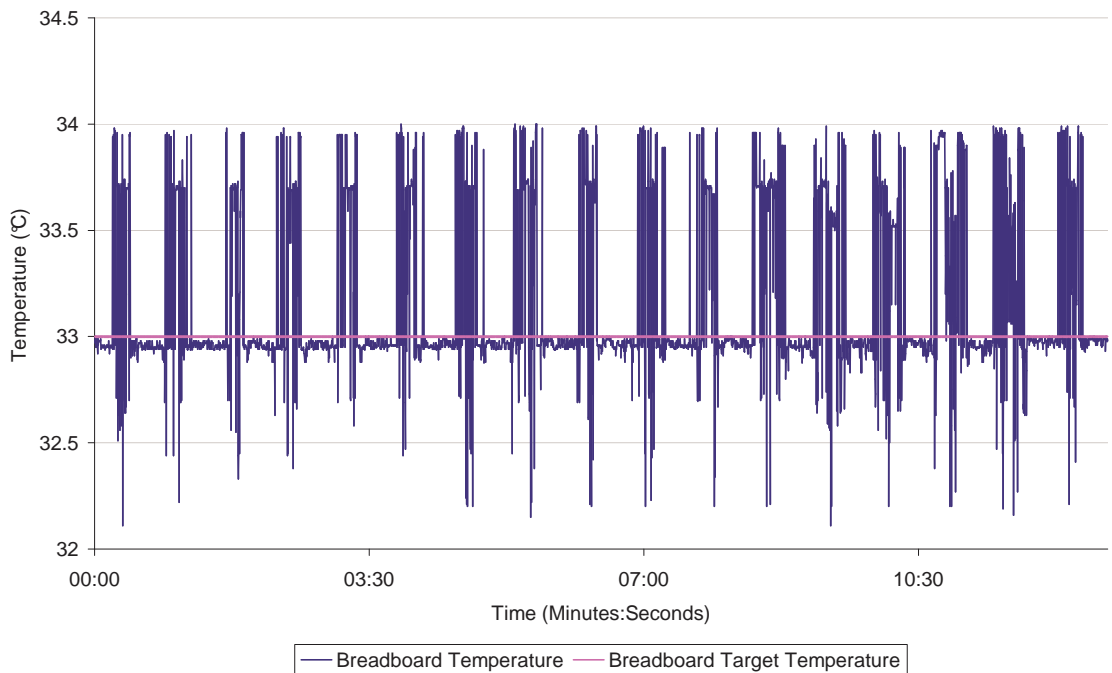


Figure 6.9: Digital Temperature Controller PID response to noise in temperature readings

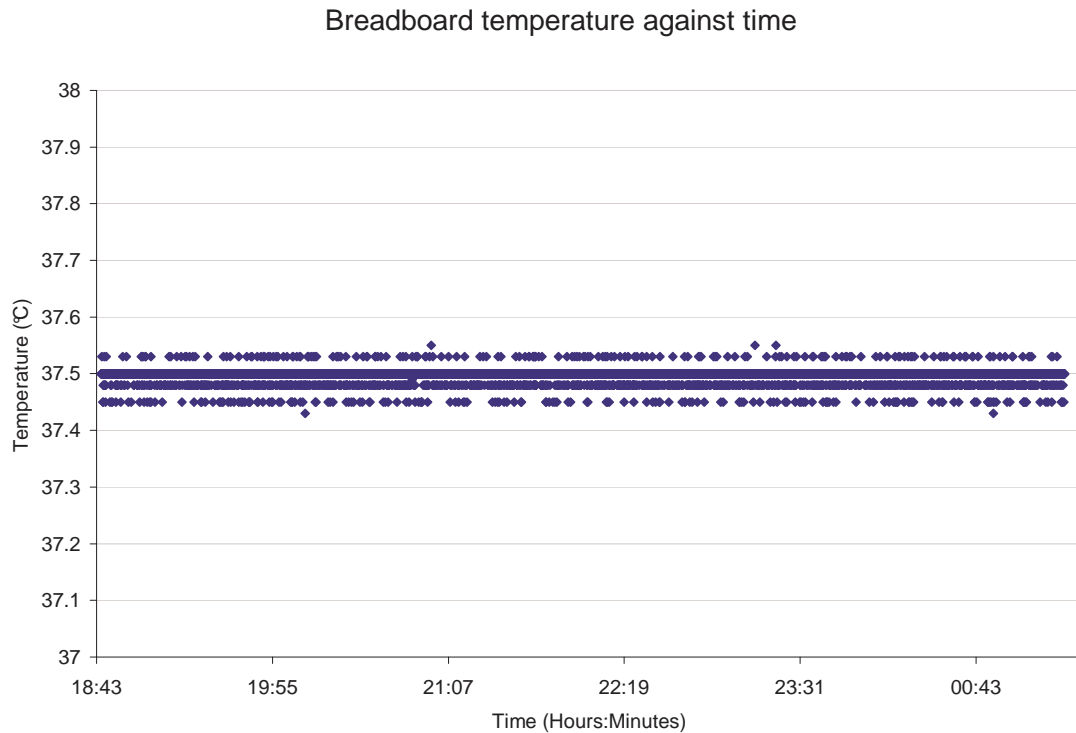


Figure 6.10: Breadboard temperature against time

6.6 DTC-PC communication

So now we have a way of maintaining a given temperature. The Digital Temperature Controller (DTC) board works independently to maintain the set target temperature. To set the target temperature, the DTC board talks to the computer via a serial communication protocol. The DTC boards use the RS485 serial protocol, produced by Electronics Industry Alliance (EIA). This protocol uses a voltage differential signal increasing its immunity against signal noise and suitable for a multi-point communications network. It also offers protection against data collision (multiple nodes accidentally talking simultaneously) and bus fault problems. The protection against signal noise is particularly important for the application of a DTC in a hologram printer because of the high voltage power supplies, flash lamps and other high voltage equipment that is present in the environment around the DTC communication wires.

RS485 also allows for multiple systems on a single wire. This allowed us to

6.6. DTC-PC COMMUNICATION

have multiple DTCs as well as other subsystems all connected via the same wires. For our purposes it was convenient to have all the data wires join together and feed into a USB-to-serial converter, and then plug the Universal Serial Bus (USB) converter into a PC.

For the higher level communication protocol, a custom protocol was developed. Each DTC, as well as other subsystems, were considered as separate nodes. Each node was given a unique number from 0 to 254. The node number 255 was reserved to indicate all nodes. Each node thus responded only to commands addressed to their own node number, or to the node number 255.

RS485 is half duplex and only allows one device to be talking at a time – to prevent cross talk. The protocol is robust enough to recover from accidentally cross talk.

To make the protocol simple, the PC acted as a master, and the nodes act as slaves – only communicating in reply to a message. At start up, the PC can send a ‘ping’ message to each node identification number (ID) number in turn. If a node sees a ping message with its ID on it, it replies. If there is no reply within some timeout period then the PC knows that there is no node connected with that ID. In this way the PC can ‘scan’ the bus looking for devices.

Every second, or so, the PC sends a message to the first device that it knows is connected asking for the current temperature. It then waits for a reply (or a timeout in case of an error) before asking the next device for its current temperature.

In this fashion the PC can be kept updated about the current temperatures of all the parts of the laser. At any time the PC can send a message to set the temperature.

To set a node ID on a DTC or to reprogram a node, a single node must be connected to the computer by itself. Then the node ID 255 can be used to communicate to it and to reprogram it.

6.7 Temperature-energy feedback

We now have the components required to measure the current beam energy and to adjust the cavity length by heating and thus expanding a small block that the rear mirror is attached to.

The aim now is to adjust the rear mirror as needed in order to try to maximise the beam energy and minimize the point-to-point standard deviation of the beam energy.

To first get a qualitative feel for how the energy depends on the cavity length, a temperature scan was performed. This changes the temperature of the metal that the rear mirror is mounted on, and hence changes the cavity size. The first attempt of an energy scan was run for just over twenty hours, with the results shown in Figure 6.11.

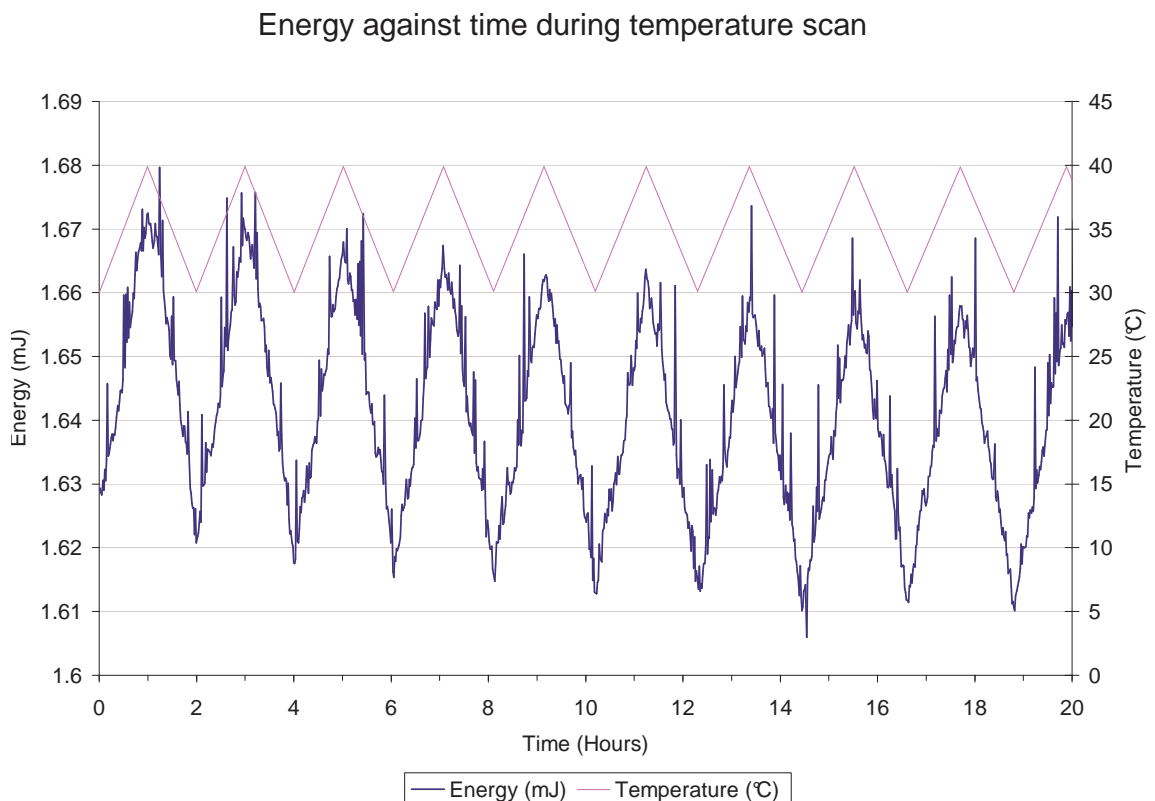


Figure 6.11: Energy against time in rear mirror position scan over 20 hours

This shows that something has gone wrong. The energy increases with the temperature (and hence shortening of the cavity) to within the limits of the heat-

6.7. TEMPERATURE-ENERGY FEEDBACK

ing system. This means that the cavity is misaligned, and the rear mirror is far away from the optimal position.

To fix, the rear mirror temperature is set to a middle-of-the-range temperature. The laser was opened up and the rear mirror's position mechanically adjusted, using an energy meter to recalibrate it.

Despite this being a laser alignment mistake, we mention it here because this is a useful way to tell if the laser is correctly aligned.

To control the energy, we must control the rear mirror position, and thus the temperature of the block it is mounted on. However how can we know whether to heat or cool the block in order to increase the energy?

Initially a simple discrete algorithm was used to decide whether to heat or cool. It was heated initially, say, until the energy decreased. It then cooled (i.e. not heated), expecting that the energy would thus increase again. It continued to cool until the energy decreased again.

This was found to be too sensitive to point-to-point variations in the energy, even if some average was taken. It would oscillate between heating and cooling, getting stuck in local minima and responding to insignificant noise.

Instead, a more robust, but still discrete, algorithm based on that indicated in Figure 6.12 on the following page was used. This algorithm requires the energy to drop twice in succession in order to cause the temperature to change.

To improve the algorithm, the energy standard deviation was also looked at. As the standard deviation increases, so does the amount that the temperature is increased or decreased by. This increases its ability to get out of local minima. When the energy has dropped a lot and cavity is mode beating, the energy can become highly unstable, meaning that algorithm in Figure 6.12 on the next page can no longer work. By having a high standard deviation causing a large change in temperature, it allows us to 'jump out' of the bad mode beating region.

6.7. TEMPERATURE-ENERGY FEEDBACK

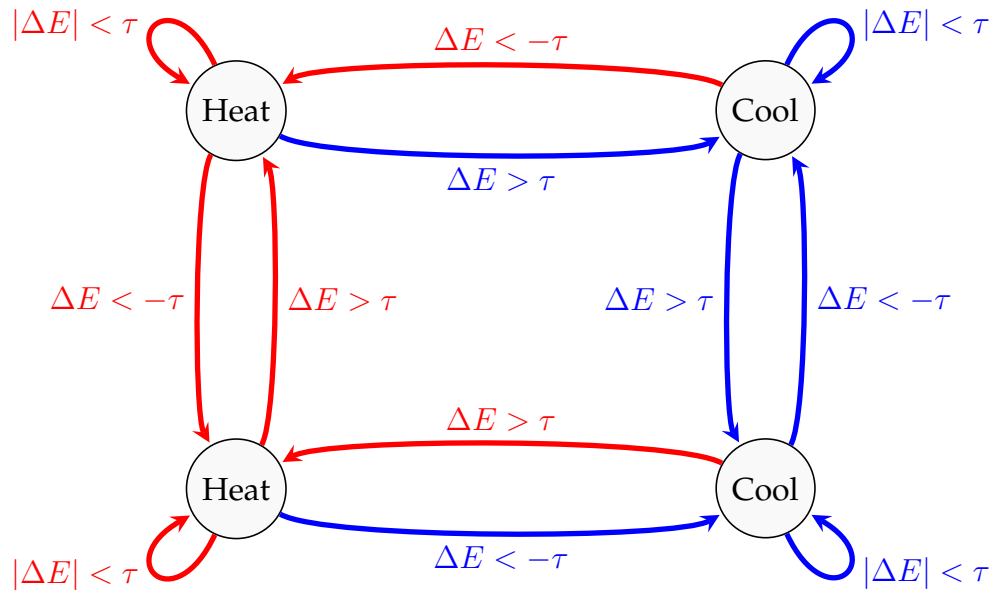


Figure 6.12: Energy temperature feedback algorithm for change of energy ΔE and threshold τ .

This algorithm was found to perform very well, as shown by Figure 6.13 on the following page. The point-to-point standard deviation remains less than 0.3 mJ (approx 3% of the beam energy) for the vast majority of the time, well within acceptable limits for hologram printing, as Figure 6.14 on the next page shows. The figure shows peaks of high standard deviation, but these were all below 10% standard deviation, producing no noticeable effects to the naked eye on the final hologram. Note that the square wave appearance of the beam energy is just due to a Neutral Density Filter being placed in the beam at arbitrary times, just to check that the beam energy is monitored over a range of energies and that no hysteresis effects are present. Also note that the graph indicates that Ophir meter has a glitch at around reading number 60 that was not picked up on the custom energy meter. The reason for this was not determined.

6.7. TEMPERATURE-ENERGY FEEDBACK

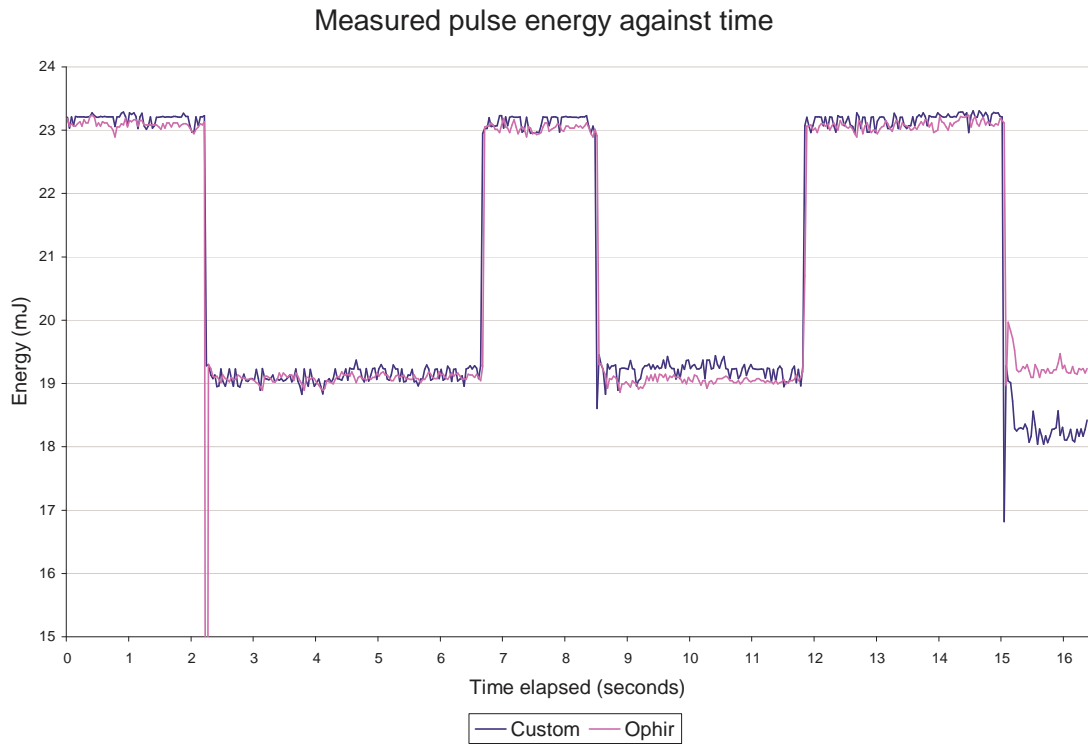


Figure 6.13: Second harmonic (532 nm) pulse energy with active feedback

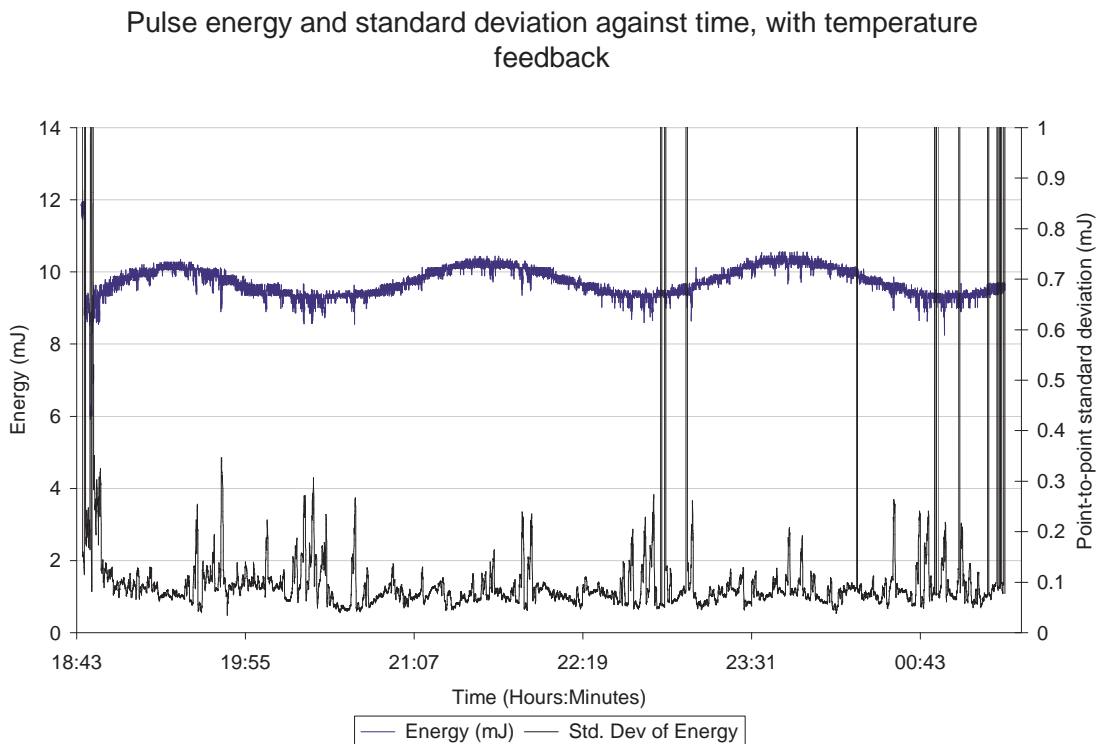


Figure 6.14: Second harmonic (532 nm) pulse energy with active feedback showing standard deviation

6.8 Summary

Instability in the laser energy output resulted in printed holograms having dim or missing pixels upon replay. A temperature control system was developed, and used to control the laser breadboard temperature. In addition, the temperature control system was used to adjust the position of the laser resonance cavity's rear mirror. This was coupled with an energy monitoring system and a PC to provide an active feedback system to stabilize the energy. Two different methods were investigated for diverting the beam energy into energy monitoring system, with the glass beam wedge being the resulting preferred method. The energy monitoring system was designed with the goal of being unobtrusive, cheap, and accurate enough for use in the feedback system. It succeeded at achieving all of these aims.

Using the active feedback for adjusting the position of the rear mirror based on the energy gave us a much more stable beam. The pulse-to-pulse standard deviation was reduced from over 10% to less than 3%, removing visual artifacts from the printed holograms. The Digital Temperature Controller was found to react fast enough for the requirements of a digital hologram printer, and performed satisfactory.

7

Conclusion and future work

7.1 Conclusion

This thesis researched and developed a direct-write pulse-laser hologram printer design suitable for recording white-light viewable reflection holograms in an off-axis geometry.

Chapter 3 examined the design of a one-step monochromatic hologram printer capable of producing white-light viewable transmission holograms created with the aid of an LCOS display system and printed in a dot-matrix sequence. The lens system was analyzed and documented in detail, with a particular focus on the microlens array system. The magnification of the object beam aperture due to the afocal telescopic reversing lens system, combined with an upstream microlens array system, was determined based upon a matrix method of lens analysis.

An optimal range of positions was analytically determined for each of the three rectangularly-packed microlens array of differing lenslet size and lenslet

7.1. CONCLUSION

curvature. While the overall fidelity of the hologram was demonstrated to be sensitive to the microlens array position, in their respective optimal positions there was no significant difference between the three different microlens arrays tested in terms of image fidelity, contrast and speckle. This implies that the contrast, diffraction efficiency and depth of view of the hologram's replay image will not be significantly affected by the choice in the microlens array employed, to within the range tested.

Chapter 4 analyzed the unwanted side effects of the angular intensity distribution of a hologram pixel, using a 'White Logo' hologram for case study. A visible 'ghosting' effect was demonstrated to be significantly reduced by applying a linear formula whose parameters were determined from either a grayscale image of the hologram or by considering each color channel (in RGB color space) separately. This correction can be applied as a pre-processing operation before printing holograms in order to reduce ghosting in the final image. Additionally, the artists can be warned when such effects may occur.

Chapter 5 examined methods for increasing both the printing speed and resolution of the hologram printer based upon increasing mechanical stability, improving hologram printer software, upgrading the laser power supply and using an improved display system. These improvements enabled the pixel size to be reduced from $1.0\text{ mm} \times 1.0\text{ mm}$ to $0.3\text{ mm} \times 0.3\text{ mm}$ and the printing speed to be increased from approximately 10 holopixels per second to approximately 42 holopixels per second.

Chapter 6 described the analysis and design of a temperature-energy feedback system to correct for pulsed laser instabilities arising from mode beating due to temperature variations. A small feedback heating system was used to control the optical length of the laser cavity with an accuracy of $\approx 0.35\text{ nm}$ by heating a metal block holding the rear cavity mirror. Combined with a custom-made energy meter and a feedback PID algorithm to adjust the temperature based on the energy stability, the pulse-to-pulse standard deviation was reduced from over 10% to less

7.1. CONCLUSION

than 3%. This improvement was shown to reduce visual artifacts from the printed holograms, improving their overall quality. The Digital Temperature Controller was found to react fast enough for the requirements of a digital hologram printer, and performed satisfactory.

7.1. CONCLUSION

Figure 7.1 and Figure 7.2 show a visual 'before and after' for the improvements to the digital hologram printer mentioned in this thesis. In particular note the occasional dim and missing pixels in the first hologram due to laser mode beating, and note the higher resolution of the second hologram.

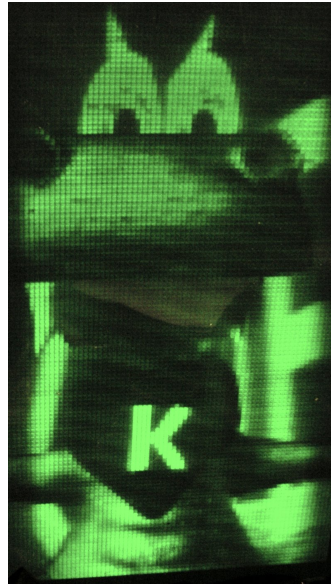


Figure 7.1: Photograph of green dragon hologram with $1\text{ mm} \times 1\text{ mm}$ pixels printed on the hologram printer before improvements, printed at 4 holopixels per second. A larger reproduction of photograph in Figure 3.19 on page 68.

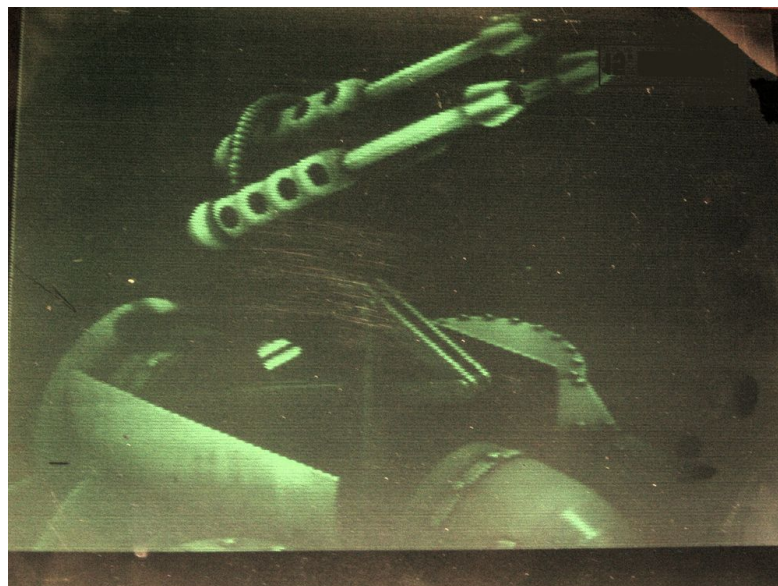


Figure 7.2: High resolution (0.3 mm in diameter pixels) hologram of futuristic tank, printed at 40 holopixels per second. Some of the low contrast and low detail are due to the difficulty in capturing the image with the camera. A larger reproduction of photograph in Figure 5.6 on page 110.

7.2 Future work

The increased resolution changes could be adopted on a hologram printer that uses an RGB laser source, such as the digital hologram printer by Rodin et al. [81]. Bjelkhagen and Mirlis [82] showed that while a minimum of three monochromatic colors are required for color holograms, four or more covers more of the color gamut observable by the human eye, allowing for more realistic colors to be reproduced.

For the beam illumination on the LCOS, Section 3.3 on page 30 assumed that an even spatial beam intensity profile would be preferable, in order to produce a replay viewing window with an even intensity. However non-even beam distributions, such as a Gaussian profile, could offer the advantage of having a brighter optimal replay angle at the sacrifice of dimmer non-optimal replay angles. This could also allow for a much larger replay window while keeping the image bright for viewers at some optimal angle (for example, at the normal to the hologram).

A modern laser printer typically prints at 600 DPI resolution. This translates to a pixel size of 0.04 mm in diameter. This makes for an interesting goal, requiring the holopixel to be reduced by an order of magnitude. This is an order of magnitude smaller than the high resolution holograms produced for this thesis. Achieving this would significantly increase the problems with beam alignment and printing speed. For an A4 sized hologram, approximately 35 million holopixels would need to be printed, requiring 8 days to print at 50 Hz.

The hologram printer could be adapted to print full parallax holograms, similar to the work done by Hrynkiw et al. [83], although this can introduce problems if printed in three or more colors. The printer could also be adapted to produce transmission holograms. This would require the reference beam to strike the hologram plate from the same side as the object beam. The only difficulty currently is that the objective and its mount block the path of the beam. This should be easily solvable, however.

7.2. FUTURE WORK

Making the printer physically smaller and more compact would be useful, ideally reducing the size down to the size of a typical office laser printer. This could possibly be achieved by using a pulsed laser diode, and by shrinking the afocal telescopic reversing lens system.

Building and maintaining the laser requires a high degree of patience and skill. It would be interesting to investigate an automatic alignment system of the mirrors and lenses, possibly based on piezoelectric actuators to provide between three to six degrees of freedom as required [84]. This could use the energy meter demonstrated with a feedback system to scan the parameter space for an optimal alignment, maximizing both beam energy and energy stability. Such a system, combined with automatic re-alignment as needed, could drastically reduce printer downtime and reduce the requirement for a full-time laser specialist.

The use of a diode pumped laser instead of a flash-lamp pumped laser could also increase reliability. This would reduce the continual maintenance requirement of replacing the flash lamp. Diode pumping could also drastically reduce the unwanted acoustic noise of the printer - by eliminating the noise produced by the flash lamp and by reducing the cooling requirements, allowing for a quieter but less powerful cooling system.

The temperature-energy feedback system used to compensate for laser cavity optical-length fluctuations worked by heating a metal block which thermally expanded, adjusting the position of the rear mirror. This approach was found to work well with a long cavity laser, but did not work well when extended to a short-cavity laser. Using a piezoelectric actuator instead would allow extension of the control scheme to a short-cavity laser.

On the software side, the rendered images could be preprocessed to correct for the 'ghosting' effect in holograms, using the parameters determined.

A more fundamental change would be to remove the reliance of wet processing. This could be achieved through the use of photopolymers or by direct abrasion or ablation of a material. This would truly open up the realization of an

office hologram printer.

Bibliography

- [1] Germain Chartier. *Introduction to Optics*. Springer, May 2005.
- [2] D. Gabor, G. W. Stroke, D. Brumm, A. FunkHouser, and A. Labeyrie. Reconstruction of Phase Objects by Holography. *Nature*, 208(5016):1159–1162, 1965.
- [3] D. Gabor. Holography, 1948-1971. *Science*, 177(4046):299–313, 1972.
- [4] D. Gabor and GW Stroke. The Theory of Deep Holograms. *Proceedings of the Royal Society of London. Series A, Mathematical and Physical Sciences*, 304(1478): 275–289, 1968.
- [5] H.F. Talbot. An account of some recent improvements in photography. 1841.
- [6] F.S. Archer. Collodion Process. *Notes and Queries*, (165):612–612, 1852.
- [7] Eastman et al. Photographic film, Oct 1884. US Patent 306,470.
- [8] PLP Dillon, AT Brault, JR Horak, E. Garcia, TW Martin, and WA Light. Integral color filter arrays for solid state imagers. *1976 International Electron Devices Meeting*, 22, 1976.
- [9] Jr. Thomas B. Greenslade. Wire diffraction gratings. *The Physics Teacher*, 42 (2):76–77, 2004.
- [10] D. Gabor et al. Theory of communication. *Institution of Electrical Engineering*, 93(4):29–4, 1946.
- [11] D. Gabor. System of photography and projection in relief, 1944. US Patent 2,351,032.

- [12] D. Gabor. Information theory in electron microscopy. *Lab Invest*, 14:801–7, 1965.
- [13] D. Gabor. Microscopy by Reconstructed Wave-Fronts. *Proceedings of the Royal Society of London. Series A, Mathematical and Physical Sciences*, 197(1051):454–487, 1949.
- [14] D. Gabor. A new microscopic principle. *Nature*, 161(4098):777–778, 1948.
- [15] D. Gabor. Progress in holography. *Reports on Progress in Physics*, 32(1):395–404, 1969.
- [16] D. Gabor. Three-dimensional picture projection, 1969. US Patent 3,479,111.
- [17] E.N. Leith and J. Upatnieks. New techniques in wavefront reconstruction. *J. Opt. Soc. Am*, 51:1469–1469, 1961.
- [18] TH Maiman. Stimulated optical radiation in ruby masers. *Nature*, 187(4736):493–494, 1960.
- [19] TH Maiman, RH Hoskins, IJ D’Haenens, CK Asawa, and V. Evtuhov. Stimulated Optical Emission in Fluorescent Solids. II. Spectroscopy and Stimulated Emission in Ruby. *Physical Review*, 123(4):1151–1157, 1961.
- [20] Emmett N. Leith and Juris Upatnieks. Reconstructed wavefronts and communication theory. *J. Opt. Soc. Am.*, 52(10):1123–1130, 1962.
- [21] E.N. Leith and J. Upatnieks. Wavefront reconstruction with diffused illumination and three-dimensional objects. *J. Opt. Soc. Am*, 54(11):1295–1301, 1964.
- [22] S.A. Benton. White light transmission/reflection holographic imaging. *Applications of Holography and Optical Data Processing*, Pergamon Press, Oxford, 1977.
- [23] SA Benton, HS Mingace Jr, and WR Walter. One-step white-light transmission holography. *Recent advances in holography; Proceedings of the Seminar, Los Angeles, Calif., February 4, 5, 1980.(A81-32403 14-35) Bellingham, Wash., Society of Photo-Optical Instrumentation Engineers, 1980, p. 156-161., 1980.*
- [24] H.I. Bjelkhagen. Holographic Portraits Made by Pulse Lasers. *Leonardo*, 25

- (5):443–448, 1992.
- [25] D.J. De Bitetto. Holographic image system and method employing narrow strip holograms, 1970. US Patent 3,547,510.
- [26] D. J. De Bitetto. Bandwidth Reduction of Hologram Transmission Systems by Elimination of Vertical Parallax. *Applied Physics Letters*, 12:176–178, March 1968.
- [27] Bell Telephone Labor Inc. Synthetic hologram generation from a plurality of two-dimensional views, August 1974. US Patent 3,832,027.
- [28] Stephen P. McGrew. System for synthesizing strip-multiplexed holograms, June 1980. US Patent 4,206,965.
- [29] Mikhail V. Grichine, David B. Ratcliffe, and Gleb R. Skokov. Integrated pulsed holography system for mastering and transferring onto agfa or vr-p emulsions. volume 3358, pages 203–210. SPIE, 1998.
- [30] H. Chen and F.T.S. Yu. One-step rainbow hologram. *Opt. Lett*, 2(4):85, 1978.
- [31] Yasushi Ohe, Hiromitsu Ito, and Niro Watanabe. Photosensitive recording material, photosensitive recording medium, and process for producing hologram using this photosensitive recording medium, June 1998. European Patent EP0697631.
- [32] Marvin C. King, A.M. Noll, and D.H. Berry. A new approach to computer-generated holography. *Appl. Opt.*, 9(2):471, 1970.
- [33] Manfred Kock. Method of holographically forming a three-dimensional image from a sequence of two-dimensional images of different perspective., October 1974. US Patent 3,843,225.
- [34] M.T. Gale and J. Kane. Generation of permanent phase holograms and relief patterns in durable media by chemical etching, March 16 1976. US Patent 3,944,420.
- [35] S.P. McGrew. Full-color hologram, December 20 1983. US Patent 4,421,380.
- [36] D. Pizzanelli. The development of direct-write digital holography. *Digital Holography*.

- [37] Frank Davis. System for making a hologram of an image by manipulating object beam characteristics to reflect image data, October 1998. US Patent 5,822,092.
- [38] Craig Newswanger. Holographic diffraction grating patterns and methods for creating the same, March 1994. US Patent 5,291,317.
- [39] Walter C. Spierings and Eric Van Nuland. Development of an office holographic printer ii. volume 1667, pages 52–62. SPIE, 1992.
- [40] Eric Van Nuland and Walter C. Spierings. Development of an office holographic printer iii. volume 1914, pages 9–14. SPIE, 1993.
- [41] Masahiro Yamaguchi, Hideaki Endoh, Toshio Honda, and Nagaaki Ohyama. High-quality recording of a full-parallax holographic stereogram with a digital diffuser. *Opt. Lett.*, 19(2):135, 1994.
- [42] Masahiro Yamaguchi, Takahiro Koyama, Hideaki Endoh, Nagaaki Ohyama, Susumu Takahashi, and Fujio Iwata. Development of a prototype full-parallax holographic printer. volume 2406, pages 50–56. SPIE, 1995.
- [43] M. Kodera. Holography in Japan. *Leonardo*, 25(5):451–455, 1992.
- [44] K. Ohnuma, T. Nishihara, and F. Iwata. Full color rainbow hologram using a photoresist plate. *Proc. SPIE*, 1051, 1989.
- [45] Robert J. Perlmutter. Optical-digital hologram recording, October 1987. US Patent 4,701,006.
- [46] Tomohisa Hamano and Hiroshi Yoshikawa. Image-type cgh by means of e-beam printing. volume 3293, pages 2–14. SPIE, 1998.
- [47] David Brotherton Ratcliffe, Florian Michel Robert Vergnes, Alexey Rodin, and Mikhail Grichine. Holographic printer. Patent 7324248, Jan 2008.
- [48] Eugene Hecht. *Optics*, chapter 8. Addison Wesley, 2nd edition, 1990.
- [49] ZEMAX Development Corporation. 3001 112th avenue ne, suite 202, Bellevue, wa 98004-8017 usa.
- [50] Fred A. Carson. *Basic Optics and Optical Instruments*, chapter 4. Courier Dover Publications, 1969.

- [51] BM Oliver. Sparkling spots and random diffraction. *Proceedings of the IEEE*, 51(1):220–221, 1963.
- [52] JW Goodman. Some fundamental properties of speckle. *J. Opt. Soc. Am*, 66(11):1145–1150, 1976.
- [53] T. Iwai and T. Asakura. Speckle reduction in coherent information processing. *Proceedings of the IEEE*, 84(5):765–781, 1996.
- [54] FTS Yu and EY Wang. Speckle reduction in holography by means of random spatial sampling. *Applied Optics*, 12(7):1656, 1973.
- [55] M. Kato and Y. Okino. Speckle reduction by double recorded holograms. *Appl. Opt*, 12:1199–1201, 1973.
- [56] M. KATO, Y. NAKAYAMA, and T. SUZUKI. Speckle reduction in holography with a spatially incoherent source. *Applied Optics*, 14:1093–1099, 1975.
- [57] GE Trahey, JW Allison, SW Smith, and OT Van Ramm. A quantitative approach to speckle reduction via frequency compounding. *Ultrasonic imaging(Print)*, 8(3):151–164, 1986.
- [58] Seung-Ho Shin and Bahram Javidi. Speckle-reduced three-dimensional volume holographic display by use of integral imaging. *Appl. Opt.*, 41(14):2644–2649, 2002.
- [59] H. Ambar, Y. Aoki, N. Takai, and T. Asakura. Mechanism of speckle reduction in laser-microscope images using a rotating optical fiber. *Applied Physics B: Lasers and Optics*, 38(1):71–78, 1985.
- [60] H. AMBAR, Y. AOKI, N. TAKAI, and T. ASAKURA. Relationship of speckle size to the effectiveness of speckle reduction in laser microscope images using rotating optical fiber. *Optik(Stuttgart)*, 74(1):22–26, 1986.
- [61] H. Ambar, Y. Aoki, N. Takai, and T. Asakura. Fringe contrast improvement in speckle photography by means of speckle reduction using vibrating optical fiber. *Optik(Stuttgart)*, 74(2):60–64, 1986.
- [62] L. Wang, T. Tschudi, T. Halldorsson, and P.R. Petursson. Speckle reduction in laser projection systems by diffractive optical elements. *Applied Optics*, 37

- (10):1770–1775, 1998.
- [63] P.F. Michaloski and B.D. Stone. Laser illumination with speckle reduction, February 20 2001. US Patent 6,191,887.
- [64] Stanislovas J. Zacharovas, Alexey M. Rodin, David B. Ratcliffe, and Florian R. Vergnes. Holographic materials available from geola. *Practical Holography XV and Conference 4296B: Holographic Materials VII (Proceedings of SPIE Volume 4296)*, 4296:206–212, June 2001.
- [65] Slavich. Joint stock co., micron branch co., 2 pl. mendeleeva, 152140 pereslavl-zalessky, russia.
- [66] Vladimir B. Markov. Some characteristics of a single-layer color hologram.
- [67] Vladimir B. Markov and Anatoliy I. Khizhnyak. Selective characteristics of single-layer color holograms.
- [68] Hans I. Bjelkhagen, Qiang Huang, and Tung H. Jeong. Progress in color reflection holography.
- [69] M. Liebling. *On Fresnelets, Interference fringes, and digital holography*. PhD thesis, ÉCOLE POLYTECHNIQUE FÉDÉRALE DE LAUSANNE, 2004.
- [70] P. Sandoz. Wavelet transform as a processing tool in white-light interferometry. *Optics Letters*, 22(14):1065–1067, 1997.
- [71] R.J. Recknagel and G. Notni. Analysis of white light interferograms using wavelet methods. *Optics Communications*, 148(1-3):122–128, 1998.
- [72] S. Sotthivirat and J.A. Fessler. Penalized-likelihood image reconstruction for digital holography. *Journal of the Optical Society of America A*, 21(5):737–750, 2004.
- [73] JP Allebach, B. Liu, and NC Gallagher. Aliasing error in digital holography. *Applied Optics*, 15(9):2183–2188, 1976.
- [74] A.K. Evans. Resolution limits and noise reduction in digital holographic microscopy. *Proceedings of SPIE*, 4659:35, 2003.
- [75] M. Jacquot, P. Sandoz, and G. Tribillon. High resolution digital holography. *Optics Communications*, 190(1-6):87–94, 2001.

- [76] N. D. Vorzobova. Pulsed holographic recording under various external lighting conditions. *J. Opt. Technol.*, 71(10):682–684, 2004.
- [77] Geola Technologies Ltd. Geola uab., 2006 vilnius, lithuania.
- [78] Stanislovas J. Zacharovas, David B. Ratcliffe, Gleb R. Skokov, Sergey P. Vorobyov, Petr I. Kumonko, and Yury A. Sazonov. Recent advances in holographic materials from slavich. volume 4149, pages 73–80. SPIE, 2000.
- [79] Yuk Wah Joseph Koo. Single mode pulsed laser., May 1984. European Patent EP0109254.
- [80] András Bálint. *Instrument Engineers Handbook Process Control and Optimization*. 2005.
- [81] A. Rodin, F.M.R. Vergnes, and D. Brotherton-Ratcliffe. Direct write holographic printer, April 3 2007. US Patent 7,199,814.
- [82] H.I. Bjelkhagen and E. Mirlis. Color holography to produce highly realistic three-dimensional images. *Applied Optics*, 47(4):123–133, 2008.
- [83] L. Hryniw, A. Rodin, and D. Brotherton-Ratcliffe. Method of writing a composite 1-step hologram, February 19 2008. US Patent 7,333,252.
- [84] T.N. Chang. Piezoelectric multiple degree of freedom actuator, March 19 2002. US Patent 6,359,370.

A

Program listing for image cropping

This is an example perl program to take a folder of files with the image type 'png' and crops each image with a sliding window. The code assumes that there are 492 images named 0001.png, 0002.png, etc, each of size 2460×960 pixels that need to be cropped to the size 1230×960. It utilizes the ImageMagick 'convert' program.

```
1 #!/usr/bin/perl
2 for($f=0;$f <= 492; $f++) {
3     system "echo $f";
4     $command= "echo convert -crop 1230x960+" . (($f-1)*5) . \
5         "x0 frame" . sprintf("%04d", $f) . ".png cropped_" . \
6         sprintf("%04d", $f) . ".png";
7     print $command;
8 }
```

Figure A.1: Program listing for cropping a series of images with a sliding window

B

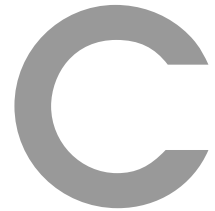
DTC commands

The communication protocol between the Digital Temperature Controller boards underwent many revisions. The final revision of the command set is given in Table B.1 on the next page. Missing identification numbers are due to deprecated commands due to the revision process. For completeness, the commands for the shutter system have been left in. The DTC boards were extended in their use to also control shutters in the beam to block the beam as needed.

'D1' indicates an 1 byte number. 'D1 D2' indicates a 16 byte number with most significance bit first.

ID	Returns	Command	Arguments	Description
1	D1 D2	get_temp1		Get current temperature
2	D1 D2	get_temp2		Get internal temperature value
6	D1 D2	get_status	1 – DTC, 2 – Shutter	Get status of the specified component.
8		set_tset	D1 D2	Set target temperature to heat to
9	D1 D2	get_tset		Get target temperature to heat to
10		set_kp	D1	Set Kp – the proportional coefficient in PID algorithm
11		set_ki	D1	Set Ki – the integrating coefficient in PID algorithm
12		set_kd	D1	Set Kd – the differential coefficient in PID algorithm
13		set_eilimit	D1	Set maximum number of points to integrate in PID algorithm
16		set_status		Reset the error status
17		set_alltoeeprom		Save all the parameters to non-volatile EEPROM
18		get_allfromeeprom		Load all the parameters to non-volatile EEPROM
20		set_address	D1	Set the node address ID. There must only be one node connected
21		set_shutters	0 – Close, 1 – Open	Open/Close shutter, if attached
22	D1	get_shutters		Get open/close status from shutter, if attached
28	D1	get_version		Get protocol version – to allow for future extensions

Table B.1: Communication protocol for Digital Temperature Controller



Hologram printer diagrams

Figure C.2 on page 155 illustrates the final design of the hologram printer. For comparison, the hologram printer as detailed by Ratcliffe et al. [47] is illustrated in Figure C.1 on the next page. The main difference is that the display system has been changed from a transmissive LCD to a reflective LCOS and moved away from the objective. An afocal relay lens system transports the LCOS image into the position that the LCD original was.

The final objective lens piece is now mounted on a heavy metal board, rather than held by mount.

The final reference beam mirror is now mounted to the optical table via an 'A' shaped support. This isolates it from the vibrations from the translation stages.

The hologram plate holder has been modified to allow for fine adjustment, and the power supply and cooling unit upgraded.

The components labelled in the figures are detailed in the Nomenclature section on page xix.

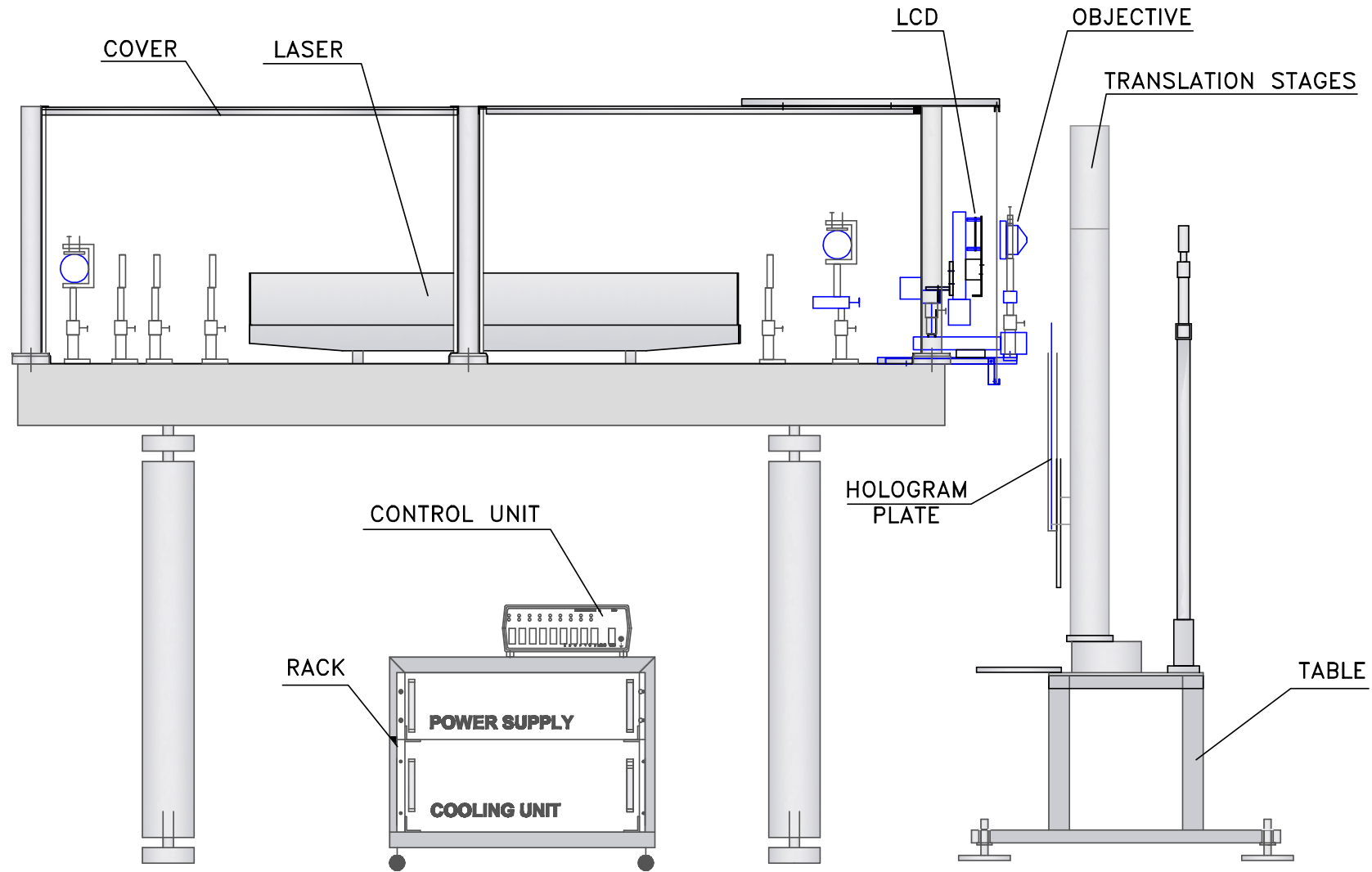


Figure C.1: Side-on orthographic projection of original hologram printer with LCD display system as detailed by Ratcliffe et al. [47]

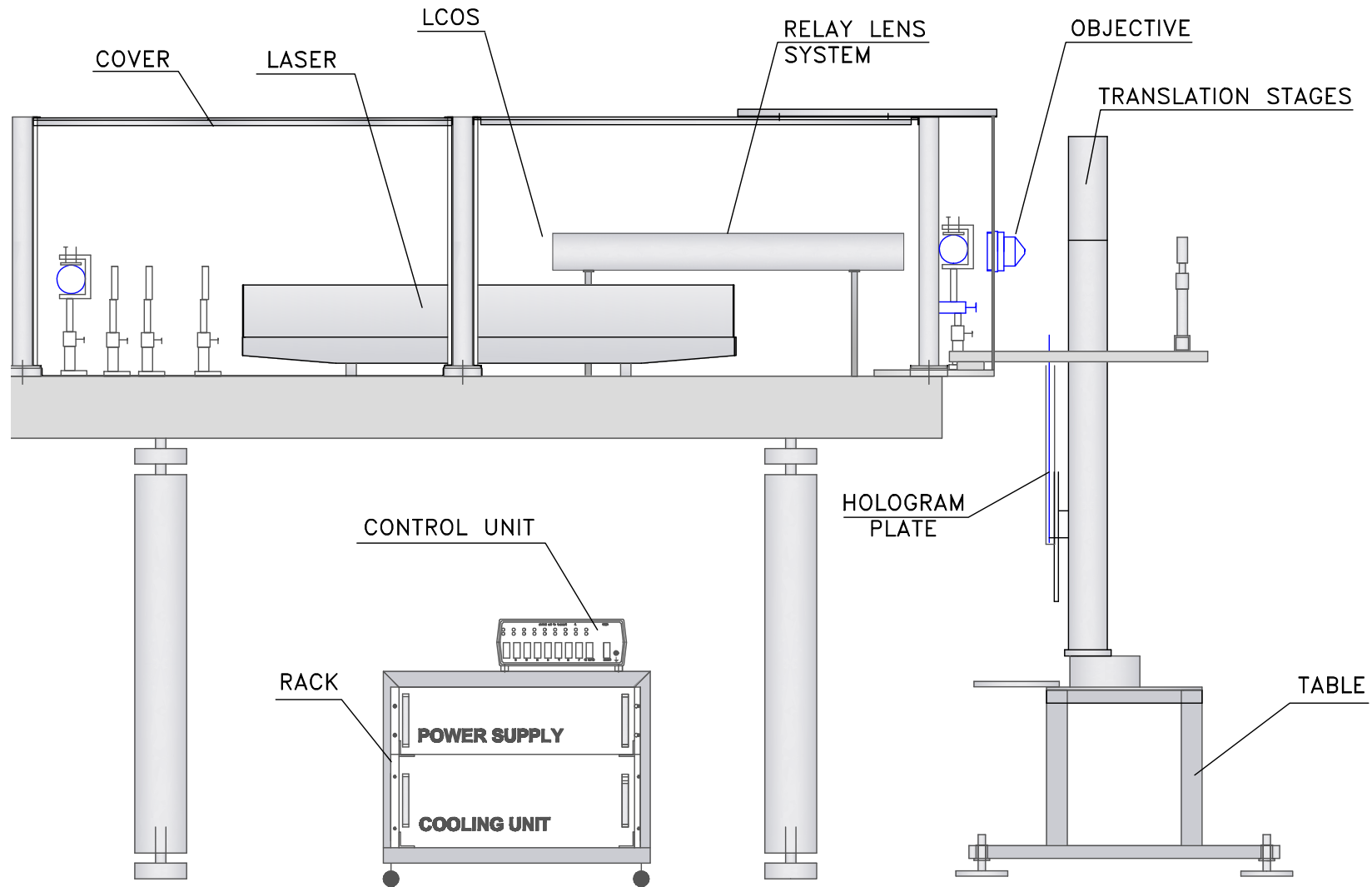


Figure C.2: Side-on orthographic projection of Hologram printer with LCOS display system

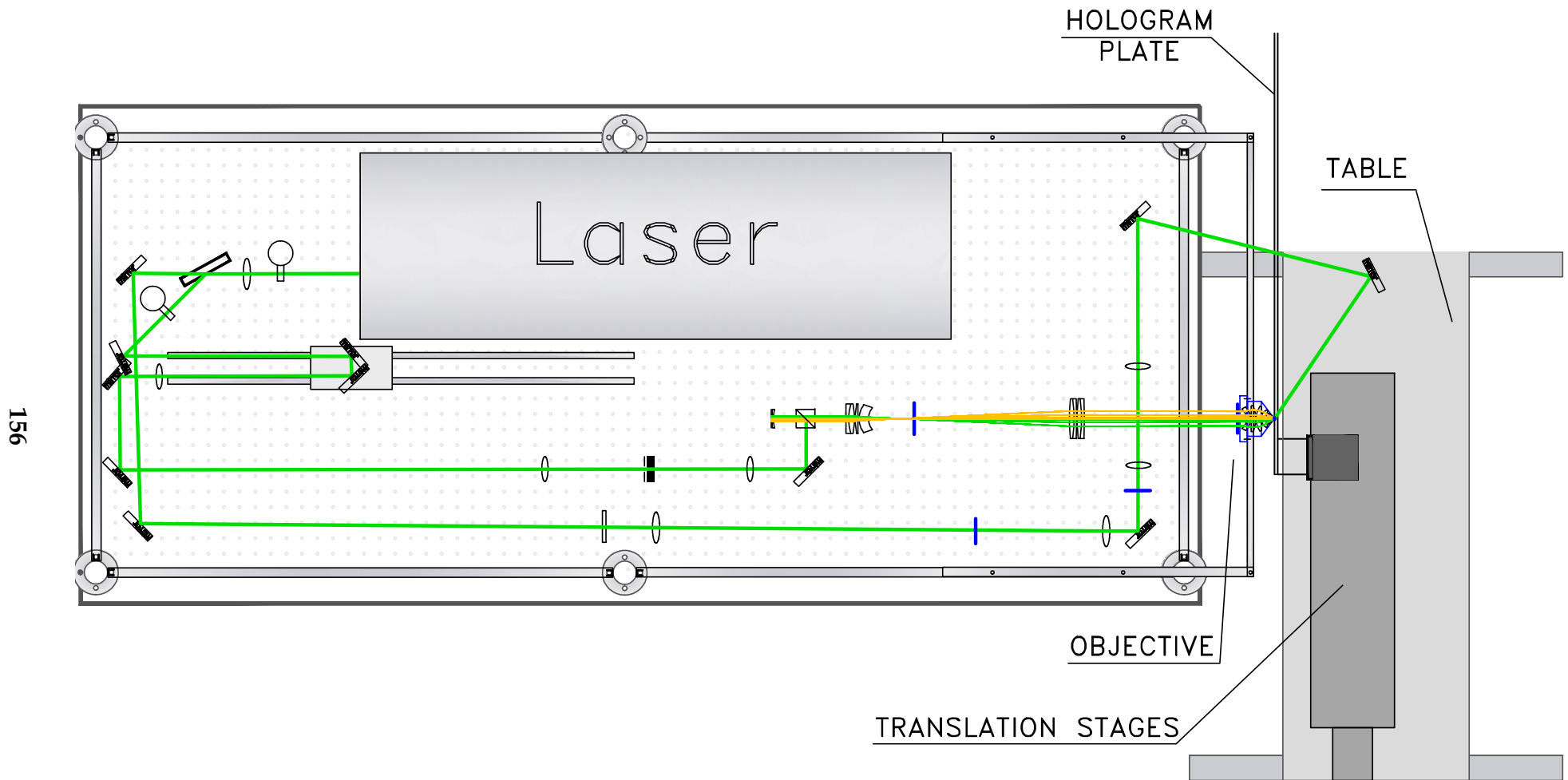


Figure C.3: Top-down orthographic projection of Hologram Printer

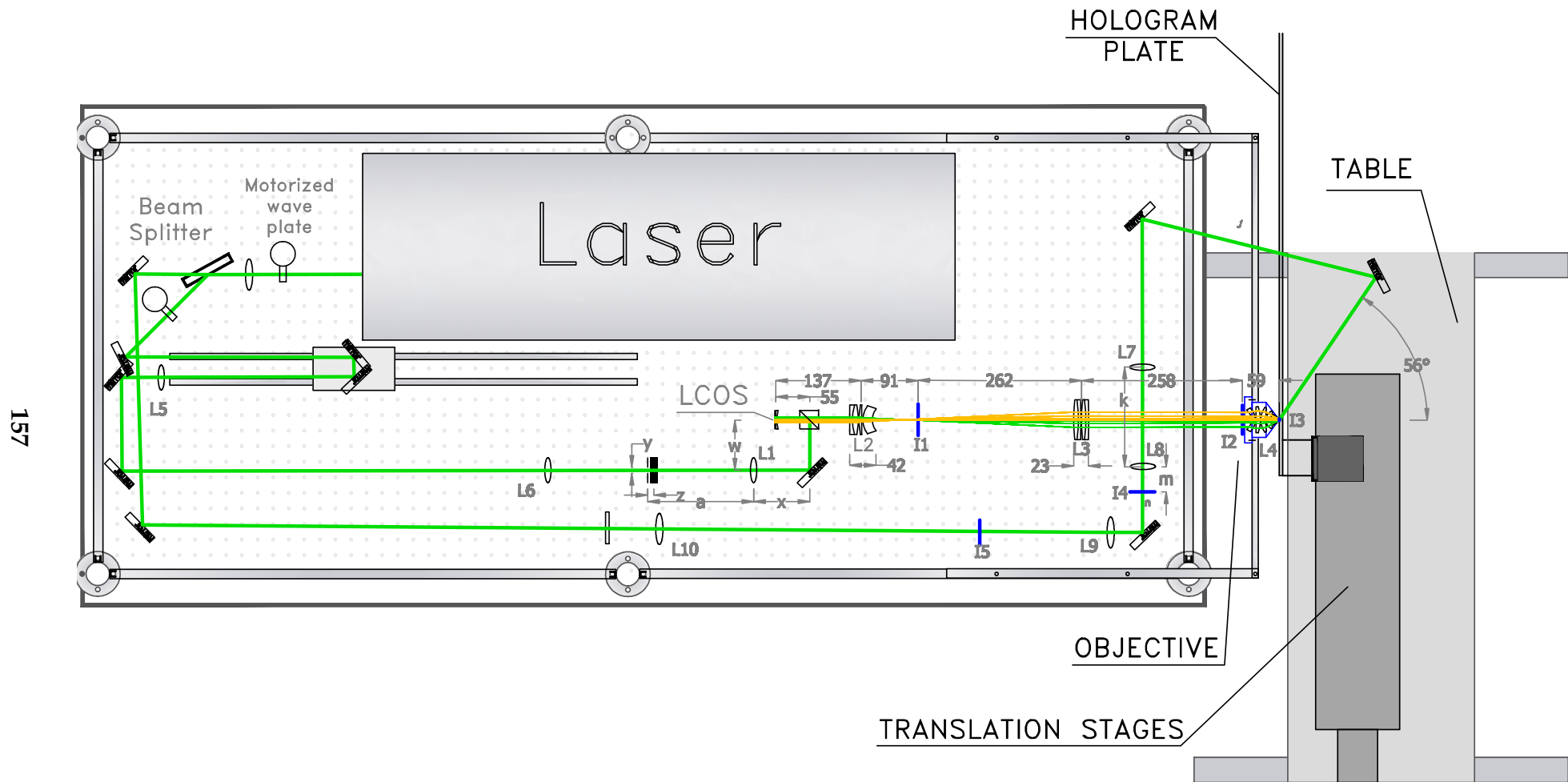


Figure C.4: Top-down orthographic projection of Hologram Printer with dimensions labelled

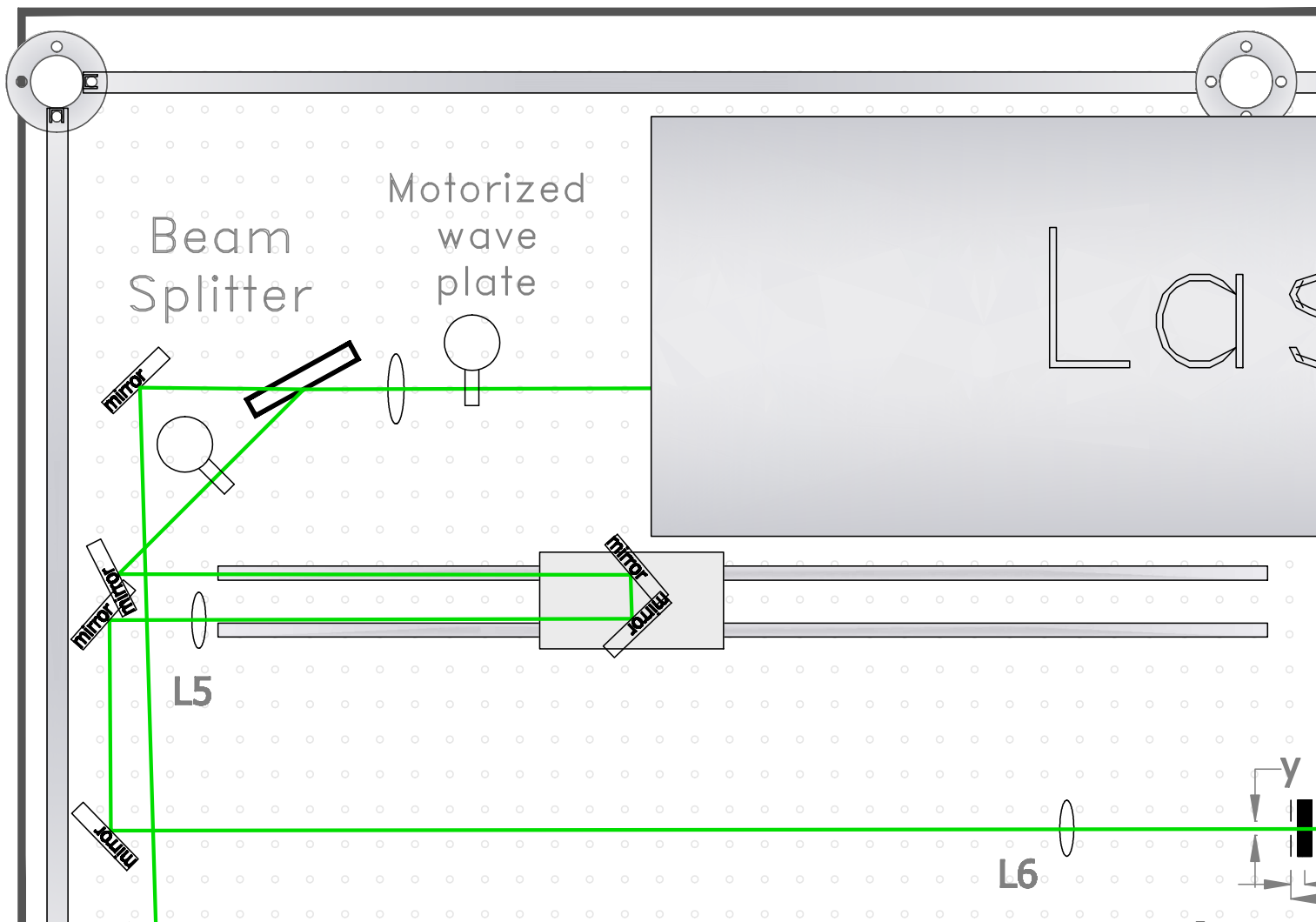


Figure C.5: Top-down orthographic projection of system to adjust optical-path distance of object beam

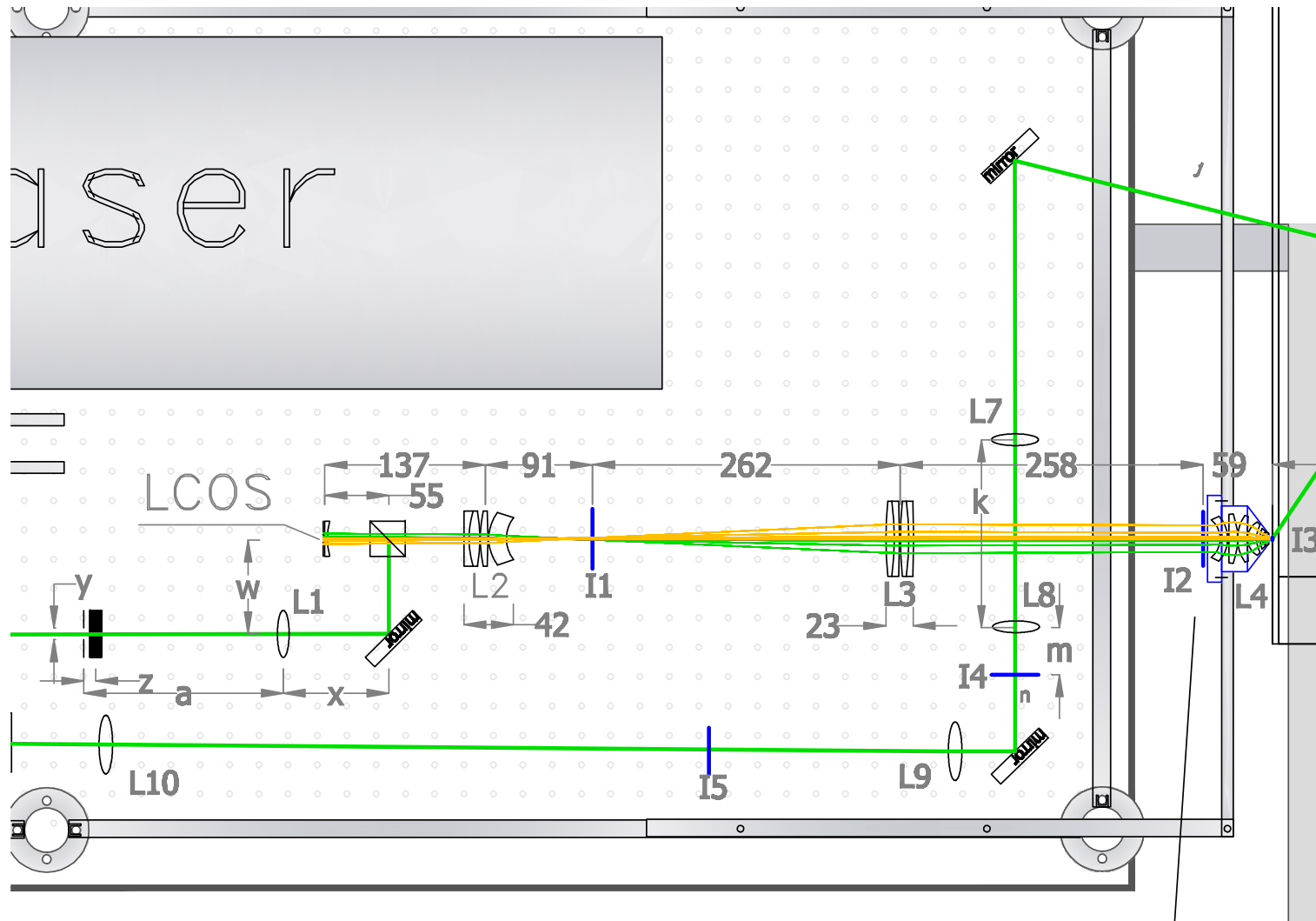


Figure C.6: Top-down orthographic projection of object lens system in hologram printer



Program listing for image analysis

Chapter 4 analysed the White Logo hologram with various techniques. Program listing D.1 gives a matlab program for the simple analysis of a set of images. A Guassian-blur filter is optionally applied to each image.

```

1  % Copyright (C) John Tapsell 2007
2  % Whether to apply a Gaussian-blur
3  % filter to the rendered images:
4  blur_input_images=true;
5
6  % Analysing all the rendered images can take a few minutes.
7  % Setting this reuses the values obtained by the last run.
8  reuse=false;
9
10 % Read in the photograph, and convert it to grayscale.
11 photo = rgb2gray(imread('photo.png'));
12
13 % Read in the closest rendered image to the photograph.
14 % The photograph was taken at close to the normal angle.
15 closest_match = rgb2gray(imread('white_0360.png'));
16
17 % Apply a gaussian blur filter to the photograph.
18 h = fspecial('gaussian',5,1);
19 blur = imfilter(photo,h);
20
21 if ~reuse
22     total_intensity = 0;
23     for i=0:663 % Read image white_0000.png to white_0663.png
24         image_filename = ['white_',num2str(i,'%04d'),' .png'];
25         new_image = rgb2gray(imread(image_filename));
26         if blur_input_images
27             new_image = imfilter(new_image,h);
28         end
29         total_intensity=total_intensity+im2double(new_image);
30     end
31 end
32 plot(blur(:), total_intensity(:),'.', 'MarkerSize', 5);

```

Figure D.1: Program listing for comparing the photograph of the White Logo hologram and the rendered images that were used to construct the said hologram



Optical fourier transform lens system

The telecentric afocal reversing lens system for the objective beam of a direct write digital hologram printer is given below in Figures E.2, E.3 and E.4. The lens system shown is suitable for monochromatic light of wavelength 532 nm (visible green), entering from the polarizing beam splitter cube. The rays reflected from the beam splitter cube are not indicated on the diagrams.

The two focal planes, I1 and I2, are also indicated¹ on the diagrams.

Figure E.5 shows the lens system in in the direct-write hologram printer.

¹Drawn in blue, if in color

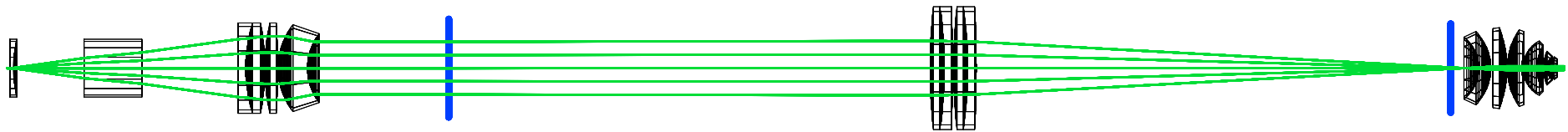


Figure E.1: Lens system for imaging the Fourier transform of the LCOS (shown on the left) onto the the photosensitive emulsion, producing a holopixel (shown on the right). Figures E.2, E.3 and E.4 below provide an enlarged view. The indicated rays trace out a single point on the LCOS display.

163

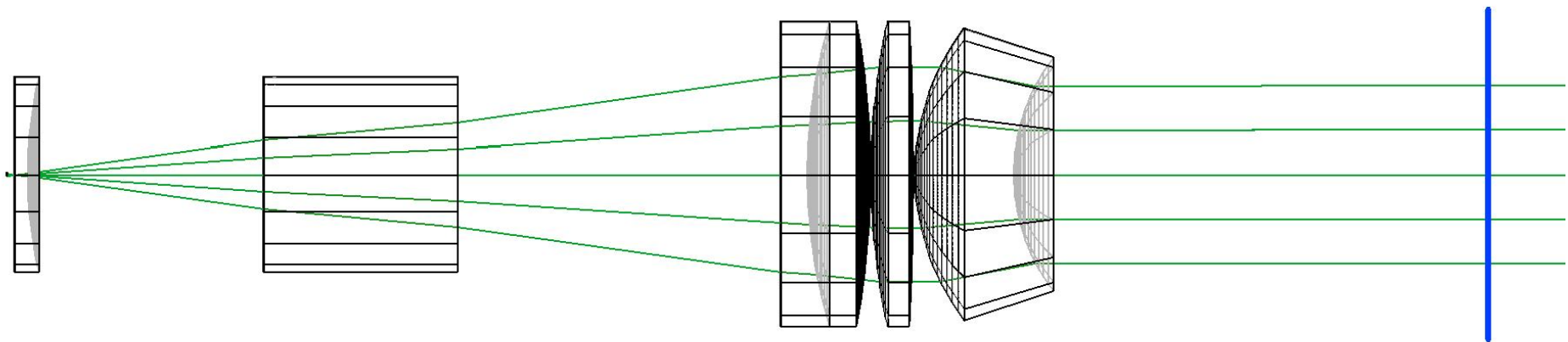


Figure E.2: Compound Lens L2 - First component of telecentric afocal reversing lens system. Images the Fourier transform of the LCOS plane onto the real image I2.

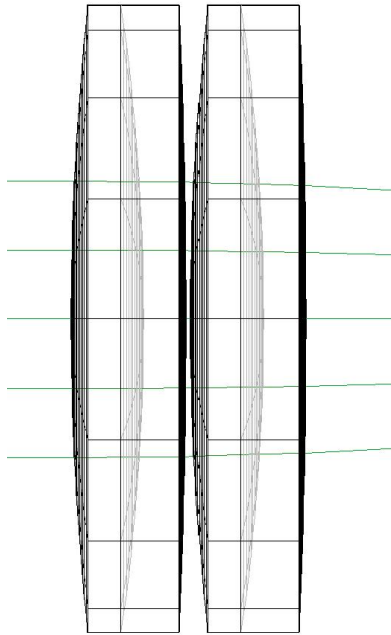


Figure E.3: Compound Lens L3 – Second component of telecentric lens system

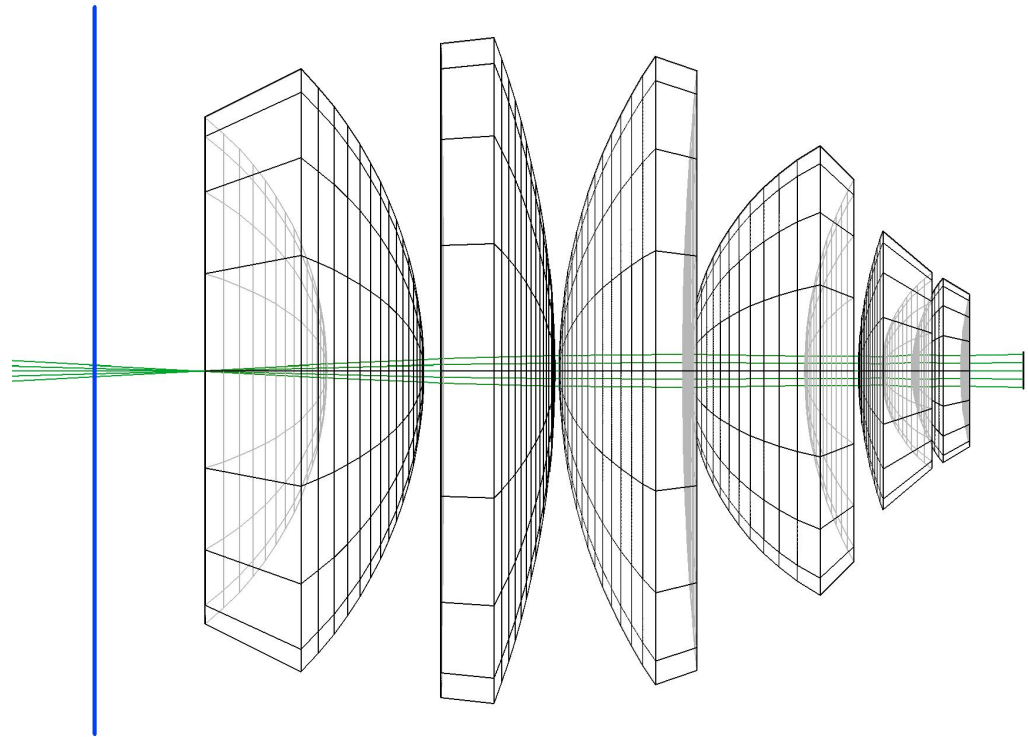


Figure E.4: Compound Lens L4 – Fourier transforms the real image plane (I2) on the left to the holopixel plane on the right (I3)

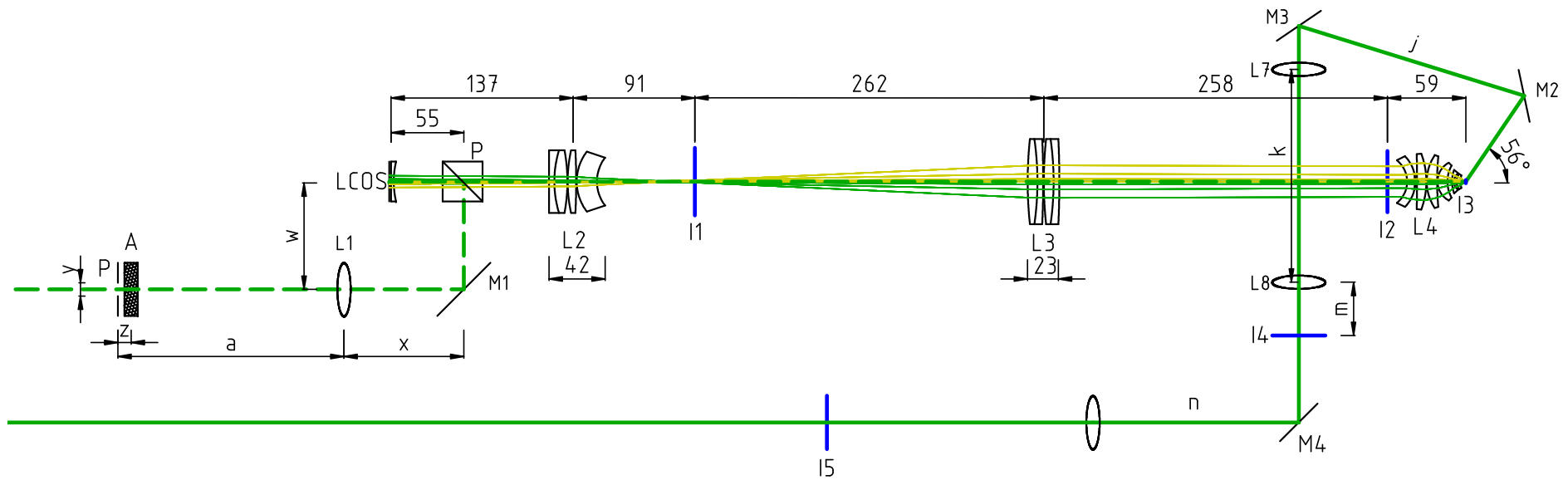


Figure E.5: Top down view of design suitable for direct-write holography of reflection holograms. Sample light rays are shown for the telescopic system. These originate parallel and spatially distinct points on the LCOS display and focus to single point with distinct angles at the final hologram plane I3. Rays below the axial ray are indicated in yellow and rays above the axial ray are indicated in green, for visual confirmation that the afocal lens system is indeed reversing.



LCOS mechanical mount

Figure F.1 on the following page shows that the LCOS was mounted in place with a weak corrective lens in front. This corrective lens ensures that the final projected image has a flat focal plane. The cube split-beam polariser is mounted in the same holder as shown. The laser light enters into the page as a plane wave into the polariser cube. Dimension shown is in millimeters.

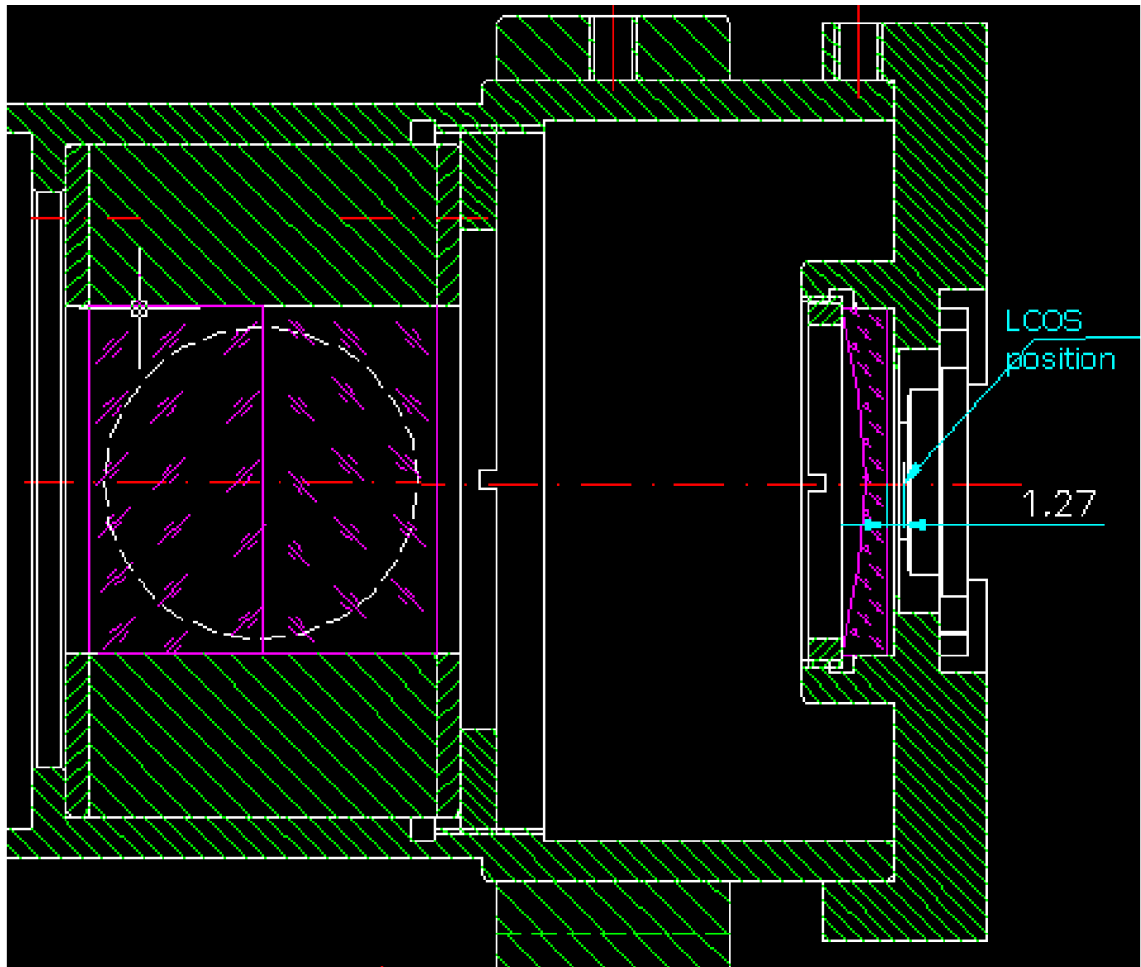


Figure F.1: Side-on orthogonal view of mechanical mount for LCOS and split beam polariser



Lens system

The parameters of the lens components in the LCOS-based hologram printer's relay lens system are given in Table G.1 on the next page. Each surface is given with the material and separation distance to the next surface. All distances are given in millimeters. Note that surfaces 14 and 21 indicate the focal image planes I2 and I1 respectively.

Optical Component Values - Green Channel

Effective Focal Length = -7.669 mm

Total distance from LCOS to image plane I3 = 807.707 mm

No.	Radius	Clear Diameter	Separation	Material	Lens
1	PLANE	2.301	4.00000	Air	
2	-20.34000	9.562	3.07000	S-SF6	L4
3	-9.61600	11.630	1.93000	Air	L4
4	-7.60000	12.360	1.45000	S-SF6	L4
5	-26.03000	17.598	3.45000	Air	L4
6	-25.02700	24.134	7.45000	S-SF6	L4
7	-16.14400	28.390	0.30000	Air	L4
8	-201.01914	37.924	7.80000	S-SF6	L4
9	-35.57000	39.759	0.30000	Air	L4
10	59.70000	42.100	7.03000	S-SF6	L4
11	1310.14201	41.384	1.27000	Air	L4
12	27.27000	38.142	6.15000	S-SF6	L4
13	20.51000	32.078	14.72777	Air	
14	PLANE	46.000	246.59396	Air	
15	693.00000	64.000	4.33000	S-SF5	L3
16	224.90000	64.000	7.33000	S-BK7	L3
17	-304.80000	64.000	0.50000	Air	L3
18	693.00000	64.000	4.33000	S-SF5	L3
19	224.90000	64.000	7.33000	S-BK7	L3
20	-304.80000	64.000	250.10000	Air	
21	PLANE	50.895	73.58000	Air	
22	-29.51000	35.980	15.20000	J-BAF7	L2
23	-37.10000	45.500	0.40000	Air	L2
24	483.10001	47.000	6.40000	J-SK4	L2
25	-110.15000	47.000	0.20000	Air	L2
26	129.42000	47.000	9.80000	J-SK12	L2
27	-80.91000	47.000	4.00000	J-SF14	L2
28	PLANE	47.000	50.00000	Air	
29	PLANE	30.000	30.00000	S-BK7	Beam cube
30	PLANE	30.000	36.68504	Air	
31	-65.84500	30.000	2.00000	S-SF5	LCOS lens
32	PLANE	30.000	1.15834	Air	LCOS

Table G.1: Optical components in afocal reversing telescopic lens system used in LCOS based hologram printer, for green channel. All distances are given in millimeters.



Laser specifications

The laser used for the digital hologram printer is a compact single oscillator flash-lamp pumped Nd:YAG laser producing emissions in the nanosecond regime. The laser produces TEM₀₀ near-diffraction limited radiation at 532 nm. Single Longitudinal Mode operation is provided with a built-in SLM option. Design features include highly stable passive Q-switched linear oscillator and harmonic generation. Fundamental lasing is at 1064 nm.



Figure H.1: Photograph of laser, powersupply and cooling unit. Dimensions shown in mm.

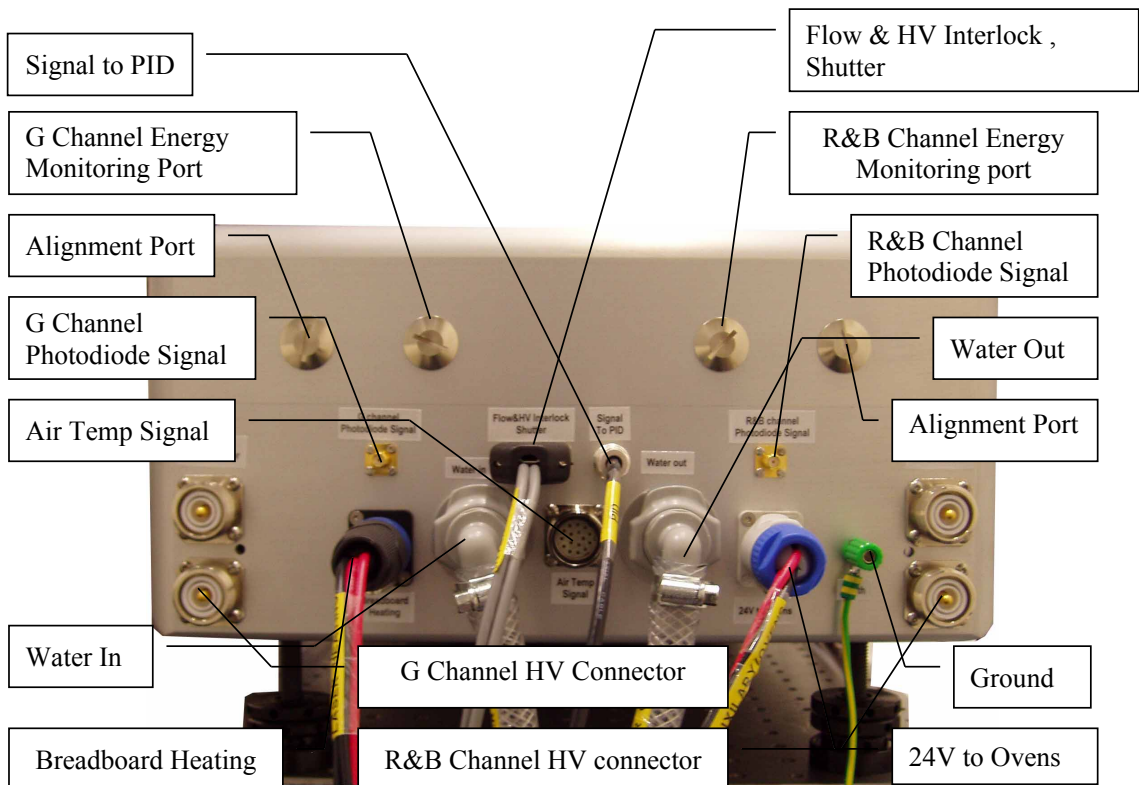


Figure H.2: Labelled photograph of the laser case. Laser shown is the Red-Green-Blue but only the green channel was used for this thesis. The photodiode and heating connection wires for the temperature-feedback system can be seen.

Fundamenta Wavelength	1064 nm
Output Wavelength	532 nm
Output Energy	5 mJ
Shot-to-Shot Energy Stability	3 %
Pulsewidth (FHM)	50 ns
Beam Divergence (1/e ²)	5-7 mm
Beam Divergence	Near diffraction limit
Linewidth	< 0.002 cm ⁻¹
Repetition Rate	50 Hz
Spatial profile	TEM ₀₀
Laser Head Size	860×360×180 mm ³
Resonator Base Plate	Al-alloy
Q-switching	Passive
Flash Tube Lifetime	> 107 shots
Advised Operating Temperature	19 - 21 ° C
Advised Operating Humidity	< 70 % non-condensing
Powering	220 V, 1 phase
Warranty Period	12 months

Table H.1: Specifications of laser used. Energy stability figure given is with temperature-energy feedback system described in Chapter 6 on page 113.



Micro lens array analysis

The following three tables give the raw data from an experiment with three different microlens arrays. In order to reduce speckle on the projected image, the three different microlens arrays were tested at different positions and the results recorded.

The microlens arrays are composed of thousands of small lenses (aka *lenslets*) made from BK7 glass. The lenslets are spherical lenses with a radius of curvature of the order of a millimeter. The lenslets are rectangularly packed with an aspect ratio close or equal to that of the LCOS display system.

In the tables, '*Dist. A*' is the distance of the lens array from the closest lens with an uncertainty of ± 0.1 cm. '*Dist. B*' is the distance of the interference pattern from the aperture with an uncertainty of ± 0.5 cm, discussed in more detail in Section 3.4 on page 51.

The important data to note in the tables is the 'Noise pattern' column. The

image projected from the LCOS has speckle. This image was projected onto a white board 1.2 m away from the final objective lens and the repeating patterns in the speckle measured with a ruler, averaging over several. The overall contrast of the speckle was also noted (lower is better) as well as the overall fidelity of the image. This was judged by eye.

When the lens array focal point is imaged directly onto the LCOS, the energy density on the LCOS is sufficiently high to risk breaking the LCOS. This was avoided and noted in the tables where applicable.

I.1 First microlens array

Each lenslet is rectangular with a size of 0.40 mm×0.46 mm. The lenslets are spherical lenses with a radius of 1.3 mm

Dist.A (cm)	Dist.B (cm)	Size/shape of beam	Average intensity across LCOS	Noise Pattern
1.2	8.0	Too big - too much energy lost	Good in the middle half, faded at edges	Very poor image - strong dominant lines of about 1-2 cm separation
3.5	5.5	Just the right size	Majority is good, but faded steps at top and bottom	On the order of a few pixels. Mediocre quality. 10 big repeating structures = 14.8 cm. Very sensitive to movement.
4.0	4.2	Just the right size	Almost perfect - just slight fading at very top and bottom.	Structure at the pixel level. 10 big repeating structures = 12.5 cm
4.5	4.0	Just the right size	Almost perfect - just slight fading at very top and bottom.	Structure at the pixel level. 10 big repeating structures = 12.4 cm
4.7	2.1	Just the right size	Almost perfect - just slight fading at very top and bottom.	Structure at the pixel level. 10 big repeating structures = 11.1 cm. Best fidelity and low contrast image.
5.0	1.5	Just the right size	Almost perfect - just slight fading at very top and bottom.	Structure at the pixel level. 10 big repeating structures = 11.5 cm
5.2	0.0	Just the right size	Almost perfect - just slight fading at very top and bottom.	Structure at the pixel level. 10 big repeating structures = 10.5 cm

Continued on next page

Raw data for first lens array continued

5.5	-0.8	Just the right size	Almost perfect - just slight fading at very top and bottom.	Structure at the pixel level. 10 big repeating structures = 10.0 cm. Fidelity isn't too bad.
5.7	-1.7	Just the right size	Almost perfect - unevenness is just starting to be noticeable by eye	Structure at the pixel level. 10 big repeating structures = 10.0 cm. Fidelity isn't too bad.
6.0	-4.0	Just the right size	Almost perfect - just slight fading at very top and bottom. Unevenness is a small bit more noticeable at top and bottom.	Structure at the pixel level. 10 big repeating structures = 9.0 cm. Fidelity isn't too bad.
6.5	-6.8	Slightly too small	Visible darkening bars at top and bottom quarters. printing. Possibly even desirable. Software correctable.	Structure at the pixel level. 10 big repeating structures = 7.8 cm. Loosing fidelity. Possibly still okay.
7.0	< -19	Too small	Much more visible darkening bars. Dark lines on top and bottom around the bars. Not suitable for holography.	Structure at the pixel level. 10 big repeating structures = 4.3 cm. Loosing fidelity. Possibly still okay.
7.5	< -19	Too small	Not even at all. Looks like a spherical waffle. Not suitable for holography.	Structure at the pixel level. 30 big repeating structures = 13.5,14.9,15.2,15.1 cm. Terrible fidelity.
8.0	< -19	Too small	Not even at all. Looks like a spherical waffle. Not suitable for holography.	Structure at the pixel level. 10 big repeating structures = 3.0 cm. Terrible fidelity.

Continued on next page

Raw data for first lens array continued

From 7.5 cm it became more and more difficult to measure the repeating pattern. The pattern no longer repeated so obvious and was too hard to count. At 8.5 cm the image fidelity is awful. Somewhere around 9.0 cm each lenslet focuses to a point on the LCOS. This was not measured too accurately for fear of damaging the LCOS. As the pixel becomes noticeably larger now and has a square shape, despite no aperture at all.

9.5	Before LCOS	Too small	Beautifully smooth spherical Gaussian shape	Bright points were just off of focus point of each lenslet
10.0	Before LCOS	Too small	Beautifully smooth spherical Gaussian shape	Beautifully smooth illumination but only illuminating a small middle section

Past 9.7 cm the beam becomes too large for the first lens in the lens relay telescope. This causes the energy to drop off quickly and gives a dim useless image.

Table I.1: Raw data results for first lens array. Each lenslet is rectangular with a size of 0.40 mm×0.46 mm. The lenslets are spherical lenses with a radius of 1.3 mm

I.2 Second microlens array

Each lenslet is rectangular with a size of $0.20\text{ mm} \times 0.23\text{ mm}$. The lenslets are spherical lenses with a radius of 0.65 mm . Note that the pattern from the lens array on the projected image was much much smaller and harder to see.

Dist.A (cm)	Dist.B (cm)	Size/shape of beam	Average intensity across LCOS	Noise Pattern
2.2	10.5	Just the right size	Beautifully smooth. No complaints	7 big repeating structures = 25.5 cm. Worst fidelity yet. Horrible
3.0	8.0	Just the right size	Beautifully smooth. No complaints	4 big repeating structures = 11.5 cm but hard to measure. Bad fidelity but getting better certainly
3.5	8.0	Just the right size	Beautifully smooth. No complaints	4 big repeating structures = 10.0 cm but hard to measure. fidelity is getting a bit better but still worse then previous lensarray
4.0	7.4	Just the right size	Beautifully smooth. No complaints	5 big repeating structures = 10.0 cm but hard to measure. fidelity is getting better slowly
4.5	6.4	Just the right size	Beautifully smooth. No complaints	10 big repeating structures = 22.0 cm but hard to measure. fidelity is getting better slowly
5.0	5.0	Just the right size	Beautifully smooth. No complaints	10 big repeating structures = 21.0 cm but hard to measure. fidelity is still getting better slowly
5.5	2.0	Just the right size	Beautifully smooth. No complaints	10 big repeating structures = 19.0 cm but hard to measure. fidelity is still getting better slowly
6.0	0.0	Just the right size	Beautifully smooth. No complaints	10 big repeating structures = 17.0 cm but hard to measure. fidelity is looking very nice

continued on next page..

...raw data for second lens array continued				
6.5	-3.5	Just the right size	Beautifully smooth. No complaints	10 big repeating structures = 15.5 cm but hard to measure. fidelity is looking very nice
7.0	-10.0	Just the right size	Beautifully smooth. No complaints	10 big repeating structures = 11.2 cm but hard to measure. fidelity is looking very nice
7.5	< -17	Starting to shrink	Beautifully smooth. No complaints	10 big repeating structures = 9.2 cm but hard to measure. fidelity is getting worse again
8.0	< -17	A bit too small	Beautifully smooth but fading around the edges	30 big repeating structures = 19.0 cm but hard to measure. fidelity is now horrible
8.5	< -17	Smaller	Beautifully smooth, almost Gaussian now	Can't measure repeating structure. Awful fidelity! Strong circular pattern appearing

Now it again becomes close to where each lenslet focuses to a point on the LCOS.
Skipping this bit to protect the screen.

10.1	Before LCOS	Too small.		Bright points where just off of focus point of each lenslet
10.5	Before LCOS	Too small.	Smooth spherical Gaussian shape	Fidelity isn't that good - repeating small structure. only illuminating a small middle section

Table I.2: Raw data results for second lens array. Each lenslet is rectangular with a size of $0.2 \text{ mm} \times 0.23 \text{ mm}$. The lenslets are spherical lenses with a radius of 0.65 mm

I.3 Third microlens array

Each lenslet is rectangular with a size of 0.040 mm×0.046 mm. The lenslets are spherical lenses with a radius of 0.13 mm.

Dist.A (cm)	Dist.B (cm)	Size/shape of beam	Average intensity across LCOS	Noise Pattern
0.0	~12.5	A bit too big	Beautifully smooth	6 difficult to count repeating structures = 21.5 cm. Good fidelity.
2.0	~10.0	Still a bit too big	Beautifully smooth	6 repeating structures = 19.7 cm. Structure is slight stronger, but still good fidelity.
2.5	~9.5	Good	Beautifully smooth	7 repeating structures = 23.6 cm. Good fidelity.
3.0	~8.5	Good size	Beautifully smooth	8 repeating structures = 25.2 cm. Good fidelity.
3.5	~8.0	Good size	Beautifully smooth	5 repeating structures = 11.4 cm. Good fidelity.
4.0	~7.5	Good size	Beautifully smooth	8 repeating structures = 18.7 cm. Good fidelity.
4.5	5.5	Good size	Beautifully smooth	8 repeating structures = 17.9 cm. Good fidelity.
5.0	2.1	Good size	Beautifully smooth	10 repeating structures = 22.0 cm. Good fidelity.
5.5	0.2	A bit too small	Beautifully smooth	8 repeating structures = 15.4 cm. Very nice fidelity.
6.0	-1.8	3/4 Too small	Some gradient appearing	5 repeating structures = 7.8 cm. Very nice fidelity.
6.5	-5.0	3/4 Too small	Some gradient appearing	6 repeating structures = 9.3 cm. Great fidelity.
7.0	-9.8	3/4 Too small	more gradient	10 repeating structures = 12.3 cm. Great fidelity.
7.5	-15.0	3/4 Too small	more gradient	8 repeating structures = 8.7 cm. Great fidelity.
8.0	< -17	1/2 Too small	more gradient	10 repeating structures = 7.1 cm. Great fidelity.
8.5	< -17	1/2 Too small	unacceptable gradient	10 repeating structures = 5.0 cm. Bad fidelity because we start to see curved patterns from lens array.

continued on next page..

...raw data for third lens array continued				
9.0	< -17	1/3 Too small	unacceptable gradient	6 repeating structures = 17.7 cm and sub repeating at 10 repeating structures = 2.9 cm. stronger curved patterns from lens array, but actually acceptable probably
Around 9.5 cm is close to where the lenslet focuses to a point on the LCOS. Skipping this bit to protect the screen.				
10.0	< -17	1/3 Too small	unacceptable gradient	Wonderful fidelity. No repeating structures.
10.5	< -17	1/3 Too small	smooth but covers a small part	Wonderful fidelity. No repeating structures.
11.0	< -17	1/2 Too small	smooth but covers a small part - too big for first lens in lens array	Wonderful fidelity. No repeating structures.
13.5	< -17	Good size	covers only a small part because first lens in lens array is too small	Okay fidelity - repeating structure again.

Table I.3: Raw data results for third lens array. Each lenslet is rectangular with a size of $0.040\text{ mm} \times 0.046\text{ mm}$. The lenslets are spherical lenses with a radius of 0.13 mm .



Hologram printer photographs

A few photographs taken while working on the printer. Note that the photographs do not necessarily reflect the final design. In particular the LCOS display and surrounding compound lenses and beam polariser are shown mounted individually, while the final design placed them inside a single enclosed metal tube.

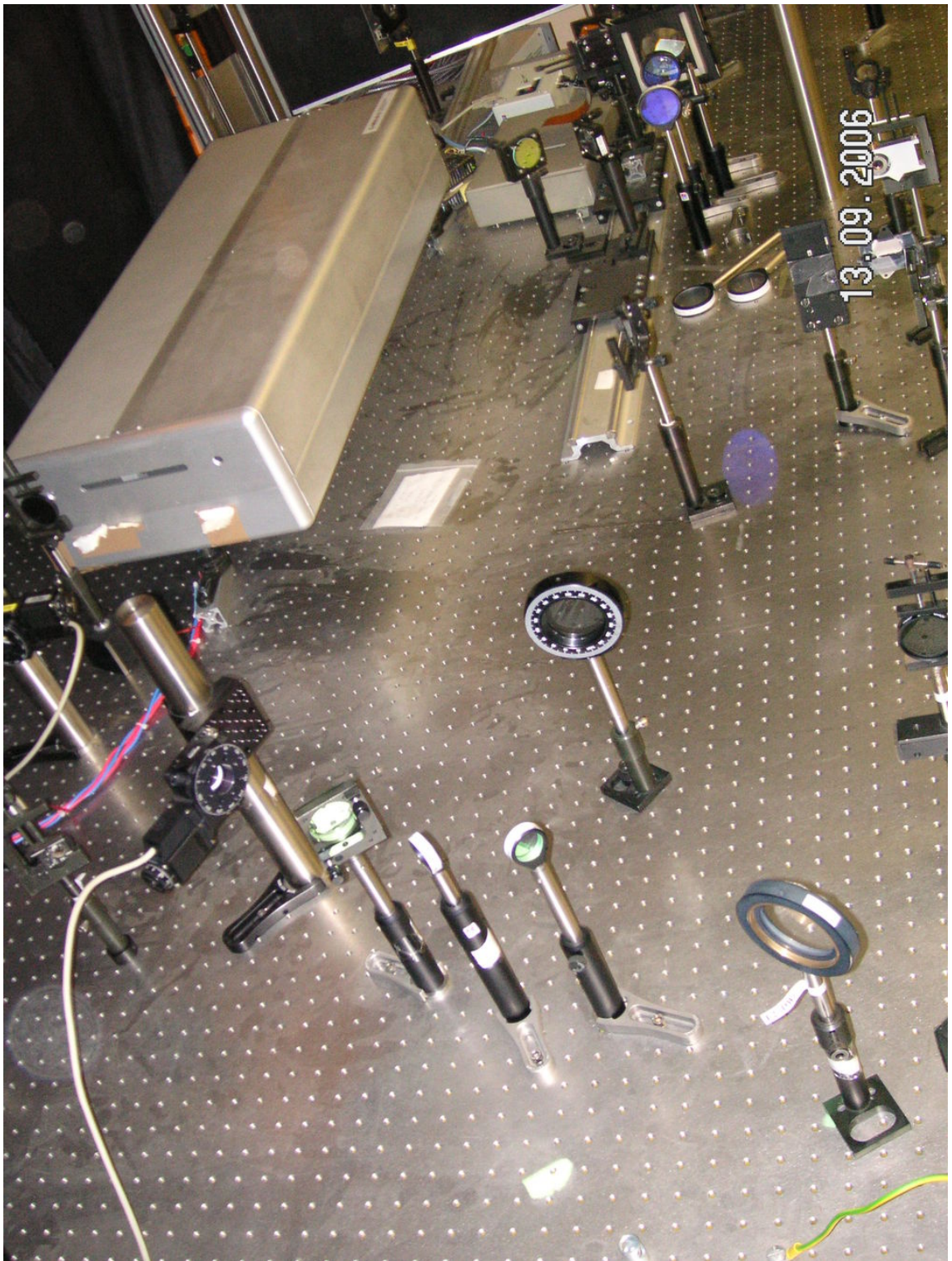


Figure J.1: Photograph of part of the hologram printer

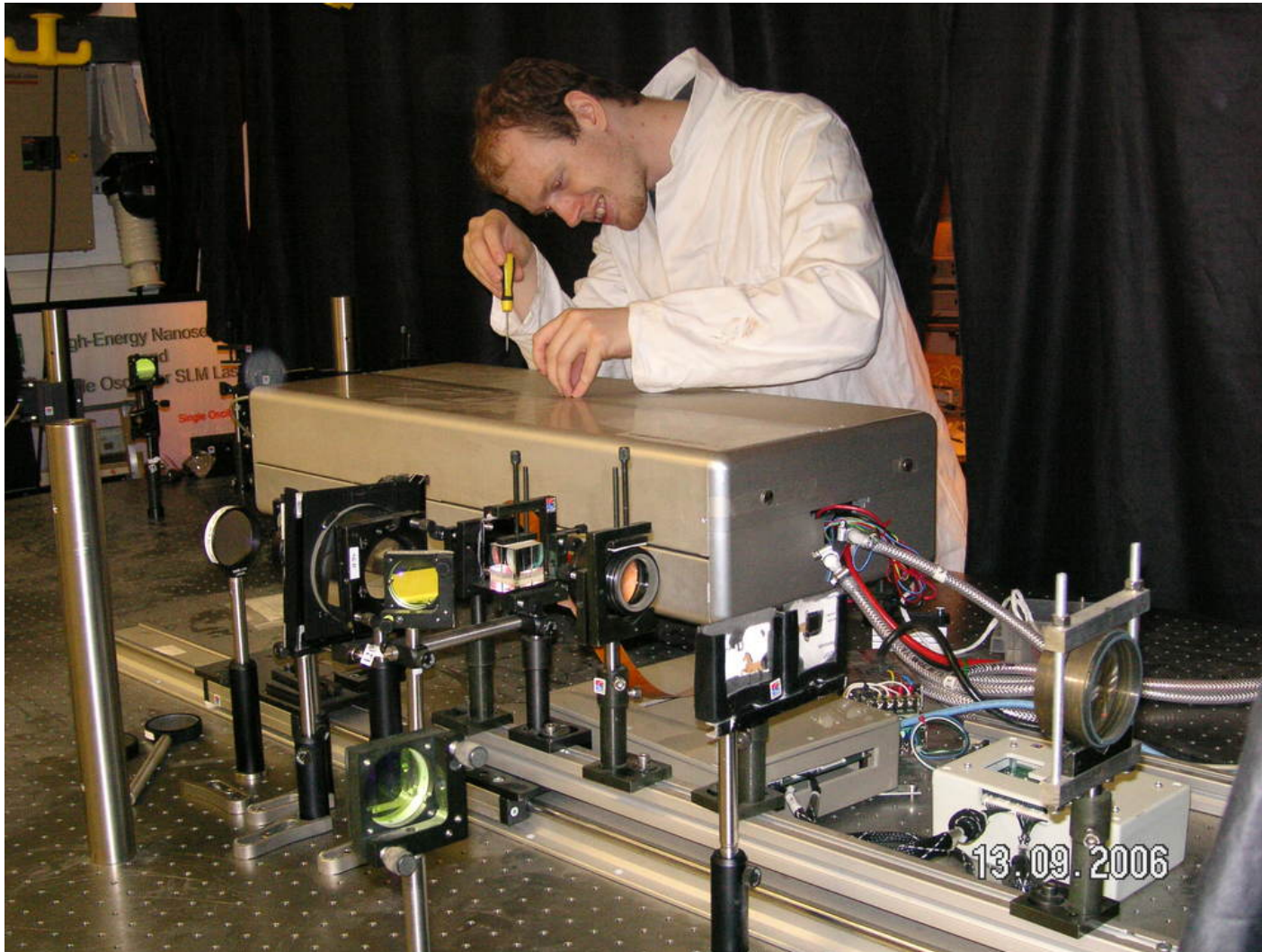


Figure J.2: Photograph of me working on the hologram printer



Figure J.3: Photograph of LCOS section of the hologram printer

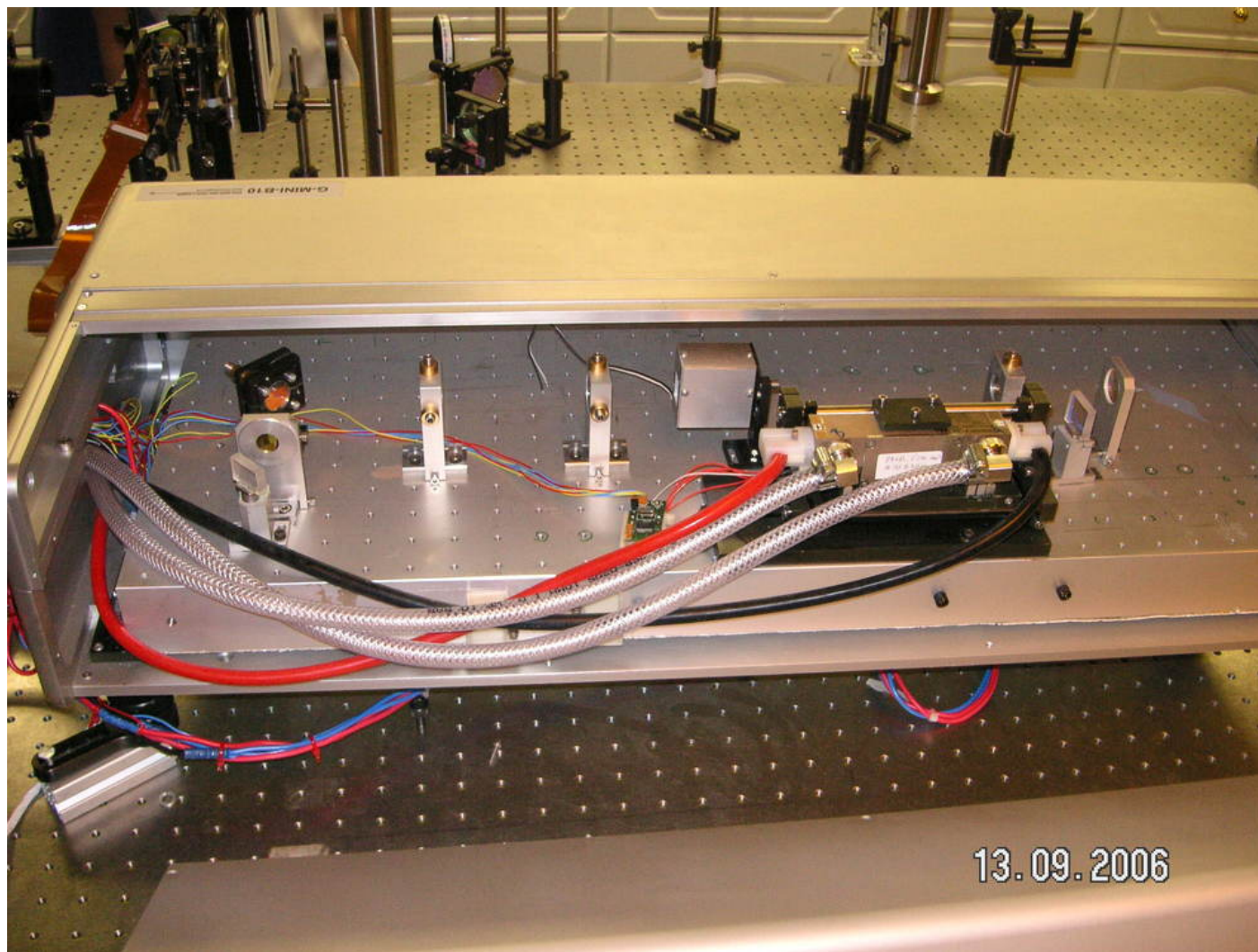


Figure J.4: Photograph of frequency-doubled short cavity Nd:YAG laser